ENHANCING MULTIPLE FUNCTIONALITIES OF SHAPE MEMORY POLYURETHANE FOAMS AND BUILDING AN *IN VITRO* PLATFORM OF ANEURYSM-BEARING VASCULAR STRUCTURE

A Dissertation

by

LINDY KANG JANG

Submitted to the Office of Graduate and Professional Studies of

Texas A&M University

in partial fulfillment of the requirements for the degree of

DOCTOR OF PHILOSOPHY

Chair of Committee,	Duncan J. Maitland
Committee Members,	Akhilesh K. Gaharwar
	Daniel L. Alge
	Melissa A. Grunlan
Head of Department,	Michael McShane

May 2021

Major Subject: Biomedical Engineering

ABSTRACT

Shape memory polyurethane (SMP) foams have multiple adequate features to be utilized as a hemostatic device or an embolic device such as their unique shape recovery property, excellent biocompatibility, and rapid hemostatic property. SMP foams can be delivered to a targeted site with minimal invasiveness to treat severe hemorrhage or aneurysms. However, SMP foams have a few limitations such as slow degradation rate to match a wound healing timeline, insufficient fluid absorption, and the lack of X-ray visibility. It is also challenging to properly evaluate endovascular embolization device performance and train medical personnel for device deployment with current *in vitro* aneurysm models. In this dissertation, unique ways to improve the biodegradability, fluid absorption capacity, and X-ray visibility of SMP foams are illustrated. Also, the development of a living *in vitro* aneurysm platform using three-dimensional hydrogel printing technology is described. The biodegradability of the SMP foams was accelerated by adding ester-containing monomers in the foams which increased the degradation rate both oxidatively and hydrolytically while the thermal properties remained to be suitable for hemostatic use. Fluid uptake capacity was enhanced by synthesizing a SMP foam-hydrogel composite that maintains unique mechanical properties from SMP foam and high fluid absorption capacity from hydrogel. The composite could also expand quicker, and clot blood more rapidly compared to the foam. The radiopacity was introduced to SMP foams by adding both physical and chemical X-ray contrast agents into the foam structure. This enabled visualization of neurovascular scale foam via X-ray spectroscopy. An *in vitro* platform of aneurysm-bearing vascular

structure was built using gelatin-fibrin hydrogel of which the inner vessel walls were seeded with human cerebral microvascular endothelial cells (hCMECs). An embolization coil was deployed to the printed aneurysm sac using a catheter and the blood plasma clotting around the coils was monitored. The SMP foams with enhanced biodegradability, fluid uptake capacity, or radiopacity possess great potential as an effective hemostatic or embolization device for treatment of hemorrhage or aneurysms. Furthermore, the biomimetic *in vitro* aneurysm platform is a promising method for examining the biocompatibility and hemostatic efficiency of embolization devices.

ACKNOWLEDGEMENTS

I would like to thank Dr. Duncan Maitland for his unconditional support, technical guidance and strong leadership throughout my PhD years. Dr. Maitland has been a great supervisor who would not only care for the research but also sincerely care for his students' well-being as graduate students and their future career after graduation. Even after many failures of my experiments, or mistakes on my end, he never discouraged me, but he gave me the right measures and motivated me to do my best and overcome the difficult times. His compliments, feedback, and encouragement on my performance greatly inspired me to do better and work harder on my research. I would also like to acknowledge the other members of my committee, Dr. Akhilesh Gaharwar, Dr. Daniel Alge, and Dr. Melissa Grunlan for their support and guidance.

I would like to appreciate Dr. Mary Beth Monroe for being my first mentor when I joined the lab. She was an amazing mentor who I could visit frequently to ask questions on the experimental problems I faced and future direction of my study. She reassured me when my experiments kept failing, filling me with positive energy and powerful motivation. I would also like to express my sincere gratitude to Dr. William Hynes who was my mentor when I was doing a summer internship in Lawrence Livermore National Laboratory. He was a very passionate researcher who gave me motivations on my work and made me realize that I should pursue things that I love to do when I choose my career. He was a good listener as he tried to incorporate my ideas into the research no matter how trivial they were. The summer I had spent with him was very valuable time for me to learn new technical skills, new mindset, and to motivate

myself in pursuing my research. Dr. Landon Nash was a great collaborator and a mentor who gave me awesome feedback and support on my research.

I would also like to thank my lab mates in the Biomedical Device Laboratory that I was grateful to work with. Grace Fletcher was a great mentor for the first couple of years, teaching me how to synthesize polyurethane foams and how to troubleshoot any experimental problems. Samuel Briggs and Lance Graul started their PhDs at around the same time with me. They have been amazing friends of mine throughout my PhD years, sharing burdens, discussing experiments, and making me feel better whenever I was down for any reasons. Scott Herting and Tyler Touchet were awesome colleagues who were always very nice to help me with anything that I was struggling with. Achu Byju was a MacGyver in the lab fixing all the broken equipment and making whole new equipment out of nothing. Thomas Cheung was a great undergraduate researcher who helped my experiment in many ways. I also want to appreciate my dear friends, Meghan Scott and Alisa Isaac for making me laugh and enjoy PhD life.

Finally, I would like to thank my parents, Hee Sung Jang and Hyunsook Kang, and my brother, Jeyun Jang, for their unlimited love and support throughout my life and journey towards earning a PhD. I also want to show my great appreciation and affection towards Ho Yong Shin who has been my friend, my lover, my fiancé, and finally my husband throughout my PhD years. He has supported me emotionally and spiritually in whichever situation I was in. Last but not least, I would like to thank God for being with me the whole time, for giving me positive energy to overcome tough times and for all the wonderful people around me.

CONTRIBUTORS AND FUNDING SOURCES

Contributors

This work was supported by a dissertation committee consisting of Dr. Duncan Maitland, Dr. Akhilesh Gaharwar, Dr. Daniel Alge, and Dr. Melissa Grunlan of the Biomedical Engineering Department.

Dr. Monroe provided her idea for Chapter II on the biodegradable foam project as well as her mentorship throughout the project. Giriraj Lokhande who is a PhD student from Dr. Gaharwar's group was my collaborator who performed hydrogel coating on the SMP foams and carried out multiple characterizations including morphological analysis, hemostatic studies, and *in vitro* cell studies for Chapter III. The radiopaque foams used in this work for Chapter IV was based on Dr. Nash's previous work who had been my collaborator and a mentor from Shape Memory Medical for the radiopaque foam project. Tantalum elemental analysis of extraction solutions in Chapter IV was performed by the Legend Technical Services Inc. Dr. Hynes provided technical guidance and led the *in vitro* aneurysm platform project for Chapter V throughout and after my summer internship in Lawrence Livermore National Lab. Dr. Pepona and Dr. Randles from Duke University built a 3D computational fluid aneurysm model and analyzed fluid dynamics using flow simulations. All other work conducted for this dissertation was completed by the student independently.

Funding Sources

Biodegradable foam project for Chapter II was sponsored by U.S. Air Force under agreement number FA8650-18-2-6978. Radiopaque foam project for Chapter IV was supported by the NIH National Institute of Neurological Disorders and Stroke, grant number U01-NS089692. In vitro aneurysm project for Chapter V was supported by LLNL LDRD-20-ERD-013. LLNL-JRNL-807798

NOMENCLATURE

SAH	Subarachnoid hemorrhage
SMP	Shape Memory Polymer
BPC	Bare platinum coil
PCL-t	Polycaprolactone triol
HPED	N,N,N′,N′-tetrakis(2-hydroxypropyl)ethylenediamine
TEA	Triethanolamine
NVP	n-Vinylpyrrolidone
PEGDA	Polyethylene glycol diacrylate
AA	6-Aminocaproic acid
Gly	Glycerol
G	Glycine
PD	Pentanediol
HDI	Hexamethylene diisocyanate
IPA	Isopropyl alcohol
RO	Reverse osmosis
DI	Deionized
Gel-NS	Gelatin-nanosilicate hydrogel
HMSC	Human mesenchymal stem cell
ATIPA	5-Amino-2,4,6-triiodoisophthalic acid
AT_T	Tantalum loaded ATIPA foams
MPD	3-Methyl-1,5-pentanediol

HT	1,2,6-Hexanetriol
BEP	2-Butyl-2-ethyl propanediol
THF	Tetrahydrofuran
DMEM	Dulbecco's modified eagle medium
3D	Three-dimensional
PIV	Particle image velocimetry
hCMEC	Human cerebral microvascular endothelial cells
ECM	Extracellular matrix
TG	Transglutaminase
PLGA	Poly(D,L-lactide-co-glycolide)
WSS	Wall shear stress
DSC	Differential scanning calorimetry
DMA	Dynamic mechanical analysis
ATR-FTIR	Attenuated total reflectance-Fourier transform infrared
SEM	Scanning electron microscopy
ICP-OES	Inductively coupled plasma optical emission spectrometry

TABLE OF CONTENTS

Page

LIST OF FIGURES

Page

LIST OF TABLES

Page

CHAPTER I

INTRODUCTION AND SIGNIFICANCE OF THE RESEARCH*

Hemorrhage and the Current Hemostatic Treatments

Combat casualty studies showed that the cause of approximately 90% of potentially survivable deaths on battlefields was uncontrolled bleeding, and severe hemorrhage is the primary cause of battlefield mortality.[1]–[5] Current hemostatic treatments include the combined use of pro-coagulant-embedded compression gauze with tourniquets.[6] However, they are not effective for the treatment of deep and non-compressible wounds, which make up 67% of all hemorrhagic injuries.[7] In addition, long-term use of tourniquets involves serious complications, such as ischemia-reperfusion injury, which can lead to muscle necrosis and limb loss.[8] One of the recent methods developed to treat non-compressible wounds is injecting 92 small cellulose sponges (XStat™) into the wound site that expand by absorbing blood to put pressure on blood vessels in wound walls to stop further blood loss.[9] However, the sponges must be removed within four hours of injection due to inflammation issues. This removal requires painful reopening of the wounds and a 22-fold increase in surgical removal time

* Reprinted with permission from "Biodegradable shape memory polymer foams with appropriate thermal properties for hemostatic applications" by L. Jang, G. Fletcher, MB. Monroe, and D. Maitland, 2020. J Biomed Mater Res. 108:1281-1294, Copyright [2020] by John Wiley&Sons Inc.

compared to conventional gauze. Thus, it may not be practical in battlefield situations with long travel times to fixed-care facilities.[10]

Literature Review on Hemostatic Materials

Various forms (e.g., solid sheets, sponges, particles/fibers) of biomaterials (e.g., collagen, keratin, chitosan, polyurethane) have been investigated for use as an effective hemostat.[11],[12] Bal-Ozturk et al. reported chitosan/alginic acid/zinc oxide (CHI/AA/ZnO) nanostructured hydrogel sponges that could be used as an antibacterial hemostat. ZnO in the sponges increased antibacterial properties, and the hydrogel sponge was biocompatible *in vitro* and *in vivo*.[13] Fathi and colleagues synthesized zeolite-loaded alginate-chitosan hydrogel beads where zeolite served as blood absorbent. The hydrogel beads showed good erythrocyte adhesion and minimal *in vitro* cytotoxicity.[14] An oxidized nanofibrillar cellulose (ONFC)-chitosan (Ch) sponge from Sukul et al. showed good biocompatibility *in vitro* and higher hemostatic ability compared to ONFC.[15] However, these hydrogel sponge and bead systems are for topical hemostatic use and are not currently feasible for treatment of non-compressible wounds.

Cerebral Aneurysms

Aneurysms, localized dilations or "ballooning" of arterial vessel walls in the brain due to the abnormal weakening of the muscular layer of a blood vessel, affect 2-3% of adults and their rupture leads to subarachnoid hemorrhage (SAH).[16] Approximately 85% of all SAHs are due to the rupture of saccular aneurysms and most

of the cases involve debilitating or fatal complications such as permanent neurological deficit or death.[16],[17] The highly detrimental effects which can arise from an aneurysm rupture highlights the critical need for the development of devices that can effectively prevent the rupture and for testing the safety and effectiveness of those devices before clinical use.

Current Treatments of Cerebral Aneurysms

Surgical clipping has been a long-standing standard treatment method for aneurysms.[18],[19] During surgical clipping, a clip is placed over the neck of an aneurysm to isolate it from the main bloodstream. However, since surgical clipping involves highly invasive intracranial surgery and some aneurysms are located in inaccessible regions within the brain, endovascular treatment using bare platinum coils (BPCs) has become an increasingly employed alternative. BPCs are delivered into the aneurysm using a microcatheter. Once the aneurysm is packed with coils, a thrombus forms which leads to the occlusion of blood flow within the aneurysm. In highly successful endovascular treatments, regrowth of the endothelium across this thrombus is observed at the neck of the aneurysm.[20],[21] Endovascular treatment using coils possesses several advantages over surgical clipping such as lower invasiveness, decreased expense and duration of hospitalization, shorter patient recovery times, and limited post-surgical complications both in ruptured and unruptured aneurysms.[19],[22] However, BPCs have limitations in that the inertness of coils limits tissue response which can lead to form partially

thrombosed aneurysms,[23] and their low packing density can result in coil compaction and further recanalization of aneurysms in 21-34% cases.[24],[25]

Shape Memory Polyurethane Foam as a New Treatment Material for Hemorrhage and Cerebral Aneurysms

Shape memory polyurethane (SMP) foams demonstrate great potential in hemostatic and embolic applications due to their high biocompatibility, high porosity, large surface area, and unique shape retention property.[6],[26] SMP foams have a highly porous primary shape that can be compressed into a low volume secondary structure when heated above their glass transition temperature (T_g). The secondary shape can be locked by cooling and maintained until actuated by a thermal stimulus. Our group developed low-density SMP foams with high volume expansion (up to 70X) for use as an embolic device in aneurysm treatments.[27] The T_g of these SMP foams ranges from 45 ˚C to 70 ˚C in dry conditions,[27] and it can be adjusted to a desired range by changing the polymer crosslink density. Upon plasticization with water, the T_g is reduced to below body temperature, depending upon network hydrophilicity and hydrogen bond disruption.[28] This unique feature enables minimally invasive delivery of a compressed foam into a deep wound site or into an aneurysm sac and its thermal actuation at body temperature. Once actuated, the foam would expand and fill the wound or the aneurysm sac. The combination of thrombogenic surface chemistry and high surface area-to-volume ratio results in rapid blood clotting within the foam.[29],[30] Previous *in vivo* studies demonstrated that SMP foams attain rapid blood clotting in a porcine hind limb

vessel within 90 seconds.[31] Furthermore, SMP foams maintained biocompatibility over up to 180 days with complete healing and minimal inflammatory response in a porcine aneurysm model.[32] SMP foam material was also used in a clinical study to embolize a false lumen of a post-dissection aneurysm in a 69-year-old patient, which resulted in complete and stable thrombosis of the false lumen at 15 months.[33] These properties make SMP foams a promising platform material for a biocompatible hemostat as well as an effective embolization material for aneurysms.

Limitations of Current Shape Memory Polyurethane Foams

Biodegradability of the SMP foam is a desirable property in a range of applications, such as hemostats, cell scaffolds, and embolic devices. In hemostatic applications, SMP foams with biodegradation rates that complement the wound healing timeline would eliminate the need for a secondary removal procedure, thus facilitating the healing response. SMP foams with controlled biodegradability will also possess potential for controlled drug release to provide localized pain relief, minimize immunogenic or infection issues, and/or promote healing. However, conventional SMP foams have slow degradation rates *in vitro* and *in vivo* due to the absence of fast-degrading chemical bonds such as esters or anhydrides. Thus, biodegradable SMP foams that also can maintain critical properties of SMP foams need to be further studied and developed.

Another limitation of SMP foam is that it has a poor capacity for fluid absorption, which limits its use as a hemostatic agent.[34] Blood and body fluid

absorption is critical for hemostatic materials in rapid blood clotting and wound healing.[35] Hydrogels have been extensively used and researched as wound dressings due to many advantages including: the ability to absorb and prevent loss of body fluids, barrier against bacteria, oxygen permeability, and potential to deliver drugs.[36] Thus, hydrogel coating on SMP foam could address the limitation that SMP foams possess by enhancing the fluid uptake capacity as well as maintaining the unique mechanical properties of SMP foam.

Lastly, SMP foams do not have inherent radiopacity, which limits their clinical utility as endovascular devices since X-ray visualization is necessary for safely delivering the device to a target site and properly packing devices into an aneurysm. One approach to circumventing the lack of SMP X-ray visibility is to incorporate high-Z markers into the device design. BPCs were used as a backbone for SMP foams to visualize the foam devices being delivered to the aneurysm sites.[37],[38] However, the use of BPC restricts the aneurysm lesion shrinkage when the collagenous connective tissue formed around the device gets contracted in the late healing stage, which would delay the overall healing.[39] Therefore, there is a great need for the development of a foam-only device with appropriate radiopacity.

Significance of *In Vitro* Aneurysm Models

Engineering an *in vitro* aneurysm model is desirable to test the next-generation endovascular medical devices for training practitioners how to deploy these devices, to develop accurate computational simulations, and for understanding how effectively

treatments induce clotting or lead to a healing response.[40]–[45] Previously, silicone or clear liquid resin molding was used to simulate human cerebral aneurysms using the lost wax technique. In this approach, silicone or resin is poured over wax models of human vascular pathologies inside a transparent plastic box to eventually create a silicone hollow vascular channel that is compatible with X-ray and Magnetic Resonance Imaging (MRI) and amenable to a visualization of vascular flow.[43] However, silicones or the resins do not have physiologically relevant modulus of a brain which makes it challenging to obtain reliable results for flow around the aneurysm or cellular responses after the embolization treatment. Therefore, biomimetic *in vitro* aneurysm models that have physiologically relevant stiffness and cellular structure of a brain need to be developed to test clotting and healing efficacy of endovascular devices.

Objectives of the Dissertation

The objectives of this dissertation are to improve multiple essential properties of SMP foams to be used as a hemostatic or embolic material and to build an *in vitro* living aneurysm platform to test such embolic devices. This dissertation illustrates the enhancement of biodegradability and fluid uptake capacity of SMP foams for use as a hemostatic material to eliminate the material removal step and to accelerate the clotting or healing response by absorbing more blood or exudate from the wound. The radiopacity of SMP foams is increased in the study to visualize implanted foam inside the body with X-ray for use in hemorrhage or aneurysm treatment. In addition, the dissertation describes making an *in vitro* platform of aneurysm-bearing vascular

structure to be used as a training model for medical personnel in endovascular device deployment or to evaluate new-generation embolization devices in their clotting or healing performance.

CHAPTER II

BIODEGRADABLE SHAPE MEMORY POLYMER FOAMS WITH APPROPRIATE THERMAL PROPERTIES FOR HEMOSTATIC APPLICATIONS*

Introduction

Biodegradable hemostats are largely investigated for the treatment of deep and non-compressible wounds since they eliminate the need for secondary removal surgery and facilitate wound healing after the treatment. Li et al. developed biodegradable porous chitosan microspheres.(46) The porous microspheres showed improved *in vitro* and *in vivo* hemostatic properties compared to compact chitosan particles as the pores trapped more red blood cells and platelets. *In vitro* enzymatic degradation analysis demonstrated that these microspheres had 40% mass loss in four weeks. Jiang et al. synthesized biodegradable collagen sponges that demonstrated good histocompatibility *in vivo*, and good hemostatic effect when topically applied on bleeding liver and ear artery.(47) However, the chitosan microspheres and collagen sponges do not have the desirable viscoelastic properties of SMP foams, which led to difficulties in delivery into

---

* Reprinted with permission from "Biodegradable shape memory polymer foams with appropriate thermal properties for hemostatic applications" by L. Jang, G. Fletcher, MB. Monroe, and D. Maitland, 2020. J Biomed Mater Res. 108:1281-1294, Copyright [2020] by John Wiley&Sons Inc.

deep wounds and inadequate pressure on the wounds, indicating that they are not suitable for treatment of non-compressible wounds.

Singhal et al. designed low density biodegradable SMP foams using ester-containing polycaprolactone triol (PCL-t, M_n = 900 Da) as one of the monomers in the polyurethane foam network.[48] Even though the SMP foams showed good shape recovery and controlled biodegradability *in vitro*, their dry T_g's were in the range of -19.1 °C - 28.5 °C, which is too low to be clinically viable (i.e., the foams would not stay compressed during storage, reducing the ability to insert a compressed foam into a tunneling wound). This low T_g range was due to the increased free volume in the amorphous polymer network, resulting from the longer branches of PCL-t compared to the traditionally used monomer polyols, N,N,N′,N′-tetrakis(2-hydroxypropyl)ethylenediamine (HPED) and triethanolamine (TEA).[48]

In this work, we synthesized ester-containing trifunctional monomers and incorporated them into our group's previously developed low density SMP foam system. Trifunctional esters were made by reacting short chain bifunctional monomers (i.e., 6-aminocaproic acid (AA) or glycine (G)) with triols. AA is used clinically to treat acute bleeding; its successful use in patients indicates its biocompatibility, and its incorporation into the foams could increase hemostatic properties. G is an amino acid that is naturally present in our body, thereby providing foams with a natural and biocompatible degradation byproduct. The overall aim of this study was to synthesize biodegradable SMP foams while maintaining the appropriate thermal properties for battlefield use (dry $T_g > 50$ ˚C and wet $T_g < 37$ ˚C).

Materials and Methods

Materials

Triethanolamine (TEA; 98%, Alfa Aesar Inc.), hexamethylene diisocyanate (HDI; TCI Chemicals), DC 198, DC 5943, DC5043, BL-22, T-131, and Enovate (Evonik, Essen, Germany) were used as received. All other chemicals were purchased from Sigma Aldrich and used as received.

Esterification of triols

To increase the biodegradability of SMP foams, ester linkages were introduced onto foaming triols, triethanolamine (TEA) and glycerol (Gly), that have been previously used to fabricate SMP networks with good thermal properties.[27],[49] Chlorotrimethylsilane (3 mol. eq.) was slowly added to 6-aminocaproic acid (AA, 1 mol. eq.) in a round bottom flask with a magnetic stirring bar. The solution was stirred for 30 minutes at room temperature. TEA (0.5 or 1 mol. eq.) or Gly (1 mol. eq.) was added to the mixture, which was then allowed to react overnight at room temperature. Excess solvent was removed using rotary evaporation, completing synthesis of three different ester-containing monomers: TA(2) (TEA:AA = 1:2 molar ratio), TA (TEA:AA = 1:1 molar ratio), and GA (Gly:AA = 1:1 molar ratio).[50] The same esterification method was applied to glycine (G, 1 mol. eq.) and TEA (1 mol. eq.) to form TG (TEA:G = 1:1 molar ratio). The chemical structures of the synthesized products were confirmed using Fourier transform infrared (FTIR) and nuclear magnetic resonance (^{1}H-NMR) spectroscopy. For FTIR analysis, controls and synthesized products were solvent-cast on KBr pellets and

dried overnight under vacuum. FTIR transmission spectra were obtained by Bruker TENSOR 27 spectrometer. ^{1}H-NMR spectra (Mercury 300 MHz spectrometer) were obtained using dimethyl sulfoxide-d_6 (dDMSO) solvent and TMS signal as an internal reference.

^{1}H NMR (dDMSO; ppm): **TA(2)**: 1.33 (m, -CH2C***H2***CH2CH2NH2, 4H), 1.56 (m, -C***H2***CH2C***H2***CH2NH2, 8H), 2.33 (t, -CH2C***H2***COO-, 4H), 2.77 (m, -CH2C***H2***NH2, 4H), 3.38 (m, -OCH2C***H2***N-, 6H), 3.81 (t, -OC***H2***CH2N-, 4H). **TA**: 1.32 (m, -CH2C***H2***CH2CH2NH2, 2H), 1.55 (m, -C***H2***CH2C***H2***CH2NH2, 4H), 2.32 (t, -CH2C***H2***COO-, 2H), 2.75 (m, -CH2C***H2***NH2, 2H), 3.33 (t, -OCH2C***H2***N-, 2H), 3.79 (t, -OC***H2***CH2N-, 2H). **TG**: 2.54 (t, -NC**H2**CH2OH, 4H), 3.34 (m, -COOCH2C***H2***NCH2C***H2***OH, 6H), 3.68 (t, -COOC***H2***NH2, 2H), 3.80 (m, -COOC***H2***CH2NCH2CH2O***H***, 4H), 8.37 (t, -CH2N***H2***, 2H). **GA**: 1.23 (m, -C***H2***CH2CH2NH2, 2H), 1.52 (m, -C***H2***CH2C***H2***CH2NH2, 4H), 2.17 (m, -C=OC***H2***CH2-, 2H), 2.72 (m, -CH2C***H2***NH2, 2H), 3.53 (m, -OC***H2***C***H***O***H***C***H2***O***H***, 7H).

SMP foam synthesis

Four different ester-containing SMP foams were fabricated using TA(2), TA, TG, and GA. Four corresponding control foams were fabricated using equivalent stoichiometric amounts of TEA or Gly. All foam syntheses followed the traditional two-step foaming method.[27] First, an isocyanate (NCO) premix was prepared in a desiccated glovebox by adding appropriate molar ratios of N,N,N′,N′-tetrakis(2-hydroxypropyl)

ethylenediamine (HPED), unmodified/modified triol (TEA , Gly, TA, TA(2), TG, or GA), 3-methyl-1,5-pentanediol (PD; only for G25 and GA25 foams to enhance solubility), and HDI. The premix was thoroughly mixed and then placed in an oven running a cure cycle up to 50°C for 2 days. (ramp rate 20°C/h, held isothermally at 50°C for 36h, passive cooling to 25°C). Second, the hydroxyl (OH) mix was prepared by mixing the remaining HPED, unmodified/modified triol, PD, and water with a FlackTek Speedmixer at 3400 rpm for 30 s. The OH mix was added to the cured NCO premix along with surfactants (DC 198, DC 5943, and DC 5043) and catalysts (T-131 and BL-22 (Evonik)) and mixed with the Speedmixer (3400 rpm, 30 s). Enovate, the physical blowing agent, was added in this step to select foams to enable pore size matching between ester-containing SMP foams and their controls. Then, the mixture was poured into a plastic mold and foamed at 50 °C for 3-6 min. The detailed foam compositions are shown in **Table II-1**.

Table II-1. Summary of SMP foam compositions. (Grey rows indicate the control foams for each ester-containing foam below)

Sample ID	HDI (wt%)	HPED (wt%)	TEA (wt%)	TA(2) (wt%)	TA (wt%)	TG (wt%)	Gly (wt%)	GA (wt%)	PD (wt%)	Water (wt%)	DC198 (wt%)	DC5943 (wt%)	DC5043 (wt%)	T-131 (wt%)	BL-22 (wt%)	Enovate (pph)
T30	60.9	14.1	4.1	-	-	-	-	-	-	3.2	4.0	3.0	-	0.5	1.3	-
TA(2)30	50.1	16.5	-	12.1	-	-	-	-	-	2.2	3.9	2.9	-	0.5	1.3	-
T40	61.6	12.2	5.5	-	-	-	-	-	-	2.7	4.0	3.0	-	0.5	1.3	-
TA40	49.3	17.0	-	-	13.5	-	-	-	-	2.2	4.0	3.0	-	0.5	1.3	7.5
T60	62.8	13.1	13.4	-	-	-	-	-	-	2.7	4.0	3.0	-	0.03	0.6	5.0
T40TG20	62.1	12.5	8.4			5.9	-	-	-	2.6	3.9	3.0	-	0.5	1.3	-
G25	63.7	10.5	-	-	-	-	2.2	-	4.3	2.8	4.0	3.0	-	0.01	0.3	2.5
GA25	61.1	12.7	-	-	-	-	-	4.9	2.6	2.6	-	-	4.7	0.02	0.6	5.1

Foam density, gel fraction and pore morphology

Foam samples were conditioned before all characterizations. Foam samples (1x1x1 cm^3) were pressed between two Teflon-coated stainless steel plates (Carver hot press) to a thickness of 5 mm at 100°C for 5 min using a 5 mm metal rod spacer. Then the foam was cleaned with water and isopropyl alcohol (IPA) repeatedly according to a previously reported protocol to remove any residual foaming additives.[28] After drying the foam under vacuum at 50°C overnight, the core foam density was measured as sample mass divided by volume measured by calipers (n=5) and was averaged for each foam composition.

For gel fraction calculations (n=3), the original mass of a 1 cm^3 foam was recorded. The foam was sonicated in IPA (1:20 volume ratio) for 30 minutes three times using fresh IPA each time. The foam was dried under vacuum at 100°C overnight, and the dry mass was measured. Gel fraction was calculated using the equation (1) below.

$$Gel\ fraction\ (\%) = \frac{F_C}{F_0 - F_{CWS}} \quad (1)$$

Where F_c is the foam mass after cleaning, F_0 is the foam mass before cleaning, and F_{CWS} is the mass of catalysts, water, and surfactant used in foam synthesis (i.e. foam components that are not part of the final network).

Pore structure was analyzed using scanning electron microscope (SEM; JCM-5000 Neoscope, JEOL) images. The diameters of 15 pores were measured from three foam sample images using ImageJ software.

Differential scanning calorimetry

Thermal properties of the SMP foams were analyzed using differential scanning calorimetry (DSC Q200, TA Instruments). To measure dry glass transition temperature (T_g), cleaned foam samples (2-4 mg, n = 3) were loaded into TZero Aluminum pans. Samples were equilibrated at -40°C, heated to 120°C with a ramp rate of 10°C/min and an equilibration time of 1 min at the end of each heating/cooling cycle. A second heating cycle was used to determine dry T_g. For wet T_g, foam samples (2-4 mg, n = 3) were immersed in 50°C water for 30 min. Water was removed from the foam using a laboratory wipe to ensure that the mass of water uptake was kept less than 10% of the original foam mass. The same temperature range and the ramp rate with dry T_g was used for wet T_g measurement. The first cycle was used to measure the wet T_g. Glass transitions were calculated using the Pyris software according to the half-height method.

Shape memory behavior

Foams were punched into cylindrical shapes (1 cm diameter, 1.2 cm length). A nickel-titanium wire was penetrated through the center of the foam along its length. The initial diameters of the foams were measured using ImageJ. The threaded cylindrical foams were placed inside an ST 150-42 stent crimper (Machine Solutions, Flagstaff) that was previously heated up to 100 °C. After heating the foams for 15 min, the foams were radially crimped to a 2 mm diameter. After the crimper was cooled down to 25 °C, the crimped foams were removed and stored in a vacuum chamber at least for 24 hours to ensure that they maintain their secondary shapes. The diameters of the crimped foams

were measured with ImageJ. The crimped foams were then submerged into 37°C water, and images were taken at regular time points (every 30 s over 0-5 min, every 1 min over 5-10 min, and every 5 min over 10-20 min) to measure the increasing diameter of the foams. Diameters at three evenly spaced locations along the foam length were measured and averaged (n = 5). Percent diameter recovery was calculated using equation (2) below.

$$\text{Diameter recovery (\%)} = \left(\frac{recovered\ diameter}{initial\ diameter}\right) \times 100 \quad (2)$$

Tensile testing

Rectangular foam samples (30 mm x 12 mm x 3 mm) were prepared, and the two shorter ends were epoxied to two wooden blocks. The epoxy was allowed to cure overnight. Clamps on MTS Insight 30 Universal Tensile Tester were firmly tightened on the wooden blocks. The foam samples were subjected to strain to failure experiments at a constant rate of 5 mm/min at 25°C.

Degradation analysis

Cleaned foam samples were prepared as 1 cm^3 cubes. Initial sample weights were measured and recorded. For accelerated hydrolytic degradation analysis, samples (n = 5) were submerged into 1N NaOH at a 1:20 volume ratio (foam: NaOH solution). Samples (n = 5) were immersed in 20% hydrogen peroxide (H_2O_2) at a 1:20 volume ratio (foam: H_2O_2 solution) for accelerated oxidative analysis. All foams were stored in degradation solutions at 37°C. Solutions were changed once every 3 days to ensure that pH and ion

concentration were stable throughout the study. At select time points, foams were washed with reverse osmosis (RO) water and ethanol, and they were dried completely at 50°C under vacuum before re-weighing and returning to fresh degradation solution. Attenuated total reflectance-FTIR (ATR-FTIR) and SEM imaging were used at set time points to analyze degraded foam surface chemistry and pore morphology, respectively.

Results

Synthesis of trifunctional esters and ester-containing SMP foams

TA(2), TA, TG, and GA esters were synthesized by reacting 1 equiv. hydroxyl group in TEA or Gly with 1 equiv. carboxylic acid group in AA or G. The synthesis was confirmed using ^{1}H-NMR (**Figure II-1a**) and FTIR (**Figure II-1b**). NMR spectra showed successful esterification of the reactants, which was further confirmed by FTIR. In the FTIR spectra, carbonyl peaks from the carboxylic acid groups of AA (1708 cm^{-1}) and G (1627 cm^{-1}) were shifted to 1730 cm^{-1} in TA(2), TA, TG, and GA, which indicates successful formation of ester linkages. Compared to Gly and TEA, a sharp N-H stretch peak (3348 cm^{-1}) was observed in TA(2), TA, TG, and GA, which confirmed functionalization of TEA and Gly with AA or G. The ester peaks of TA(2) and TA were normalized to compare the ester content between the two monomers by observing other peak intensities. TA had much higher peak intensities on all the other chemical bonds than TA(2), which indicated that TA(2) has higher ester content compared to TA.

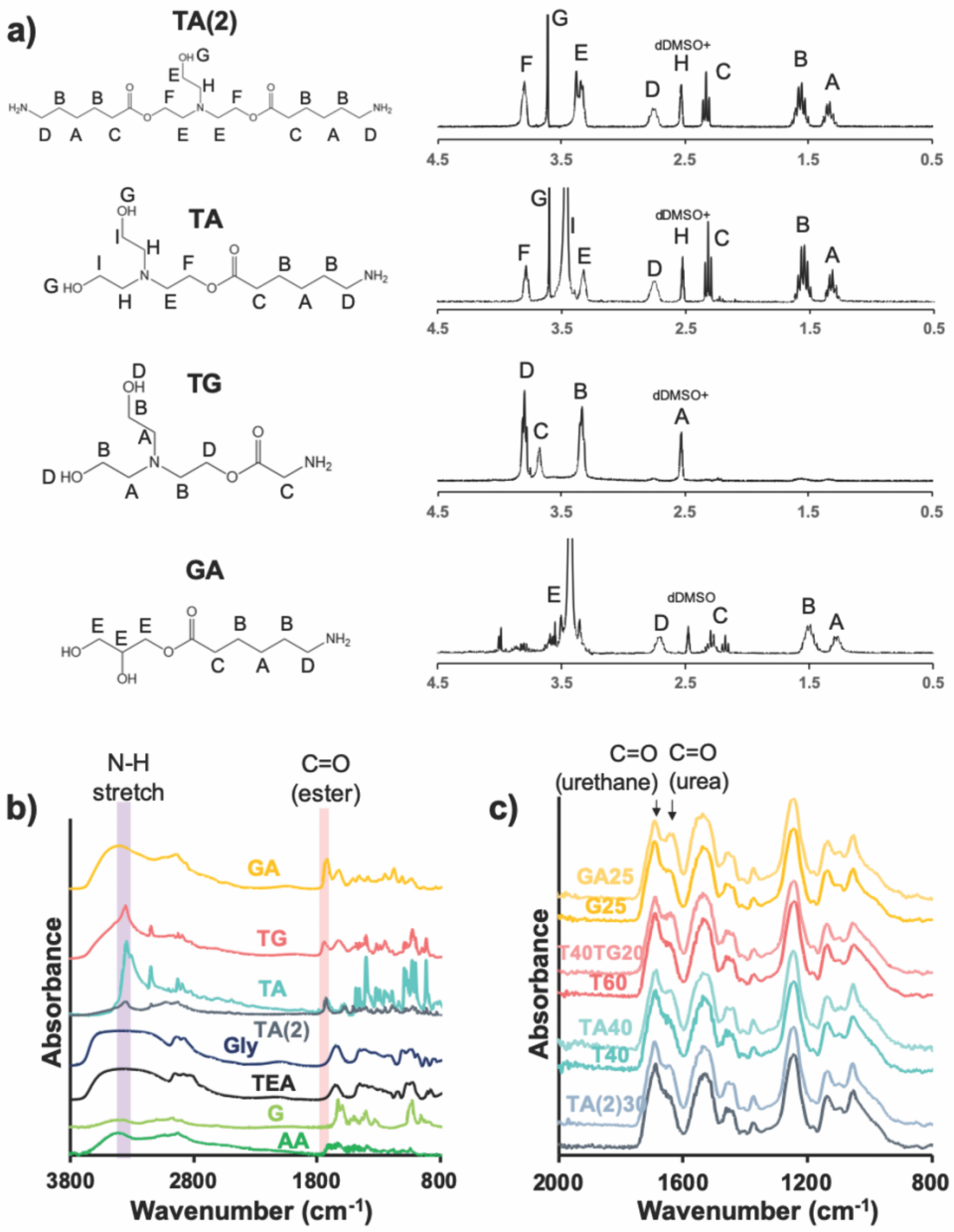

Figure II-1. Chemical characterization of synthesized esters and ester incorporated SMP foams. a) Chemical structure and 1H-NMR spectra of the synthesized esters. b) FTIR spectra of synthesized esters (TA(2), TA, TG, and GA) compared to triols (Gly, and TEA) and bifunctional monomers (G, and AA). c) FTIR spectra of ester-containing SMP foams (TA(2)30, TA40, T40TG20, and GA25) compared to control SMP foams (T30, T40, T60, and G25).

Characterization of SMP foams

Structural properties

Foam densities of cleaned SMP foams are shown in **Figure II-2a**. The densities for the ester-containing foams (0.030–0.076 g/cm^3) were higher than their controls (0.022–0.049 g/cm^3) due to shorter rising heights of the ester-containing foams than those of the control foams. Shorter rising height was attributed to faster reactions between amines on ester-containing monomers and isocyanates, and it correlates with previous results of polyurethane-urea foam synthesis.[51],[52] Additionally, the NCO premixes of ester-containing foams had to be more viscous than the controls to prevent collapse during foaming, which further restricted foam rise. Pore sizes of the ester-containing foams were optimized to match those of the control foams using different amounts of physical blowing agent (Enovate) in the foaming process (**Figure II-2b**). ANOVA single factor test was performed to confirm that the pore sizes of each ester-containing foam and its control are not significantly different ($p > 0.1$). The pore morphologies can be viewed in SEM images in **Figure II-2d**. Interestingly, TA(2)30, TA40, and T40TG20 had highly interconnected, open porous structure while all other foam compositions had morphologies with mostly closed pores. Gel fractions of the foams are shown in **Figure II-2c**. All foams showed high gel fractions of over 90%. In general, ester-containing foams had lower gel fractions than their controls, which is likely due to inhomogeneity in the synthesized monomers.

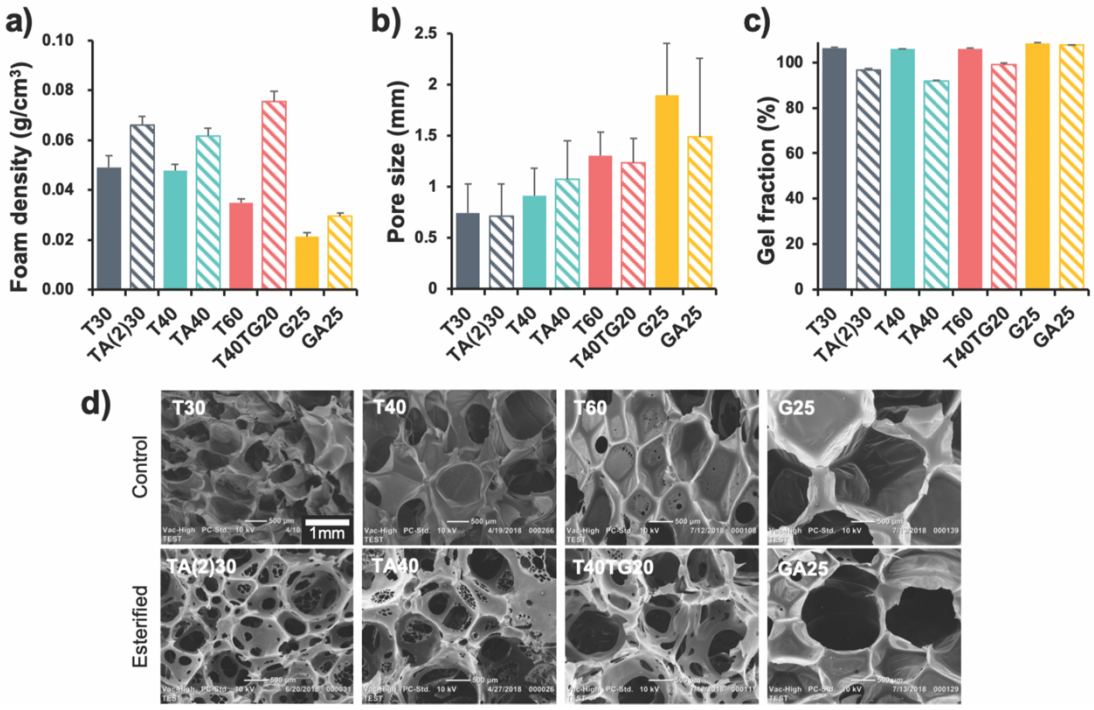

Figure II-2. Structural properties of synthesized SMP foams. a) Foam density of cleaned SMP foams (n=3). b) Average pore sizes of SMP foams (n=15) measured using ImageJ. Pore sizes between each control and ester-containing foam are not significantly different ($p > 0.1$). c) Gel fraction measured after RO water and IPA cleaning step (n=3). d) Representative SEM images of SMP foam cross sections. (Scale bar on T30 SEM image applies to all images.)

Thermal properties

The glass transition temperatures (T_g) of dry and water-plasticized SMP foams are shown in **Figure II-3a**. Dry T_g's of the eight different foam compositions were all in the range of 60 – 70 ˚C, and wet T_g's were all in the range of 14 - 20 ˚C. This result indicates that the modification of TEA or Gly using short chain monomers, AA or G, had a minimal effect on the thermal properties of the synthesized SMP foams, which was a primary goal in this work and represents a step forward over the previous generation of ester-containing SMP foams.[48] Dry T_g over 60 ˚C allows for storage of foams in their

compressed secondary shape in battlefield conditions where the temperatures could reach up to 50 ˚C in summer (e.g. in Iraq). Wet T_g below 20 ˚C allows for foam actuation in body temperature (37 ˚C) blood when the compressed foams are injected into the bleed site. **Figure II-3b** shows that all foam compositions have a single T_g, which indicates that the polymer network is homogeneous.

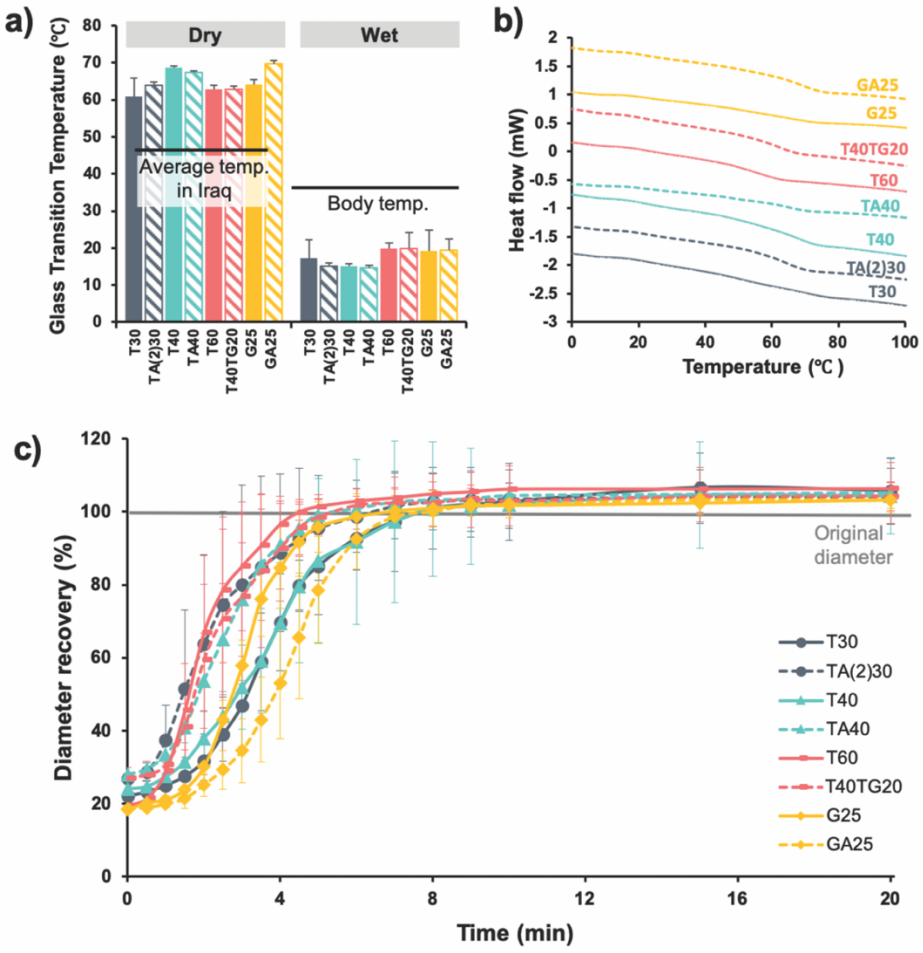

Figure II-3. Thermal and shape memory characterizations of SMP foams. a) Dry and wet T_g of SMP foams measured by differential scanning calorimetry (DSC). (n=3) b) Representative heat flow spectra of dry SMP foams. (Second heating cycle is shown.) c) Shape recovery profiles of crimped SMP foams immersed in RO water at 37 °C as a function of time.

Shape memory behavior

Radially crimped cylindrical foam (original diameter: 1 cm, length: 1.2 cm) expansion profiles in 37 ˚C RO water are shown in Figure II-3c. The expansion test was performed to analyze the shape recovery behavior of the foams in physiological conditions. The initial crimped diameters of the foams were 18-28% of the original diameters. G25 (18.4%) and GA25 (18.6%) had smaller crimped diameters compared to other foams due to their larger pore sizes and lower foam densities. TA(2)30 (27.0%) , TA40 (28.1%), and T40TG20 (26.8%) had larger crimped diameters due to higher foam densities and stiffnesses (Table 2). Among TEA-based control foams, T60, which has the lowest theoretical crosslink density, showed the fastest expansion profile, while that of highly crosslinked T30 was the slowest. TA(2)30 and TA40 exhibited faster expansion compared to their controls. This result is hypothesized to occur due to the asymmetry of the synthesized TA(2) and TA monomers, which provided an irregular network that enabled faster water plasticization of bonds within the network. On the other hand, T40TG20 and GA25 had slower expansion rates than their controls, which is attributed to stronger hydrogen bonds between chains around the urea linkages that slow water plasticization. In addition, the introduction of aminocaproic acid increases the hydrophobicity of the foam, which likely further slowed expansion in the GA25 foam system in wet conditions. It was noteworthy that all foam compositions recovered to their full volume within 4-8 minutes. Many trauma research data suggest that early treatment of non-compressible hemorrhage within the first 30 min can significantly

increase patient survival rate.[53],[54] Thus, the rapid expansion profiles observed here are promising for quick application of a hemostat to a bleed site.

Mechanical properties

Tensile testing was performed on the SMP foams (30 mm x 12 mm x 3 mm) to measure their mechanical properties (**Table II-2**). In comparing T30, T40, and T60 control foams, Young's modulus decreased and strain at break increased as TEA (triol) content was decreased and replaced with HPED (tetraol). Namely, the TEA:HPED ratios of T30, T40, and T60 were decreased (3:7, 4:6, and 6:4, respectively), resulting in a lower crosslink density and less stiff network. The effect of relative HPED content resulted in a similar trend among the ester-containing foams (decreased Young's modulus and increased strain at break with reduced HPED content).

Ester-containing foams showed 3.3-5.9 times higher Young's moduli compared to their controls, which can be attributed to a combination of chemical and physical properties. The urea linkages formed during reactions between amines on ester-containing monomers and isocyanates have increased hydrogen bonding capabilities and therefore can serve to increase foam stiffness. The faster reaction between amines and isocyanates also restricted foam rise during synthesis, which increased foam densities and provides a stiffer scaffold.

For G25 and GA25 foams, 3-methyl-1,5-pentanediol (PD) was added to the premixes to increase the solubility of Gly or GA in the mixture. Adding this diol to the foam network reduced crosslink density, which translated to a decreased Young's

modulus compared to TEA-based foams. GA25 foams had increased stiffness relative to G25 foam, which was again attributed to urea linkages in the polymer network. In general, modulus of thermoset polymer is highly related to its crosslink density, which is typically co-dependent on both T_g and pore size.[55],[56] Therefore, it is critical to note that mechanical stiffness of ester-containing foams could be improved significantly while thermal properties and pore sizes were maintained similar to the controls, providing a new mechanism to decouple stiffness from thermal and physical properties. This result could open up new application possibilities for the ester-containing SMP foams to be used in high stiffness applications, such as cartilage or bone tissue engineering.

Increased modulus was observed with corollary decreased strain at break for all foam compositions, as expected. However, the increases in stiffness observed in ester containing foams relative to controls (3.3-5.9 fold increases) generally outweighed the reductions in strain at break (1.5-3.2 fold decreases).

Table II-2. Mechanical properties of SMP foams measured by MTS tensile tester. (n=5)

Sample ID	Young's modulus (MPa)	Strain at break (%)
T30	3.0 ± 1.5	12 ± 3
TA(2)30	13.3 ± 5.2	5 ± 3
T40	1.9 ± 1.0	19 ± 9
TA40	6.3 ± 1.2	6 ± 2
T60	0.9 ± 0.4	48 ± 14
T40TG20	5.3 ± 1.7	16 ± 4
G25	0.8 ± 0.2	31 ± 10
GA25	2.6 ± 0.5	21 ± 9

Gravimetric degradation analysis

Hydrolytic and oxidative degradation of SMP foams were analyzed using gravimetric measurement. Remaining masses of 1 cm^3 foam samples were measured every 6 days in an accelerated hydrolytic condition (1N NaOH; **Figure II-4a**) or in an accelerated oxidative condition (20% H_2O_2; **Figure II-4b**) over 90 days. In the basic hydrolytic solution, TA40 and TA(2)30 had significant mass loss after 90 days. Specifically, TA40 demonstrated 43% mass loss while its control (T40) had 8% mass loss, and TA(2)30 demonstrated 15% mass loss while the T30 control showed 9% mass loss. Other foam compositions showed similar mass loss of 9-10% on day 90. The trends in degradation rates have a general correlation with the theoretical ester content in each foam composition. The theoretical ester content was calculated by dividing the theoretical molar number of ester groups by the molar number of hydroxyl and amine groups used in the polymer network and provides an indication of the number of crosslink sites that are adjacent to ester linkages. The calculated ester content was 14.2% for TA(2)30, 10.1% for TA40, 8.3% for GA25, and 6.7% for T40TG20. The increased mass loss of TA40 relative to TA(2)30 is attributed to increased pore size/surface area and reduced gel fraction (i.e., decreased crosslinking efficiency) in TA40 foams. In general, these results indicate that ester content can be used to tune hydrolytic degradation rates of SMP foams. The hydrolytic degradation rates were slower than expected, which is attributed to the relatively high hydrophobicity of the foam network[57] that prevents effective water penetration and subsequent hydrolytic breakdown of ester linkages.

For the oxidative degradation study, more significant changes in mass were observed. All ester-containing foams exhibited faster degradation compared to their controls. TA40 showed the fastest degradation rate until day 66, after which the degradation rate of TA(2)30 surpassed that of TA40. By day 90, TA(2)30, TA40, and GA25 were completely degraded while remaining masses of 8.6% for T40TG20, 25.9% for T40 and T60, 31.5% for T30, and 66.0% for G25 were calculated. It is noteworthy that G25 had the slowest degradation rate, which is due to the oxidatively stable structure of Gly. Previous research has demonstrated that in oxidative conditions, the tertiary amines in TEA and HPED are oxidized to amine oxide to form primary amines, carboxylic acids, and aldehydes.[58] This research explains why the control TEA-based foams (T30, T40, and T60), which contain higher percentage of tertiary amines, are more susceptible to oxidation than the Gly based foam (G25).

The oxidative degradation rates also correlate roughly with theoretical ester content, with similar overall trends to those observed in the hydrolytic degradation study. This result can be attributed to two possible mechanisms: (1) Oxidation of ester linkages can occur when an oxygen attacks the alpha carbon of the carbonyl group, resulting in the cleavage of the C-C bond to form carboxylic acid and aldehyde[59] and/or (2) Oxidative degradation of the tertiary amines by H_2O_2 facilitates water penetration into the scaffolds to hydrolyze ester linkages, providing a complementary degradable system with a tunable and faster degradation rate in oxidative conditions.

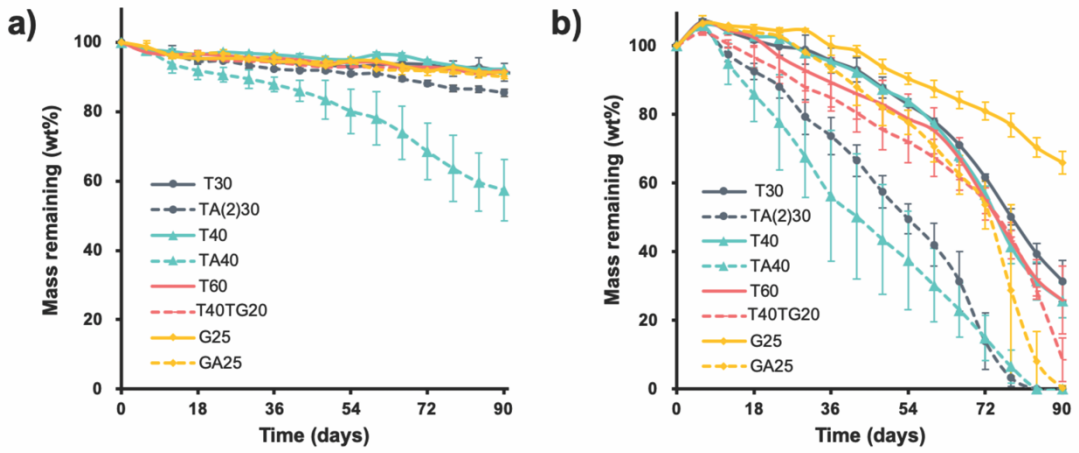

Figure II-4. Accelerated hydrolytic and oxidative degradation profiles of SMP foams over 90 days (n=3). a) Mass change of SMP foams in 1N NaOH at 37 °C. b) Mass change of SMP foams in 20% H_2O_2 at 37°C.

Analysis of degraded foams

Foams were analyzed every 18 days up to 90 days using ATR-FTIR and SEM during the degradation process. **Figure II-5a** shows the FTIR spectra of foams at 0 and 90 days of hydrolytic degradation. In general, despite significant mass losses of TA(2)30 and TA40 after 90 days (**Figure II-4a**) there were minimal changes in the FTIR spectrum of ester-containing foams before and after degradation. The TA40 spectra showed a slight increase at 1405 cm^{-1}, which is attributed to the C-O-H bending peak from carboxylic acid that forms after hydrolysis of ester bonds. The urea peak of TA40 showed a slight decrease due to hydrolysis of adjacent ester bonds, which led to fragmentation of urea linkages in the foam structure. Based on SEM images, the porous morphologies of each foam composition were well maintained in hydrolytic solution until 72 days. After 90 days, pore collapse was observed in T30 and strut rippling was observed in T40TG20 (**Figure II-6).**

More significant differences were observed between the ester-containing foams and their controls over time in oxidative degradation conditions. Previously, our group analyzed degraded SMP foams and their degradation products and proposed an oxidative degradation mechanism for HPED and TEA; the tertiary amine oxidizes into amine-oxide, which further undergoes C-N fragmentation leading to the formation of carboxylic acids and aldehydes.[58] All TEA-based foams showed carbonyl peak shifts from 1689 cm^{-1} to 1696 cm^{-1} (**Figure II-5b**) which are attributed to the fragmentation of C-N bond from the tertiary amine of TEA or HPED to form carboxylic acid or aldehyde conjugates. G25 showed a minimal carbonyl peak shift due to the absence of tertiary amines in Gly, which further indicates the good oxidative stability of Gly-based foams. GA25 showed a larger carbonyl peak shift than G25 due to the formation of carboxylic acids and aldehydes from oxidation or hydrolysis of ester bonds in the oxidative solution. A gradual decrease in the urea peak was observed over time, which was more pronounced in ester-containing foams. Urea bonds in the ester-containing foams were formed when the amine end of trifunctional ester-containing monomer reacted with the isocyanate group of HDI. Thus, the gradual decrease in urea peaks over time is attributed to the groups' location relative to the labile ester linkages. Foam morphologies under oxidative degradation conditions were observed over time using SEM (**Figure II-7**). All of the control foams maintained their struts and did not undergo total material collapse until day 72. T30 and G25 retained their struts through all 90 days of the study, which supports the gravimetric analysis (i.e., these formulations had the slowest mass loss rate). Surface erosion was observed in TA40 on day 36, which was followed by

fragmentation, clustering, and total material collapse. All ester-containing foams showed completely collapsed structures on day 72, and none of them were retrievable on day 90.

In addition, qualitative analysis found that only the ester-containing foams showed bulk degradation under oxidative conditions (i.e., total structural collapse vs. gradual thinning of samples), while controls showed surface degradation throughout 90 days. H_2O_2 is known to produce reactive hydroxyl radicals, which acts as oxidants[60] to cause the chain scission of tertiary amines.[58] Due to the instability of the reactive hydroxyl radicals, oxidative degradation occurs primarily at the surface of polymer samples, which explains why the control foams showed surface degradation. For ester-containing foams, we hypothesize that the cleavage of tertiary amines on the surface enabled faster water diffusion into the foam to allow for hydrolysis of ester bonds in the inner structure, which resulted in bulk degradation of the foams.[61] This observation was consistent with SEM results (**Figure II-7**) where ester-containing foams showed fragmented struts clustered together (day 54 and 72), while controls had degraded membranes but more connected struts.

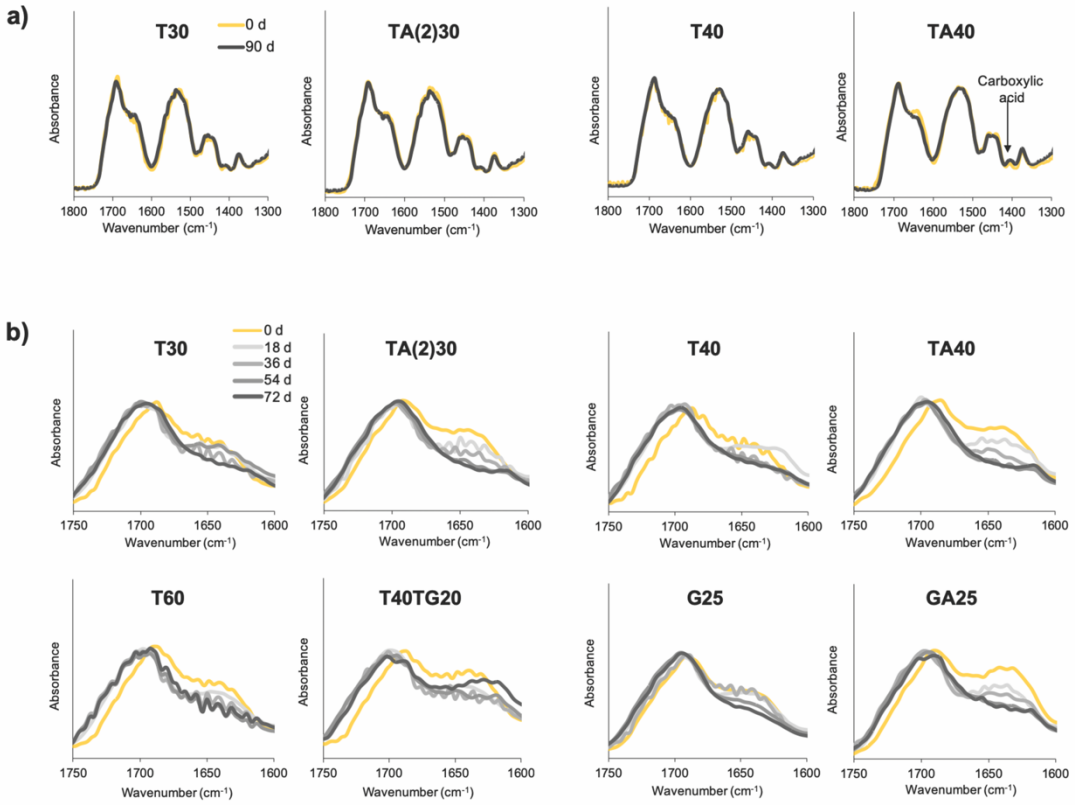

Figure II-5. FTIR spectra of different foam compositions under accelerated degradation conditions. a) 0 and 90 days after foams undergoing hydrolytic degradation (1N NaOH) at 37 ˚C. b) 0, 18, 36, and 72 days after foams under oxidative degradation condition (20% H_2O_2) at 37 ˚C. Analyses of 90 day samples were excluded since there was no retrievable foams left for TA(2)30, TA40, T40TG20 and GA25. (Representative legend is included in the first graph for each degradation condition.)

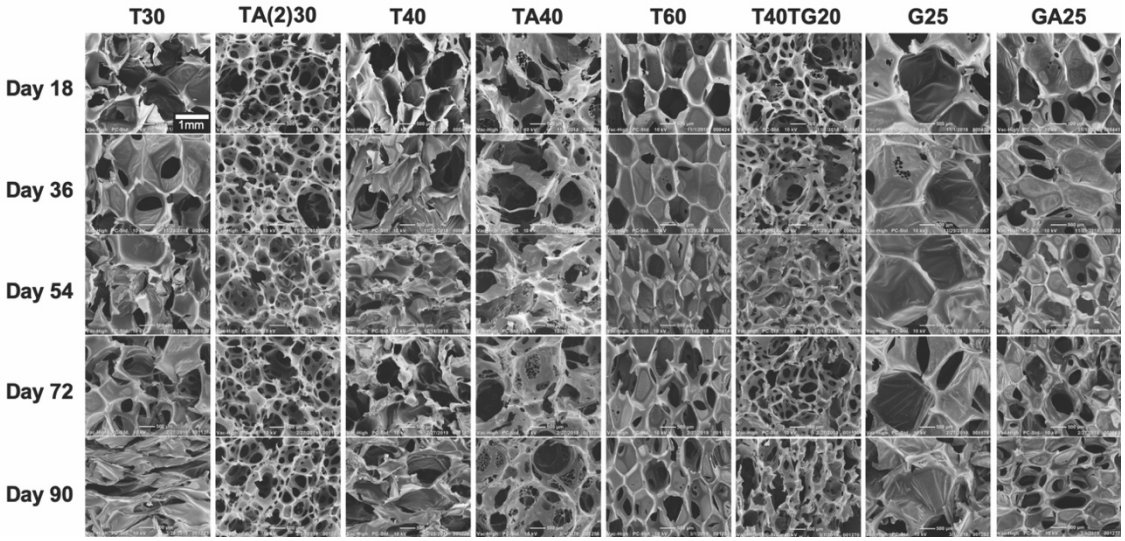

Figure II-6. SEM images of foams under accelerated hydrolytic degradation condition (1N NaOH at 37 ˚C) over 90 days. (Scale bar on T30 SEM image applies to all images.)

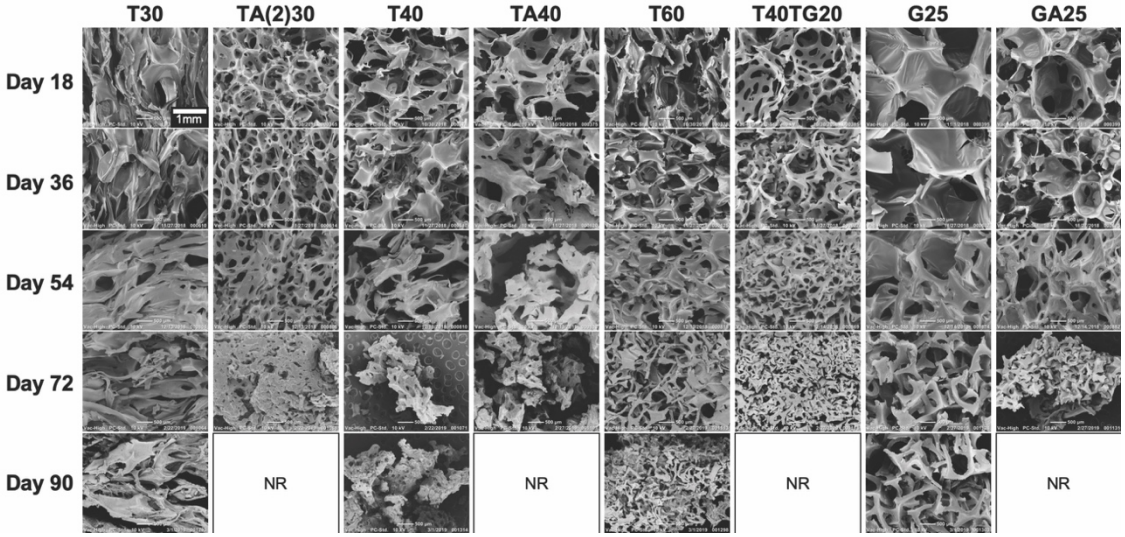

Figure II-7. SEM images of foams under accelerated oxidative degradation condition (20% H_2O_2 at 37 ˚C) over 90 days. NR: non-retrievable foams. (Scale bar on T30 SEM image applies to all images.)

Discussion

The low density of SMP foams ensures high porosity and high volume expansion, which is beneficial for blood clotting and cell infiltration in hemostatic applications.[27],[48] Although the ester-containing foams had higher densities than their controls, the densities of all foams synthesized in these studies are still relatively low (0.03–0.076 g/cm^3) compared to other polyurethane foams reported (0.1–0.2 g/cm^3),[62],[63] which could provide an advantage for their use as hemostats or tissue scaffolds.

TEA modified esters (TA(2), TA, and TG) were synthesized in powder form, and some monomer particles were not dissolved fully in the foaming mixture. This occurrence resulted in relatively lower gel fractions for TA(2)30, TA40, and T40TG20 foams compared to their controls. However, it is hypothesized that the monomer particles in the mixture aided in interconnected pore formation in the foam structure (**Figure II-2d**). Some undissolved particles may have acted as stress concentration points during foaming, generating holes in the pore membrane. Previously, Collins et al. demonstrated that increasing the amount of silica microparticles during foaming increased pore interconnectivity in polymer scaffolds.[64] Interconnectivity is a crucial property for a hemostat or for a tissue scaffold, since interconnected pores allow enhanced blood clotting, degradation rate, cellular growth, nutrient transport, and waste exchange.[64],[65] Formation of interconnected pores in TA(2)30, TA40, and T40TG20 foams also removes the need for a post-processing step of reticulation, which involves mechanically punching holes on the foam membranes with floating nitinol pin array.[31]

Therefore, the TEA-based ester-containing foams present a new method to reduce fabrication steps and potentially increase the efficacy of SMP foams for hemostatic use.

Hydrolytic and oxidative degradation profiles of SMP foams were analyzed *in vitro* in accelerated conditions. It is important to correlate the *in vitro* data to the *in vivo* time-frame. Weems et al. compared *in vitro* degradation data of porous SMP foams with *in vivo* data of foams implanted in porcine sidewall aneurysm.[58] These results showed that 45 ± 3 days in 3% H_2O_2 is comparable to 90 days *in vivo* and that 15 days in 20% H_2O_2 is equivalent to 108 days in 3% H_2O_2. This correlation allows an estimation for how quickly the foams synthesized in the current study would degrade *in vivo* in a porcine model. TA40 lost half of its mass by 42 days in 20% H_2O_2, which is equivalent to 1.7 years *in vivo,* while T40 had 50% mass loss at 75 days *in vitro,* which is 3.0 years *in vivo*. This result indicates that TA40 degrades approximately 1.8 times faster than T40 during the first half of foam degradation. For complete foam degradation, TA40 took 84 days *in vitro,* which is calculated to be 3.3 years *in vivo*, while T40's total *in vitro* mass loss correlates with approximately 4.3 years *in vivo.* Even though the converted *in vivo* degradation time-frame for TA40 is slower than the ideal scaffold degradation time for wound healing and skin tissue replacement,[66] degradation rate differs largely by animal model and implantation site. Therefore, this study can serve as a future resource for synthesis of multiple types of biodegradable SMP foams with varied degradation rates. In addition, Gly based foams were found to be more biostable than TEA based foams. Using the same correlations, G25 will take ~5.9 years to completely degrade *in vivo*, which is 1.4 times slower than T40 and 1.8 times slower than TA40. G25 has great

potential to be used in biomedical applications where increased material biostability is desired, such as in a stent or an aneurysm embolization application.[32],[67],[68]

Biocompatibility of degraded products is another critical factor to consider in developing long term implantable materials. The anticipated degradation products in concern are oxalic acid and glycolic acid, of which the oxalic acid has a lower safety threshold than glycolic acid.[69],[70] However, a previous study showed that the exposure level of oxalic acid for 10 cm^3 SMP foam is 32.0-36.6 mg total over the full degradation time frame, which is far below the toxic threshold for an average 70 kg human (37.8 mg/day).[58],[69],[70] While further analysis on degradation products of ester-containing foams needs to be performed, the new additives used in these foams were aminocaproic acid and glycine, a commonly used procoagulant drug and an amino acid, respectively, both of which are expected to be biocompatible.[71] In addition, cytotoxicity tests, animal studies with large hemorrhagic wounds, and mutagenicity tests on the degraded products and degraded ester-containing foams are necessary in future studies to enable clinical translation of these materials as effective and biocompatible hemostats.

Summary

Four types of biodegradable SMP foams were successfully synthesized using ester-containing trifunctional monomers: TA(2), TA, TG, and GA. All ester-containing foams showed uniformly porous structure and improved mechanical strengths compared to the controls. In addition, TA(2)30, TA40, and T40TG20 foams showed highly interconnected pores. Excellent thermal properties (dry T_g > 60 ˚C and wet T_g < 20 ˚C)

along with rapid and full volume expansion (< 8 min) in physiological conditions were observed in all foam compositions. TA40 and TA(2)30 showed faster degradation rate (43% and 15% mass loss respectively at day 90) compared to controls (9-10% mass loss at day 90) in hydrolytic solutions, with similar trends in oxidative solutions (100% mass loss by day 84 vs. 69-74% mass loss for control). Analyses on degraded foams demonstrated that ester-containing foams undergo faster surface erosion, clustering, and total material collapse than controls in oxidative conditions. These biodegradable SMP foams with clinically relevant thermal properties are promising smart materials for a hemostatic device that can be used on battlefields, and they also have a great potential for use as a drug delivering tissue scaffold.

CHAPTER III

SHAPE MEMORY POLYMER FOAM/GELATIN-NANOSILICATE HYDROGEL COMPOSITE WITH ENHANCED FLUID UPTAKE AND HEMOSTATIC PROPERTIES FOR USE AS A HEMOSTATIC MATERIAL

Introduction

Hydrogel coating on the SMP foam structure is desired due to the limited fluid absorption capacity of SMP foams. Previously, Landsman et al. had reported n-vinylpyrrolidone (NVP)-polyethylene glycol diacrylate (PEGDA) hydrogel-coated SMP foam composite.[26] The composite was doped with iodine to form povidone-iodine complex which showed antibacterial properties. The composite retained the shape memory properties of the SMP foam demonstrating 15 X volume expansion after submerged in 37 °C water. However, only 74% shape recovery was achieved after 15 min which is a very slow expansion rate to treat patients with severe hemorrhage in battlefield where hemostatic treatment should be completed within 30 min of their injuries.[53] There was no characterizations regarding the hemostatic properties of the composite device. Also, the NVP-PEGDA hydrogel does not have cell adhesive motifs, which are critical in tissue regeneration and reducing the healing time.

In this chapter, we are incorporating gelatin-nanosilicate hydrogel with the SMP foam. Gelatin, which is a denatured form of collagen, has abundant cell adhesive motifs (RGD), mimics extracellular matrix, absorbs body fluids, and contains positive and negative regions on its backbone.[72] In previous studies, nanosilicate-incorporated

gelatin hydrogels improved the hydrogel's physiological stability, and *in vitro/in vivo* hemostatic performance by enhancing protein adsorption and platelet adhesion.[73],[74] Nanosilicate ($Na^{+}_{0.7}[(Mg_{5.5}Li_{0.3}Si_8O_{20}(OH)_4)]^{-}_{0.7}$) is a disc-shaped synthetic silicate that has dual-charged surface which enables binding of numerous growth factors, therapeutic drugs, and peptides. This versatile binding capacity allows delivery of antimicrobials or growth factors to a wound site which can lessen inflammation and accelerate the healing process. In addition, nanosilicates have very low cytotoxicity (LD_{50}~4mg/mL), compared to other nanomaterials such as graphene (LD_{50}~100μg/mL), and they dissociate into nontoxic ions (Na^{+}, Mg^{2+}, $Si(OH)_4$, Li^{+}) in physiological conditions.[73],[74] Thus, gelatin hydrogels containing nanosilicates has great potential to serve as a biocompatible and effective hemostatic device.

Materials and Methods

SMP foam (H40) synthesis

SMP foams were synthesized using the three-step foaming process as described previously.[75] H40 foam composition was chosen due to its fast shape recovery rate compared to other SMP foam compositions.[26] First, an isocyanate (NCO) premix was made in a desiccated glove box by mixing 40 equivalents of hydroxyl groups from N,N,N′,N′-tetrakis(2-hydroxypropyl) ethylenediamine (HPED; Sigma Aldrich), 60 equivalents of hydroxyl groups from triethanolamine (TEA; 98% Alfa Aesar Inc.), and 100 equivalents of isocyanate groups from hexamethylene diisocyanate (HDI; TCI Chemicals). The NCO premix was thoroughly mixed and cured for two days in an oven

with a pre-set cure cycle (ramp rate 20 °C/h, held at 50°C for 36h). Secondly, a hydroxyl (OH) premix was prepared by mixing the balance hydroxyl groups from HPED, TEA, and deionized water using a FlackTek Speedmixer at 3400 rpm for 30 s. For the final step, NCO premix and OH premix were mixed together along with surfactants (DC 198, DC5943; 3400 rpm, 30 s; Evonik), catalysts (T-131, BL-22; 3400 rpm, 30 s; Evonik), and a physical blowing agent (Enovate; 3400 rpm, 5 s; Evonik). The mixture was allowed to foam at 50 °C for 3-6 min. The detailed amounts of components in the final foam are summarized in **Table III-1**.

Table III-1. H40 foam compositions

Sample ID	HDI (wt%)	HPED (wt%)	TEA (wt%)	Water (wt%)	DC198 (wt%)	DC5943 (wt%)	T-131 (wt%)	BL-22 (wt%)	Enovate (pph)
H40	62.8	13.1	13.4	2.7	4.0	3.0	0.03	0.6	5.0

Mechanical reticulation of SMP foam

All synthesized foams used in this study were mechanically reticulated following the previous reticulating procedure.[31] Reticulation was performed to ensure open-pore structure of the foams which would enhance gel penetration, blood clotting, cell migration, and wound healing process. In brief, synthesized foam was mounted on an oscillating vibratory shaker. A gravity-driven floating nitinol pin array (50 mm length) was loaded on top of the foam perpendicularly with the tips of unrestricted nitinol pins barely touching the top surface of the foam. The foam was agitated by the shaker while the floating pins moved downward penetrating the foam. The pin array moved 500 μm

horizontally to punch the foam. The foam was flipped and the same process was done on the other side of the foam.

Foam cleaning

Reticulated foams were sonicated in reverse osmosis (RO) water with 1:20 volume ratio for 30 min. RO water was switched to isopropyl alcohol (IPA), and samples underwent sonication four times changing the IPA to fresh solution every 30 min. Samples were sonicated further in RO water four times changing to fresh solution every 15 min. Cleaned foams without any residual foaming additives were dried in 50 °C oven overnight and stored at room temperature under vacuum until use.

Fabrication of foam/hydrogel composite (H40/Gel-NS)

Foams were punched into a cylindrical shape with 1 cm diameter and 1 cm length using a biopsy punch. Laponite XLG (BYK Additives) nanoparticles (6%) were weighed and added to deionized water. Gelatin (3%; Sigma Aldrich) was dissolved in deionized water at 37 °C. Under constant stirring, nanoparticle solution was added to a pre-heated gelatin solution at 60 °C and mixed until homogenous. Homogenous gelatin-laponite composite hydrogel was kept warm at 37°C. H40 foams were soaked in the composite for 5 mins to allow the infusion of hydrogel within the foam structure. To further facilitate infusion, the foam-hydrogel composite scaffold was placed in a vacuum chamber for 30 minutes. Then, the scaffolds were flash-frozen using liquid nitrogen and lyophilized overnight. Foams and foam-hydrogel composites were stored in a desiccated vacuum chamber until use.

Scanning electron microscopy-energy dispersive X-ray spectroscopy

Fabricated H40 foams, Gel-NS hydrogel, and foam-hydrogel composites were placed in microcentrifuge tubes and dipped in liquid nitrogen for 30 seconds. These flash- frozen samples were then sectioned transversally into two halves and were mounted on an adhesive carbon tape attached to a stainless steel stub. All samples were then sputter coated with Iridium in an inert atmosphere of Argon gas. Using scanning electron microscope, surface topography for each sample was observed at 70X magnification using a 20kV electron beam. Further, an energy dispersive X-ray spectroscopy was performed to conduct an elemental analysis of the samples to detect the presence of Mg and Si in the foam composites.

Swelling ratio

Dry weight (W_d) of H40 and H40/Gel-NS samples (n=3) were measured after taking them out from a desiccated vacuum chamber. They were submerged in 37 °C RO water for 24 h and weighed after removing excess water on the exterior of the samples to get the swollen weight (W_s). The swelling ratio (Q) was calculated using the equation below.

$$Q = \frac{W_s}{W_d}$$

Expansion study

The initial diameters of cylindrical foams and foam composites (n=3; 1 cm diameter, 1 cm length) were measured prior to crimping. The samples were placed inside

a heated ST 150-42 stent crimper (Machine Solutions, Flagstaff) at 70 °C for 5 min to allow the heat equilibration throughout the samples. Then the samples were radially crimped to a diameter of 2-2.5 mm and immediately cooled down to 25 °C to fix the secondary shape. The crimped samples were stored in a desiccated vacuum chamber at least for 24 h before use. After measuring the crimped diameters of the samples, they were immersed in 37 °C RO water or in 37 °C bovine plasma where the expanding diameters of each sample were measured (every 30 s up to 5 min, every 1 min over 5-10 min). All the diameters were measured using Image J by measuring the diameter at three evenly spaced locations along the sample length. Diameter recovery (%) was calculated by the following equation.

$$\text{Diameter recovery (\%)} = \left(\frac{Recovered\ diameter}{Initial\ diameter}\right) \times 100$$

Expansion force measurement

For radial expansion force measurement, the cylindrical foams and the foam composites were radially crimped before testing using the stent crimper as described above (n=3; 1 cm diameter, 1 cm length). For longitudinal expansion force measurement, cylindrical samples were placed longitudinally between two Teflon-coated stainless steel plates (Carver hot press) at 70 °C for 5 min. After heating the samples evenly, the samples were crimped to a thickness of 1 mm disc at 70 °C using a 1 mm metal rod spacer. Then, the samples were cooled to room temperature and stored in a desiccated vacuum chamber for 24 h before use. For both expansion force testing, a

crimped sample was placed between two compression platens inside a waterproof environmental chamber which was attached to the Instron Model 5966 Dual Column Test System (Illinois Tool Works Inc., Norwood, MA). After the sample was given a preload of 0.15 N, 40 °C RO water was filled into the water chamber up to the height which can submerge both platens and the sample. The expansion forces of the crimped samples were measured within the temperature range of 36.5-40 °C and the two compression platens remained still throughout the test. This analysis method is based on ISO 25539-2. The buoyancy force of water was measured by performing the same test without the sample between the platens. The expansion force was calculated by subtracting the buoyancy force from the raw force recorded.

Degradation study

Oxidative degradation

The initial weights of cylindrical foam samples (n=3; 1 cm diameter, 1 cm length) were measured. Samples were submerged in 20% hydrogen peroxide (H_2O_2) solution at a 1:20 volume ratio (foam:H_2O_2 solution) in individual glass vials. The samples were stored in 37 °C incubator and the solutions were exchanged to fresh ones every three days to keep constant pH and ion concentration. The sample weights were measured every six days after draining the sample solution, washing with RO water and IPA, and drying overnight under vacuum at 50 °C. For degraded foam analysis, attenuated total reflectance-Fourier transform infrared (ATR-FTIR) spectroscopy and

SEM imaging were used to characterize foam chemistry and foam morphologies every 18 days.

Hydrolytic degradation

The hydrolytic degradation process is the same with the oxidative degradation except for using 0.1N NaOH in place of 20% H_2O_2.

Hemostatic property analysis

Fresh bovine blood containing CPDA-1 (Citrate-phosphate-dextrose solution with adenine) anticoagulant was used to evaluate the clotting kinetics of foam and foam composites. The hemostatic ability of our foam-hydrogel composites was tested in both static and dynamic conditions. For static conditions, foam-hydrogel composite scaffolds were placed in a well plate, and bovine blood, pre-warmed to 37°C, was added to each well. 0.1M calcium chloride was added to inactivate the anti-coagulant . At every one-minute interval, blood was removed from the well, and the foam-hydrogel composites were washed with 1X PBS. The samples were then imaged using a stereo-microscope to visualize clot formed at each one-minute interval. Thus, clotting time for foam-hydrogel composite scaffolds was established. TCPS, H40 foams, and Gel-NS hydrogels were used as controls.

For the dynamic phase model, the Hemochron 801 Coagulation Analyzer was used. The ACT test function of the coagulation analyzer was utilized which allows the detection of a clot in a dynamic system. Samples and the bovine blood were added to the ACT tubes and allowed to rotate until a fibrin clot was detected by the analyzer. Clotting

time was measured in seconds, providing accurate results. H40 foams and Gel-NS hydrogels were used as controls, and the blank tubes were used as negative controls.

E-beam sterilization

Samples used in *in vitro* studies were sterilized with E-beam radiation at the National Center for Electron Beam Research (College Station, TX). Samples and humidity indicators (S-8028 10–60% Humidity Indicator, Uline, Pleasant Prairie, WI) were packaged in foil header pouches (Tyvek Foil Pouches, Beacon Converters, Saddle Brook, NJ) using an AVN packaging system (AmeriVacS, San Diego, CA). Nitrogen gas was purged into the pouch right before it was vacuum sealed with heat. E-beam dose of 43.8 kGy was radiated using a vertically mounted 10 MeV, 18 kW commercial scale linear accelerator. Alanine films (Kodak, Rochester, NY) were placed below samples to measure the actual absorbed radiation dose using a Bruker E-scan spectrometer (Bruker, Billerica, MA).

Attenuated total reflectance-Fourier transform infrared (ATR-FTIR) spectroscopy

E-beam sterilized samples were chemically characterized using ATR-FTIR and compared to the non-sterilized samples. Bruker ALPHA Infrared Spectrometer (Bruker, Billerica, MA) was used with a diamond ATR crystal. Bruker OPUS Spectroscopy software (Bruker, Billerica, MA) was used to analyze the obtained data.

In vitro study

A transwell assay was performed to determine the effect of leachables released from E-beam irradiated foam composite scaffolds on cell viability. Human mesenchymal stem cells (HMSCs) were cultured in a well plate in AMEM supplemented with FBS at 37°C under 5% CO_2. Upon reaching 75% confluency, a transwell containing an irradiated foam-hydrogel composite was introduced in the well. AMEM supplemented with FBS was added to the well to submerge the scaffold completely, and the well plate was maintained at 37°C for five days. Media was changed on day 1 and 3. Alamar Blue assay was performed on days 1, 3, and 5 to determine the toxicity of the leachables from the scaffolds at each time point. Viability was normalized to TCPS positive control each day.

Results

Surface morphology and elemental analysis

In applications of regenerative medicine, porous scaffolds play a major role in allowing cell infiltration and fluid retention. Under SEM, Gel-NS hydrogel shows a microporous structure. Although gelatin forms a brittle and flaky structure after flash freezing, combining with silicate provides a reinforcement to the microarchitecture of gelatin.[76] Thus, this enables the composite hydrogel to have better structural integrity. Fabricated H40/Gel-NS composites showed a clear integration of Gel-NS hydrogel in the porous structure of H40 foams. Our hypothesis for use of these foams in hemostasis depends on providing larger surface area to volume ratio to ensure increased fluid uptake

and expansion so as to allow plugging of blood loss and initiation of clotting. It is seen in the SEM image that the Gel-NS hydrogel has completely filled the pores in H40, thus providing an interconnected microporous network architecture to the foam composites (**Figure III-1 b-d**). This increases the surface area of the foam composites allowing for enhanced fluid retention which is desired for hemostasis.

The elemental analysis of foam composites shows significant signals of magnesium (Mg) and silicon (Si) which are predominantly present in the chemical structure of NS, which in contrast in absent in untreated H40 foams (**Figure III-1 e,f**). This shows that these ions are not pre-existent in the H40 structure but only introduced after treating with Gel-NS hydrogel. This also provides evidence of retention of nanosilicates within the porous structure of H40 foams, without any significant loss. Their confirmed presence ensures that they will play a significant role in the proposed application of hemostasis for these foam composites.

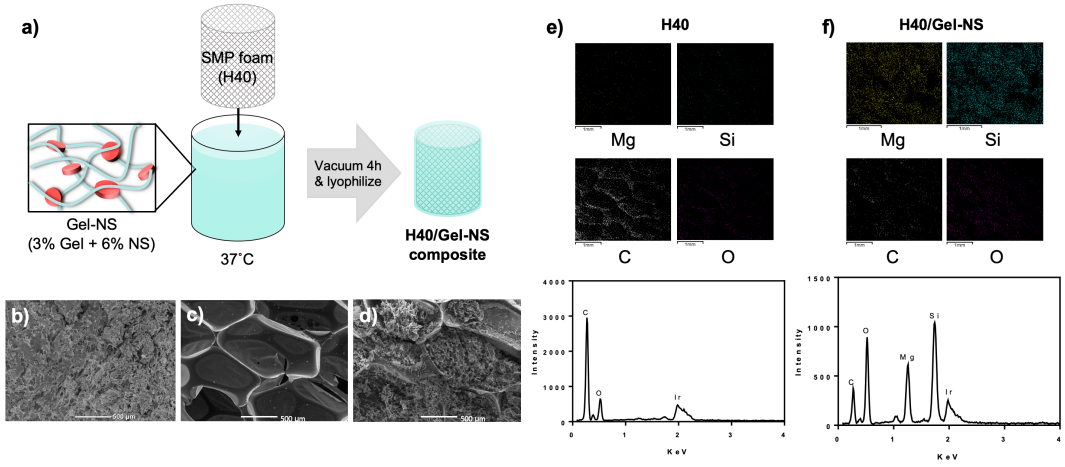

Figure III-1. Morphological analysis. a) Schematic of the fabrication of H40/Gel-NS composite. SEM images of b) Gel-NS hydrogel, c) H40 foam, and d) foam-hydrogel composite. Elemental analysis of e) H40 foam and f) the composite.

Fluid uptake and shape recovery

The swelling ratio of H40 and H40/Gel-NS in 37 °C water was measured to compare the fluid uptake capacity of the samples in physiological condition (**Figure III-2a**). H40/Gel-NS showed 11.1 X higher swelling ratio compared to H40. This demonstrated the incorporation of Gel-NS hydrogel enhanced the swelling capacity to be used as a hemostatic device for absorbing blood or wound exudate and keeping the wound moist throughout the healing process. Shape recovery of samples were analyzed by placing the radially crimped cylindrical samples in either RO water or bovine blood plasma at 37 °C and observing the expansion profile of their diameters (**Figure III-2b,c**). The crimped H40/Gel-NS recovered its full diameter 1.5 X faster than the crimped H40 both in water and in blood plasma. H40 and H40/Gel-NS both showed slower shape recovery in blood plasma than in water. However, the shape recovery time for H40/Gel-NS in blood plasma was still notably faster (< 4.5 min for 100% recovery) than that of previously developed iodine doped hydrogel coated foam (> 15 min to recover 80% of its shape in 37 °C water).[26] The results indicate that H40/Gel-NS would be appropriate for treating non-compressible wounds within the golden time of 30 min.[53]

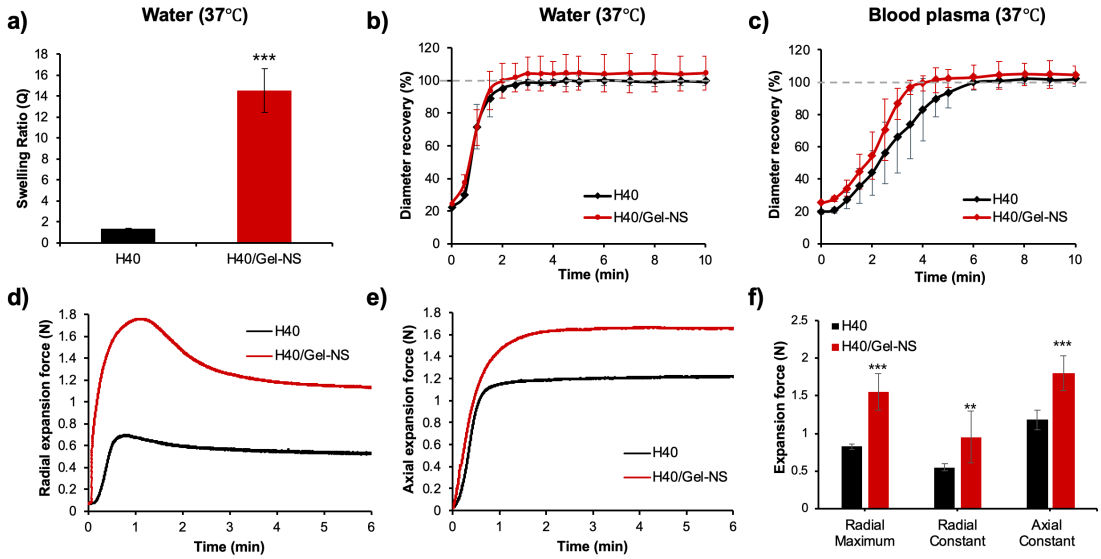

Figure III-2. Shape recovery and expansion properties. a) Swelling ratio of H40 and H40/Gel-NS in 37 °C water. Expansion profile of the foam and the composite in b) 37 °C water and c) 37 °C blood plasma. d) A representative graph of the expansion force of the radially crimped foam and the composite. e) A representative graph of the expansion force of the axially crimped foam and the composite. f) A bar graph of the expansion forces (n=3).

Expansion force

The treatment of non-compressible hemorrhage using injectable hemostatic devices requires applying adequate pressure to the bleeding site. The pressure has to be large enough to stop bleeding and to stay in the injected wound bed with or without an additional aid such as gauze. However, the pressure should not be too large to damage the surrounding tissue. The radial expansion force of crimped devices was measured following the ISO 25539-2 with the results shown in **Figure III-2d**. The longitudinal expansion force was measured using cylindrical samples (1 cm diameter, 1 cm thickness) crimped to a 1 mm thickness (**Figure III-2e**). The expansion of the samples was initiated with the introduction of 40 °C water in both measurements. For the radial

expansion force profile, the expansion force increased sharply immediately after the samples contacted water which reached a maximum peak within 2 min and slightly decreased to have constant force. The time at which the constant force was reached was consistent to the time point when the crimped samples expanded to their largest diameters in RO water (**Figure III-2b**). This indicates that after the crimped samples exerted force to recover their diameters, they became malleable that the expansion force decreased due to the full plasticization of the samples. For the longitudinal expansion force profile, the constant force was reached within 2 min as well showing similar expansion rate to the radial expansion.

The average radial maximum force of H40/Gel-NS was 1.6 N which was 2.0 X higher than H40 (**Figure III-2f**). The average force of H40/Gel-NS after the force became constant was 1.0 N which was still 1.8 X higher than H40. The average longitudinal constant force was 1.8 N for H40/Gel-NS which was 1.5 X higher than H40. With the assumption that both H40 and H40/Gel-NS have the same contact area with the compression platens, H40/Gel-NS exerted pressure of 4.8 - 8.0 kPa in radial expansion and 22.9 kPa in longitudinal expansion.

Degradation study

Gravimetric analysis was performed to characterize the degradation profiles of SMP foam and the composite in an accelerated oxidative degradation condition (**Figure III-3a**) and in an accelerated hydrolytic degradation condition (**Figure III-3b**). H40 contains amino-alcohols (HPED and TEA) which are previously shown to degrade into

lower amines, aldehydes and carboxylic acid in an oxidative condition due to the cleavage of C-N bond of tertiary amine.[58],[77] In the oxidative condition, H40 showed steady mass loss until day 54, and then noticeably faster mass loss was observed. This result is consistent to the previous study and this is because membrane degradation and strut thinning occurs initially before day 54 and strut fragmentation occurs after that which triggers large mass loss from the foam.[77] For H40/Gel-NS, it showed about 20% mass loss at the first measuring point (day 6) which is due to the diffusion of Gel-NS hydrogel since the physically crosslinked and hydrophilic gelatin polymer diffuses out easily in 37 °C solution. It should be noted that H40/Gel-NS shows the faster mass drop at earlier time point than H40. The mass drop of H40/Gel-NS was observed starting at day 36 which was 18 days faster than H40. This is attributed to the highly hydrophilic properties of Gel-NS hydrogel which allows effective H_2O_2 solution penetration into the inner pores of the foam. Therefore, oxidative degradation could progress more rapidly in H40/Gel-NS than H40.

In hydrolytic degradation condition, H40 foam did not show significant mass loss during 90 days. For H40/Gel-NS composite, similar mass loss of about 20% was observed at the initial measuring point and the mass afterwards was steady which indicates that most of Gel-NS hydrogel was diffused out of the foam before the first measuring point.

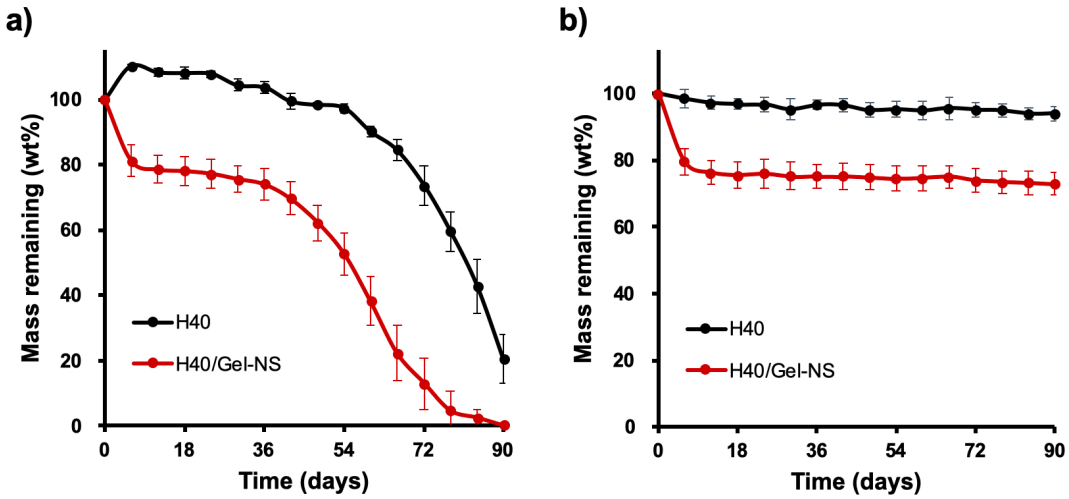

Figure III-3. *In vitro* degradation studies in a) an accelerated oxidative degradation condition (20% H_2O_2, 37 °C) and b) an accelerated hydrolytic degradation condition (0.1N NaOH, 37 °C) over 90 days.

Hemostatic property

We demonstrated the potential of H40/Gel-NS fabricated foam composites for faster blood clotting using a static and a dynamic model. In the static model, significant blood clotting was observed from the three minute interval in foam composite samples whereas TCPS control did not show any clotting until the seventh minute mark (**Figure III-4a**). Gel-NS hydrogel and H40 foam samples initiated clotting at the 4th and 6th minute interval, respectively. These results are consistent with our earlier studies, where integration of nanosilicates into the system greatly enhanced the hemostatic potential of the system.[(73),(74)] The increased fluid uptake property of H40 foams further facilitates the contact-based hemostasis driven by nanosilicates.

The kaolin activated clotting test was performed using Hemochron™ 108 series as our dynamic model for blood clotting (**Figure III-4b**). The principle of the test helped

identify the time of clotting initiation more narrowly. The results of the dynamic model showed an average value of ~200 seconds of clotting initiation time for foam composites while the untreated controls showed ~430 seconds. This validated the clotting time trend observed in the static phase which shows that combining H40 foam with gel-NS hydrogels accelerated hemostasis *in vitro*.

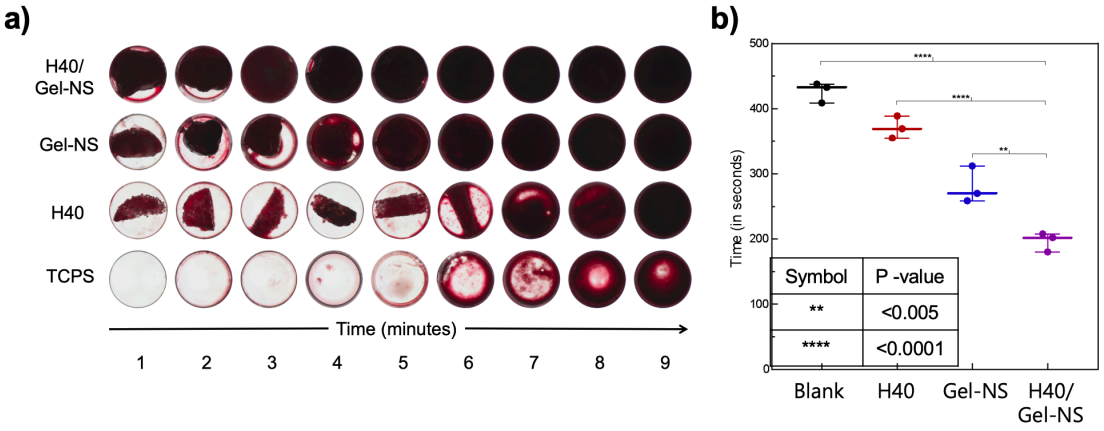

Figure III-4. Hemostatic property analysis. a) A qualitative analysis showing clotting kinetics of bovine whole blood with respect to time and sample types. b) A quantitative analysis of blood coagulation initiation time using a dynamic model, Hemochron™.

Biocompatibility

Gel-NS has been extensively studied for the growth of HMSCs *in vitro*.[78]–[81] H40 foam have been shown to be biocompatible in previous studies.[32],[37] Given the established biocompatible nature of both components, we hypothesized that combining H40 and Gel-NS in a composite foam would also result in a biocompatible scaffold. The use of transwells allowed for indirect contact between the foam composites and cells. We observed weight loss from the composite foams as seen in earlier experiments, with

accumulation of analytes in media. We speculate Mg^{2+} and Si ions from the scaffold surface could be introduced into the medium supplementing HMSC growth. In spite of leaching of analytes, HMSCs showed >90% viability when normalized to untreated TCPS controls for each day (**Figure III-5**). There was no statistical significance between the viability on day 1, 3 and 5 thus demonstrating that the leachables generated post-incubation of composite foams did not affect the survival of cells.

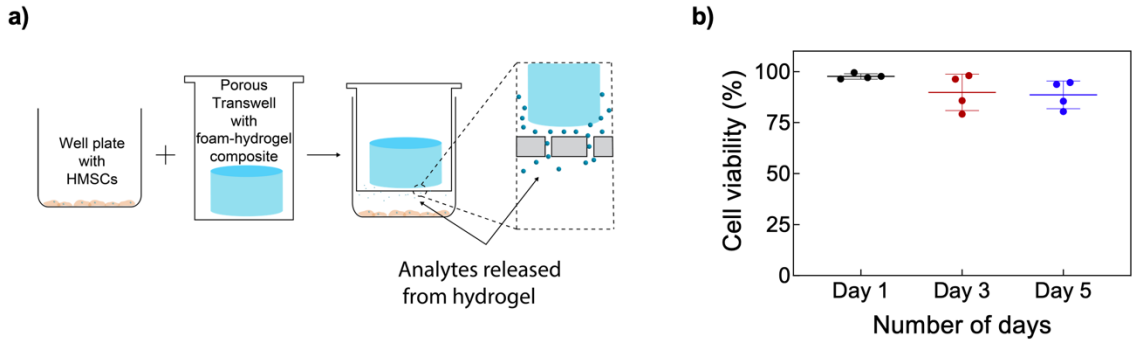

Figure III-5. *In vitro* biocompatibility test. a) A schematic of the transwell assay analyzing the toxicity of analytes released from the composite. b) Cell viability test using Alamar Blue assay over 5 days.

Characterization after E-beam sterilization

Chemical property analysis

Chemical compositions of SMP foam and the composite were analyzed before and after the E-beam sterilization at the radiation dose of 43.8 kGy using ATR-FTIR (**Figure III-6a**). The IR spectra showed that there is no difference between before and after the sterilization on either H40 or H40/Gel-NS. This suggests that E-beam sterilization does not alter any chemical structures of the foam or the composite.

Expansion property analysis

Shape recovery properties of crimped devices with and without E-beam sterilization were analyzed in 37 °C water (**Figure III-6b**). There was not any significant difference in expansion profile between samples treated with or without E-beam sterilization. All of the crimped devices expanded to their full diameters within three minutes. This indicates that E-beam sterilization does not affect the shape recovery properties of the foam or the composite.

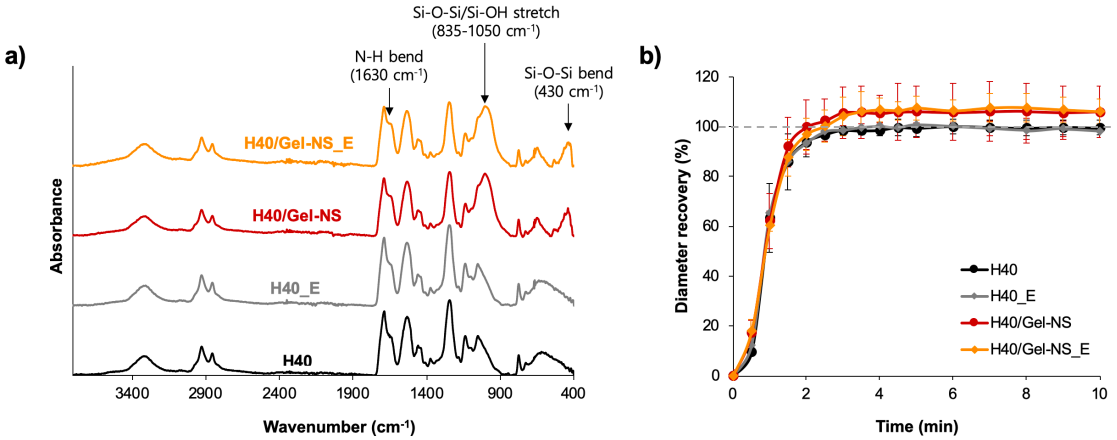

Figure III-6. Characterizations of H40 and H40/Gel-NS after E-beam sterilization. a) ATR-IR spectra before and after E-beam sterilization at 43.8 kGy. b) Expansion profile of the foam and the composite in 37 °C water before and after the E-beam treatment.

Discussion

The composite device showed faster expansion rate than the control foam both in water and in blood plasma. This is attributed to the stronger interaction between gelatin backbone containing hydrophilic groups (-COOH and -NH_2) and water molecules compared to the interaction between polyurethane foam and water. Water molecules

bound to the hydrophilic groups can open up the transport channel for water to move towards the center of the crimped samples,[82] which plasticizes shape memory polyurethane polymer and speeds up the shape recovery. The reason for slower expansion rate in blood plasma compared to that in water is due to the high viscosity of blood plasma containing various proteins and macromolecular components,[83] which lowers the accessibility of the water molecules to the center of the crimped samples. However, overall, the expansion rate of the composite was very fast, expanding to its full volume within two minutes in water and four minutes in blood plasma which ensures its ability to treat patients rapidly within 30 minutes. This is a great improvement in the expansion rate compared to the foam-hydrogel composite developed by Landsman et al. The expansion rate of their device was decreased significantly after coating the foam with PEGDA-NVP hydrogel, only achieving 74% shape recovery after 15 min of submersion in 37 °C water. Several factors in our study could have attributed to faster expansion rate compared to the previous work. The swelling rate of hydrogels generally increases with decreasing crosslinking densities since less water molecules will diffuse into highly crosslinked network.[84],[85] Physically crosslinked Gel/NS hydrogels will have a relatively lower crosslinking density and more flexible structure that will more likely to rearrange under shear stress compared to chemically crosslinked PEGDA-NVP hydrogels. Thus water molecules will diffuse into Gel/NS hydrogel more easily than PEGDA, resulting in higher swelling rate and faster expansion rate of H40-Gel/NS composite. In addition, PEGDA-NVP composite was crimped to a diameter of 1.5 mm while our composite was crimped to a diameter of 2 mm. A larger crimped diameter

would increase the expansion rate since water molecules can penetrate more easily into less tightly crimped polymer structure.

Radial expansion force and longitudinal expansion force of the crimped devices were measured using parallel plate method. The obtained radial expansion pressure of the composite (5 - 8 kPa) was at the lower end of gauze pressure range (6 – 26 kPa) measured by Dubik group using a wound model made of Perma-Gel Ballistic Gel.[10] The longitudinal expansion pressure of the composite (~23 kPa) was at the higher end of gauze pressure and also slightly higher than the Xstat pressure (16 - 21 kPa).[10] However, there were some limitations in the expansion force measurement method. One of the assumptions was that the crimped device is tightly fit to the wound cavity which would not be the case when injecting the device into an actual wound. This would make the actual expansion pressure of the composite smaller than the obtained pressure values. In addition, for the radial expansion force measurement, parallel plate method only measures one directional force against the parallel plates. Kim et al. had shown that the radial force of coronary stents measured by parallel plate method was 7-11% of the radial force measured circumferentially by Blockwise.[86] This indicates that the actual radial force of the composite device will be close to 9 - 22N. This is 25 – 65% radial force of commercially available coronary stents. In addition, the expected expansion pressure of the composite device assuming it is tightly fit to the wound will be 140 – 350 kPa which is much below the minimum aneurysm wall breaking stresses of 700 kPa.[87] This indicates the expansion of the composite device will not likely damage tissue. In addition, the radial or longitudinal expansion pressure of the composite is comparable to

commercial hemostats such as gauze or Xstat which demonstrates the composite device's hemostatic ability.

Degradation studies demonstrated that the composite device has similar hydrolytic degradation profile after the initial diffusion of Gel-NS hydrogel but has faster oxidative degradation rate compared to the SMP foam. The significant mass drop in the oxidative degradation study, which is caused by the breakage of H40 foam struts, was observed 18 days earlier in the composite than in the foam. 18 days in an accelerated oxidative degradation in vitro can be correlated to ~260 days in vivo in a porcine model according to the calculation from the previous study that compared the in vitro degradation data of SMP foams to the in vivo degradation data of implanted SMP foam in a porcine sidewall aneurysm.[58] This indicates that the composite device can be estimated to degrade within 3.6 years in vivo which is comparable to the degradation rate of previously developed biodegradable SMP foams made with ester containing monomers.[77] This result is noteworthy in that the SMP foam's degradation rate can be accelerated not only by chemically modifying the foam structure but also by physically coating the SMP foam with a highly hydrophilic hydrogel like Gel-NS. For future work, the chemical and physical methods can be combined to attain a hemostatic device that has faster degradation rate and thus matches more with the actual wound healing time-frame.

Summary

SMP foam/gelatin-nanosilicate hydrogel composite was synthesized which possesses the unique shape memory properties from SMP foam and high fluid absorption capacity from the gelatin-nanosilicate hydrogel. The synthesized foam-hydrogel composite showed 11 times higher swelling ratio and faster expansion rate in physiological condition compared to the control SMP foam. Mechanical testing demonstrated that the composite has higher expansion force than the foam both when the samples were radially and longitudinally crimped. Hemostatic studies showed that the composite could clot blood at around three min which was two times faster than the control SMP foam. *In vitro* studies demonstrated that over 90% of HMSC viability was achieved in a transwell assay on the composite. Overall, the incorporation of gelatin-nanosilicate hydrogel to SMP foam improved the fluid uptake capacity, expansion rate, expansion force, hemostatic properties, and degradation rate which proves the material's potential to be used for hemostatic medical devices.

CHAPTER IV

ENHANCED X-RAY VISIBILITY OF SHAPE MEMORY POLYMER FOAM USING IODINE MOTIFS AND TANTALUM MICROPARTICLES*

Introduction

X-ray visibility is required in delivering embolization devices to a targeted aneurysm site using an endovascular approach. Kashyap et al. three-dimensionally (3D) printed and salt leached thermoplastic SMP containing tungsten particulates to fabricate radiopaque and porous endovascular embolization material.(88) However, the fabricated SMP had too high density (~1 g/cm^3) and too stiff modulus (~1 GPa) to be used as a neurovascular device. In the case of low-density SMP foams, Hasan et al. physically incorporated tungsten nanoparticles into SMP foams to increase the X-ray visibility. Sufficient radiopacity was achieved at 6 vol% tungsten foams, but the mechanical toughness was diminished significantly.(89) Nash et al. reported chemically modified, triiodobenzene monomer (5-amino-2,4,6-triiodoisophthalic acid; ATIPA) containing SMP foams with increased X-ray visibility and mechanical toughness. However, the degree of radiopacity was still not sufficient for the neurovascular device scale (2 mm diameter),(90) motivating the need for further opacification.

---

* Reprinted with permission from "Enhanced X-ray Visibility of Shape Memory Polymer Foam Using Iodine Motifs and Tantalum Microparticles" by L. Jang, L. Nash, G. Fletcher, T. Cheung. A. Soewito, and D. Maitland, 2021. *J. Compos. Sci.* **5**(1), 14, Copyright [2021] by MDPI.

Tantalum is a good candidate material as an X-ray visible additive to SMP foams due to its excellent biocompatibility, ductility, corrosion resistance, and radiopacity.[91],[92] Tantalum has been in clinical use since 1940 and has shown great *in vivo* bioactivity, exhibiting abundant cellular adherence, growth, and extracellular matrix formation on tantalum coated surface.[91],[93] In this chapter, tantalum microparticles were loaded on the ATIPA foaming mixtures to further enhance X-ray visibility of the ATIPA SMP foam which was previously developed by Nash et al.[90] In addition, cell opening additives were added during the foaming process to make a more open cell structure, which will prevent the foam from shrinking during curing. Thermal properties, mechanical properties, chemical properties, and radiopacity were characterized. The effect of E-beam sterilization on chemical, thermal, and mechanical properties of tantalum loaded ATIPA foams (AT_T) was also analyzed, in addition to the *in vitro* degradation behavior (oxidative and hydrolytic) after E-beam sterilization.

Materials and Methods

Materials

5-amino-2,4,6-triiodoisophthalic acid (ATIPA; Sigma Aldrich, St. Louis, MO), 3-methyl-1,5-pentanediol (MPD; Sigma Aldrich), 1,2,6-hexanetriol (HT; Sigma Aldrich), 2-butyl-2-ethyl propanediol (BEP; VWR Scientific, Radnor, PA), hemxamethylene diisocyanate (HDI; TCI America, Portland, OR), Enovate 245fa Blowing Agent (Honeywell International, Houston, TX), tantalum powder (APS~2 μm, 99.9%; Alfa Aesar, Tewksbury, MA), Tegostab B8523 (Evonik, Essen, Germany), 2-

propanol 99% (IPA; VWR Scientific), tetrahydrofuran (THF; Millipore Billerica, MA), Dulbecco's Modified Eagle Medium (DMEM; Sigma Aldrich), and deionized (DI) water (>17 MΩcm purity; Millipore water purifier system; Millipore) were used as received.

Synthesis of tantalum loaded ATIPA SMP foam

ATIPA SMP foams with tantalum microparticles (AT_T) were synthesized based on the protocol described by Nash et al.[90] Hydroxyl (OH) premix was prepared one day before foaming by adding 0.6 equivalent of ATIPA, MPD, BEP, and HT. The OH premix was mixed for 30 s at 3500 rpm using a Flacktek high-speed shear mixer, heated at 50 °C for one hour, mixed for 30 s at 3500 rpm, heated overnight at 50 °C, and mixed for 30 s at 3500 rpm before foaming. Isocyanate (NCO) premix was prepared two days before foaming in a desiccated glove box by adding 0.4 equivalent of ATIPA, MPD, BEP, and HT. The NCO premix was mixed at 3500 rpm for 30 s, heated at 50 °C for an hour, mixed at 3500 rpm for 30 s, and heated at 50 °C overnight. On the next day, 1 equivalent of HDI was added to the NCO premix and it was mixed for 10 minutes at 3500 rpm and placed on a room temperature shaker overnight at 60 rpm. On the foaming day, the viscosity of NCO premix was checked to be like honey and if it was less viscous, it was shaken for an additional day. 0, 2, 4, and 8 vol% tantalum powder was added to the NCO premix and mixed for 30 s at 3500 rpm. The mixture of 4 wt% of surfactant DC1990 and 0.025 wt% of Tegostab B8523 was added to the NCO premix and mixed for 30 s at 3500 rpm. The OH premix was added to the NCO premix and mixed for 30 s. After adding 1.5 mL Enovate and mixing for 15 s, the mixture was cured

for 20 minutes at 90 °C. The foam skin was removed by a razor blade and then post-cured at 50 °C overnight. The detailed foam composition is shown in **Table IV-1**. All the foam samples were thoroughly cleaned with reverse osmosis (RO) water (30 minutes, sonicated), IPA (30 minutes x 4 times, sonicated) and RO water again (15 minutes x 4 times, sonicated). Foam samples were dried at 50 °C overnight and stored at room temperature under vacuum before use.

Table IV-1. ATIPA SMP foam compositions with varying amounts of tantalum.

Sample name	ATIPA (eq%)	MPD (eq%)	BEP (eq%)	HT (eq%)	HDI (eq%)	Tantalum (vol%)	Tegostab B8523 (wt%)	Enovate (mL)	Scale (g)
AT	20	40	20	20	100	0	0.025	1.5	8
AT_2%T	20	40	20	20	100	2	0.025	1.5	8
AT_4%T	20	40	20	20	100	4	0.025	1.5	8
AT_8%T	20	40	20	20	100	8	0.025	1.5	8

Physical and morphological characterization

Foam density was calculated by foam mass divided by foam's bulk volume. Foams were cut into 1 cm^3 cubes and the mass was measured (n=5).

Pore size was measured using images taken from scanning electron microscopy (SEM; JCM-5000 Neoscope, JEOL, Peabody, MA). For SEM sample preparation, foams were cut into 3 mm thick slices and sputter coated. Five images were taken for each foam composition. Random 5-6 pores were selected per image and their diameters were measured using ImageJ software (n=20).

Gel fraction was calculated by the final sample mass divided by the original sample mass. Foam samples were cut into 1 cm^3 cubes. The samples were cleaned three times with IPA (1:20 volume ratio) for 30 minutes each using sonication to remove any residual surfactants. Then the samples were dried at 100 °C overnight and the mass was recorded. THF (1:20 volume ratio) was added to the samples, heated at 50 °C for 48 hours, and dried at 70 °C after removing THF for 36 hours. The final mass of the samples was recorded (n=5).

ATR-FTIR spectroscopy

The absorbance of foam samples was measured using attenuated total reflectance Fourier transform infrared (ATR-FTIR) spectroscopy (Bruker ALPHA, diamond ATR crystal, Bruker, Billerica, MA). Bruker OPUS Spectroscopy software was used to analyze the spectra.

Differential scanning calorimetry (DSC)

Glass transition temperatures (T_g) of dry samples (dry T_g) and water-plasticized samples (wet T_g) were analyzed using differential scanning calorimetry (DSC Q200, TA Instruments, New Castle, DE). For the dry T_g measurement, dry foam samples (2 - 4 mg, n=3) were loaded into Tzero pans and two heating cycles were run of which the second cycle was used to get the dry T_g (heating range:-40∼120 °C, ramp rate: 10 °C/min, 1 min equilibration at each endpoint). For wet T_g measurement, the dry mass of the samples were measured (2 - 4 mg, n=3) and the samples were submerged in 50 °C water for 30

minutes. Excess water was squeezed out using a laboratory wipe until the water uptake was smaller than 10% of the original sample mass. Samples were loaded into Tzero pans and only one cycle was run to determine the wet T_g (heating range:-40~120 °C, ramp rate: 10 °C/min). Pyris software was used to determine the T_g's of the samples.

Dynamic mechanical analysis (DMA)

Foam samples were punched into cylinders of 6 mm diameter and 5 mm thickness. Thermomechanical properties of the foams were analyzed using a TA Q800 Dynamic Mechanical Analyzer (TA Instruments, New Castle, DE) with a compression mode. Foams were equilibrated at 20 °C for 5 min and heated to 100 °C at 3 °C/min rate with an amplitude of 40 μm at 1Hz and a preload of 0.01 N.

Expansion study

Foams were punched into cylindrical shapes with 2 mm diameter and 1.5 cm length (n=3). The samples were axially threaded over 0.006" wires. The foam crimper (Machine Solutions SC250) was pre-heated to 100 °C for 15 minutes. Foams were radially compressed at 100 °C, constrained while cooling to room temperature, and released from the crimper. Crimped foams were placed under vacuum for 24 hours before the expansion test. Foams over wires were submerged in 37 °C water and the expanding foams were imaged every one minute until five minutes, and every five minute until 40 minutes. Diameters of the expanding foams at five sites along the length were measured using ImageJ software.

Mechanical testing

Samples were prepared by cutting into dog bone shape ASTM D-638-V. Each shorter ends of the dog bone samples were epoxy glued to wooden blocks and they were rested for 24 hours for complete cure. The attached wooden blocks were fixed to clamps on MTS Insight 30 Universal Tensile Tester. Strain to failure experiments were performed on the foam samples (n=5) with a rate of 5 mm/min at room temperature.

X-ray spectroscopy

Samples were cut into 1.5 cm x 1.5 cm squares with thicknesses of 8, 4, 2, and 1 mm. Neurovascular scale foams which were expanded and crimped cylindrical samples with 2 mm diameter were prepared. All the foam samples were taped on a plastic tray as well as two bare platinum coils as positive controls (0.008" OD 90/10 Pt/Ir coil and 0.008" OD 92/8 Pt/W coil). X-ray images of the plastic tray containing all the samples were taken using OrthoScan C-arm system (Mobile DI Model 1000-0005). X-ray images were obtained with and without an 0.5" aluminum plate over the sample tray which was used as a skull analog that attenuates X-rays and imitates the clinical setting of endovascular treatment.[94] Gray scale values were measured on the background of an 8-bit X-ray image and on the samples using ImageJ software. The background value was subtracted from the sample's mean grey scale value.

Cytocompatibility test

Extraction media tests were performed on the ATIPA foams with a 3 cm^2/mL extraction ratio according to ISO10993-5. Cell culture media consisted of DMEM, 10%

newborn calf serum, 1% penicillin/streptomycin, and 0.1% fungizone. The extracts of each specimen were obtained by submerging 5 mm diameter and 2 mm thick discs cut by biopsy punch into 2 mL of media solution. The size of the discs was chosen through consideration of the pore sizes and volume to represent the accessible surface area. The samples were then placed on a shaking incubator for 72 h at 37 °C. Three replicate extraction media samples were made for each foam.

NIH/3T3 mouse fibroblast cells were seeded at an initial 7,500 cells per well onto 96-well polystyrene plates and cultured for 24 h at 37 °C and 5% CO_2 in an incubator before treatment with extract media samples. At 24 h, 200 µl of extraction media was used for each well. Cell viability was evaluated using a resazurin assay to quantify metabolic activity 48 h after the addition of extraction media. Resazurin solution was added to cell culture media for a 5% final concentration. Cells were then incubated in the media and resazurin solution for 3 h, where the increase in absorbance at 590 nm relative to a blank (media and 5% resazurin without cells) was measured using a plate reader (Tecan Infinite M200 Pro, Switzerland). The absorbance values for the extract media samples were compared to a negative control (media and 5% resazurin with cells and without extract media) as a percentage, with the negative control representing 100% cell viability.

E-beam sterilization

Samples were packaged in foil film bags (Beacon Converters, Saddle Brook, NJ) with humidity indicators. The packages were vacuum sealed with heat after purging with nitrogen gas using an AVN packaging system (AmeriVacS, San Diego, CA). The sealed

packages were E-beam sterilized at 43.6 kGy E-beam dose (10 MeV, 18kW) at the National Center for Electron Beam Research (College Station, TX). Alanine films (Kodak, Rochester, NY) were used to measure the actual dose of E-beam using a Bruker E-scan spectrometer (Bruker, Billerica, MA).

Degradation analysis

In vitro degradability of foam samples was analyzed in an accelerated oxidative condition (20% H2O2) and an accelerated hydrolytic condition (0.1 N NaOH). Samples were prepared by cutting foams into 1cm3 cubes (n=3) and the initial sample mass was recorded. Samples were submerged in 20% H2O2 or 0.1 N NaOH with a 1:20 volume ratio (foam:solution) and stored at 37 °C. Degradation solutions were exchanged with fresh solutions every three days to ensure stable pH or ion concentration. The mass change of the samples was recorded every six days. Samples were washed with RO water and ethanol (1:20 volume ratio) and dried at 50 °C under vacuum overnight. The mass of the samples were recorded and the samples were put into fresh degradation solutions. To analyze the chemical and morphological changes of the sample foams over degradation time, ATR-FTIR and SEM analysis were performed every 18 days of degradation.

Tantalum extraction analysis

The AT_2%T was chosen for the extractables study due to its optimal radiopacity and the oxidative stability. The extraction was performed under exaggerated extraction conditions. Foam samples were prepared in neurovascular device scale (2 mm

in diameter, 1 cm in length), and submerged in 5 mL of water (polar extraction) and hexane (non-polar extraction) at 50 °C for 72 hours.

To study the effect of the oxidative and hydrolytic degradation solutions on the extraction of tantalum particles from the foam samples, AT_2%T was submerged in 5 mL of 20% H_2O_2 and 0.1 N NaOH at 37 °C for 72 hours.

Foam samples were removed from the four extraction solutions. After gently mixing the solutions, 1 mL aliquot was taken and 0.1 mL of concentrated hydrofluoric acid (HF) was added for complete dissolution of tantalum. The aliquot equilibrated for a minimum of one hour in a polypropylene acid digestion tube. For the hexane extraction solution, hexane was evaporated using nitrogen evaporation. Then deionized water was added to the samples to a final volume of 10 mL. A method blank and lab control spike solutions were prepared and got the same treatment as the samples. The samples were analyzed by inductively coupled plasma-optical emission spectrometry (ICP-OES) to determine the amount of tantalum in the extraction solutions. The ICP-OES analysis including the HF treatment was performed at Legend Technical Services Inc. The total amount of tantalum extracted from the neurovascular device was calculated by multiplying the result by the volume of the remaining solutions accounting for the evaporated solvents in the extraction solutions.

Results

Physical properties of ATIPA-tantalum composite (AT_T) foams

Foam densities of AT_T foams were in the range of 0.045-0.2 g/cm^3 (**Figure IV-1a**). AT_T foams showed increasing foam densities as the tantalum content increased.

As more tantalum was added to the NCO premix, the foaming mixture became more viscous which led to the lower rising height of the foam and thus, higher density and smaller pore size (**Figure IV-1b**). The foaming mixture was especially viscous for AT_8%T after loading 8 vol% tantalum that its final foam height was significantly lower than the other foams, resulting in significantly higher density. A highly viscous foaming mixture could limit the release of gas that was generated inside the bulk foam solution and cause many small pores to form throughout the foam. Furthermore, microparticles serve as nucleation points in foam synthesis due to stress concentration and generate a higher number of pores inside the foam.[89] All of the AT_T foams showed high gel fractions over 90% (**Figure IV-1c**). AT foam showed the lowest gel fraction of 92% while AT_2%T, AT_4%T, and AT_8%T foams showed 96% gel fraction. This is attributed to lower density and lower number of nucleation points of AT foam compared to tantalum added foams.

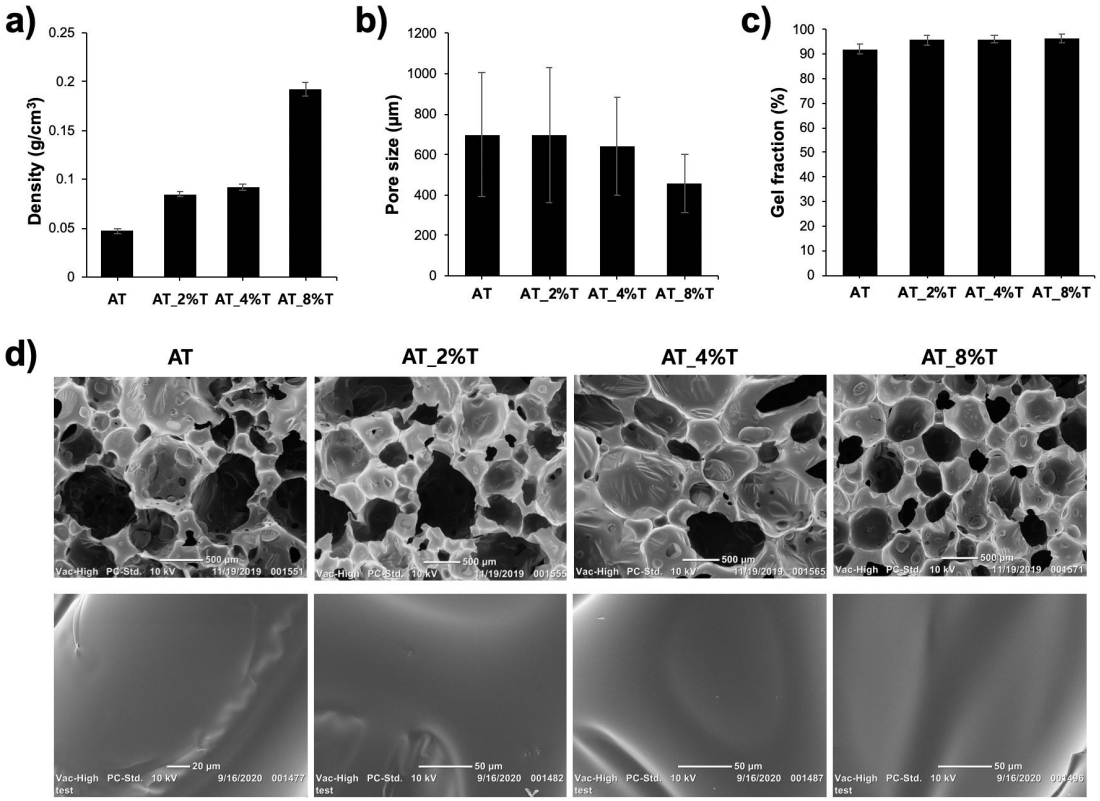

Figure IV-1. Physical and morphological properties of ATIPA foams. a) Foam densities measured after RO water and IPA cleaning step. b) Pore sizes measured from SEM images using Image J. c) Gel fraction measured after IPA and THF treatment. d) Representative SEM images of the foam morphologies at 30X magnification (top) and 500X magnification (bottom).

Morphological properties

SEM images in **Figure IV-1d** (top) show partially open porous structures of ATIPA foams. The addition of Tegostab B8523 which is a commercial cell opener for polyurethane foams introduced a higher number of open pores in the foam system compared to the previous ATIPA foam developed by Nash et al.[90] AT_T foams demonstrated pore sizes ranging from 300 to 1000 μm. AT_8%T showed more homogeneous pore sizes compared to other foams because of the increased nucleation

sites and higher density. All of the foams exhibited even distribution of tantalum particles as shown in the smooth surface of the foam membranes and did not show any noticeable agglomerates in the SEM images even at higher magnification (500X).

Chemical characterization

Chemical properties of AT_T foams were analyzed using ATR-FTIR spectroscopy. All of the foams showed identical peaks indicating that the addition of tantalum microparticles did not change any chemical properties of the control AT foam (**Figure IV-2a**). All foams showed a strong hydrogen bonded urethane C=O peak at 1686 cm^{-1}. This urethane peak was observed in previous polyurethane foams that were made using low molecular weight polyols which is also the case in this study.[27] A urea shoulder peak is present at 1650 cm^{-1} which is from the urea link formed when the amine group of ATIPA reacted with the isocyanate group of HDI. A broad peak at 3310 cm^{-1} indicates N-H stretching and peaks at 2849 cm^{-1} and 2896 cm^{-1} are from C-H stretching of methyl groups of MPD or BEP. Peaks at 1512 cm^{-1} and 1236 cm^{-1} are from amide II and amide III vibration peaks respectively from amide link formed when the carboxylic group of ATIPA reacted with the isocyanate group from HDI.

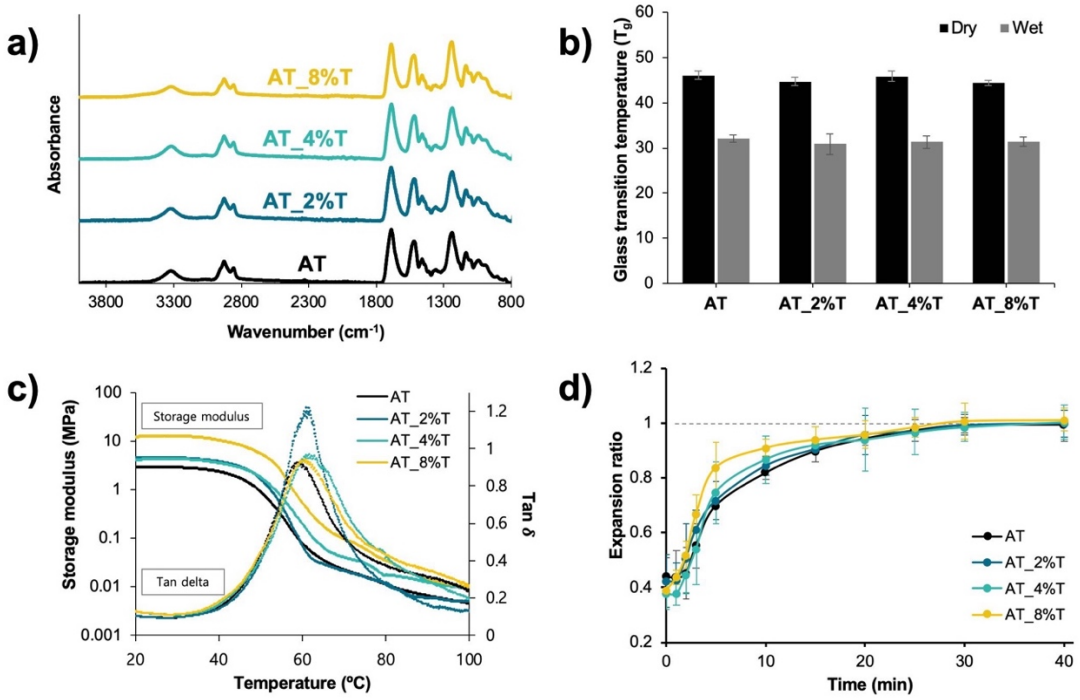

Figure IV-2. Chemical, thermal, and thermomechanical properties of ATIPA foams. a) ATR-IR spectra of synthesized foams. b) Dry and wet glass transition temperatures (T_g's) of each foam composition measured using DSC (n=3). c) Storage modulus and Tan δ measured as a function of temperature using DMA. d) Expansion profile of crimped foam cylinders (2 mm diameter, 1.5 cm length) in 37 °C water (n=3).

Thermal characterization

Dry T_g and wet T_g of AT_T foams were measured using DSC (**Figure IV-2b**). All of the dry T_g's of the foam samples were in the range of 44-47 °C and all of the wet T_g's were in the range of 30-33 °C. There was not any trend observed in between the T_g's of the foam samples which indicates that the addition of tantalum microparticles did not affect the thermal properties of the foams. Also, dry T_g being higher than 40 °C ensures the safe storage of the foam devices at dry state at ambient temperature, and wet

T_g being lower than 37 °C ensures their ability to expand passively in bloodstreams at body temperature.

Thermomechanical characterization

DMA was performed to analyze the mechanical properties of the foams as a function of temperature (**Figure IV-2c**). The T_g values of ATIPA foams measured by DMA (max tanδ) were all within the range of 59 – 62 °C which was comparable to the trend shown in DSC T_g values. Although the ATIPA foams had increasing storage modulus with the increasing tantalum content, their onsets of phase transition were all similar (46 - 49 °C) which indicates the addition of tantalum microparticles does not alter the heat transferring rate of the material.

Expansion study

Radially crimped cylindrical foams in the NED scale (2mm diameter) were submerged in 37 °C water to observe the expansion profile over time (**Figure IV-2d**). Foams were crimped to 0.64-0.77 mm in diameter and all of the foams showed full recovery within 30 minutes. Foams showed fast expansion, demonstrating 70%, 72%, 75%, and 84% recovery of original diameters at the 5 minute mark for AT, AT_2%T, AT_4%T, and AT_8%T, respectively. The expansion rate was faster with the increase of tantalum content in the foams. Since the DMA results showed that the addition of tantalum does not have a significant effect on the heat transferring rate of the material, the faster expansion at AT_8%T foam is attributed to its higher crosslink density in the

foam network due to the increased physical crosslinks. This result is consistent with previous work that showed SMP networks with higher crosslinking density recover faster to their original shapes than the SMPs with a less dense network when both materials have similar glass transition properties.[95]

Tensile testing

The mechanical properties of the samples were characterized using tensile testing (**Figure IV-3**). The AT foams with the addition of 2% and 4% tantalum microparticles did not show any significant difference in the overall mechanical properties compared to AT foam. However, AT_8%T showed significantly higher Young's modulus, ultimate tensile strength, and significantly lower toughness and strain at break compared to other foam compositions. This indicates that high loading of tantalum particles (8%) results in stiffer and less tough foam matrix which could be attributed to the smaller pore sizes leading to higher crosslink density and tantalum particles replacing a higher portion of each polymer strut cross section.

a)

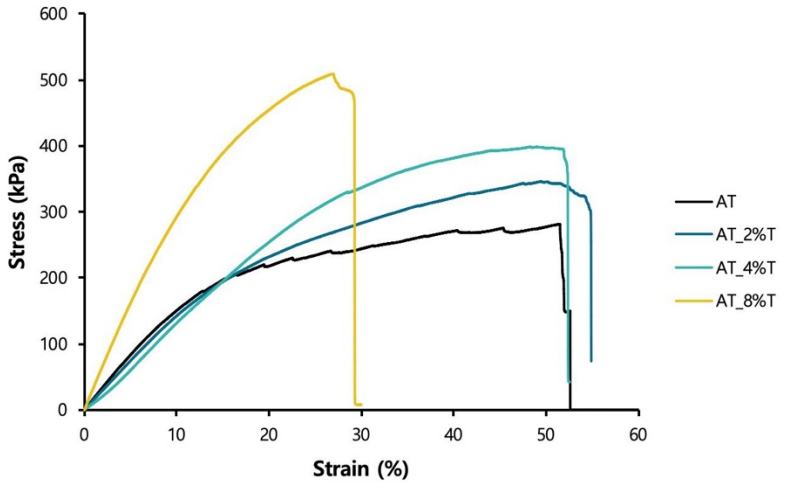

b)

	Ultimate tensile strength (kPa)	Toughness (kJ/m^3)	Strain at break (%)	Young's modulus (kPa)
AT	266 ± 54	110 ± 52	58 ± 17	1216 ± 287
AT_2%T	280 ± 86	147 ± 38	71 ± 17	1343 ± 571
AT_4%T	318 ± 78	151 ± 54	68 ± 16	1304 ± 226
AT_8%T	461 ± 38	84 ± 32	26 ± 9	3468 ± 801

Figure IV-3. Mechanical properties of ATIPA foams obtained from tensile testing. a) Representative stress-strain curve for each foam composition. b) Mechanical properties (ultimate tensile strength, toughness, strain at break, and Young's modulus) of ATIPA foams (n=5).

X-ray visibility analysis

Foam samples were prepared in thicknesses of 1, 2, 4, and 8 mm, as well as in neurovascular device prototypes (**Figure IV-4a**). X-ray images of the foams are shown in **Figure IV-4b**,**c** where a 0.5" aluminum plate is placed over samples in **Figure IV-4c** as a human skull analog. The numbers in **Figure IV-4d** represent 8-bit grayscale shift values relative to the image backgrounds. A minimum of 5 grayscale shift value is required in the visualization of the samples qualitatively. As tantalum microparticle

loading % increased in AT foams, the X-ray visibility was gradually improved. For AT foams, the 8 mm thick sample was lightly visible in **Figure IV-4b** (grayscale shift 6) but all thicknesses/types of AT samples were hardly visible with the skull analog. The addition of tantalum microparticles enabled visualization of ATIPA foams through aluminum plate, even at neurovascular device scales. The crimped device of AT_2%T foam was slightly visible (grayscale shift 5), which became more clearly visible in AT_4%T (grayscale shift 8) and AT_8%T (grayscale shift 12). Even the expanded device was visible in AT_4%T (grayscale shift 6) and AT_8%T (grayscale shift 8). This is a remarkable improvement compared to the previous study by Nash et al. where either crimped or expanded neurovascular device prototypes were barely visible through X-ray imaging (grayscale shift 2).[90]

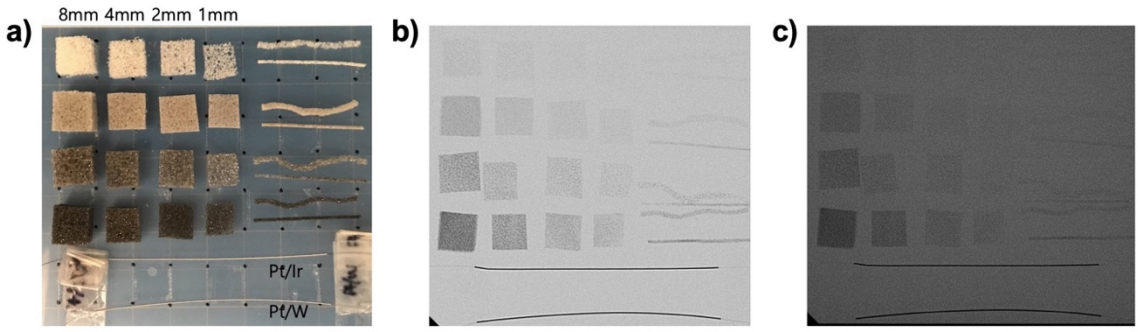

d)

	8mm	4mm	2mm	1mm	Expanded	Crimped
AT	**6** (2)	3 (1)	2 (1)	2 (0)	3 (0)	4 (2)
AT_2%T	**23** (**11**)	**11** (**5**)	**6** (3)	4 (1)	**7** (3)	**14** (**5**)
AT_4%T	**32** (**14**)	**14** (**8**)	**10** (**5**)	**6** (2)	**9** (**6**)	**19** (**8**)
AT_8%T	**71** (**27**)	**36** (**14**)	**20** (**9**)	**14** (**6**)	**19** (**8**)	**40** (**12**)

PT/Ir	**171** (**66**)
PT/W	**176** (**68**)

Figure IV-4. X-ray visibility of radiopaque ATIPA foams. a) ATIPA foam samples with varying thicknesses and NED prototypes aligned on a plastic tray. The first row is AT foams with 8,4,2, and 1 mm thicknesses. NED prototypes (2 mm diameter cylinders) in the expanded (top) and crimped (bottom) forms are at the right side of the image. The second, third, and fourth rows are AT_2%T, AT_4%T, and AT_8%T foams respectively. For positive controls, 0.008" OD 90/10 Pt/Ir coil and 0.008" OD 92/8 Pt/W coil are used which are at the very bottom of the image. b) Fluoroscopy image of the ATIPA foam samples. c) Fluoroscopy image with an 0.5" aluminum plate placed on top of the sample tray. d) Mean grayscale shift values of samples from the background using ImageJ. Numbers without parentheses are from the image (b) and numbers with parentheses are from the image (c). Grayscale shift values 5 and above are bolded.

Cytocompatibility test

The cytotoxicity of the ATIPA foams was investigated *in vitro* by adding foam extract media on the NIH/3T3 mouse fibroblasts. The cell viability was evaluated 48 h after adding the extract media using a resazurin assay. **Figure IV-5** shows that the cell viabilities for each foam compositions were very high (> 90%) which exceeds the 70% threshold to be considered noncytotoxic. The cell viabilities for ATIPA samples did not

show a significant difference from the negative control (100%). Furthermore, there was no significant difference found among the foam compositions.

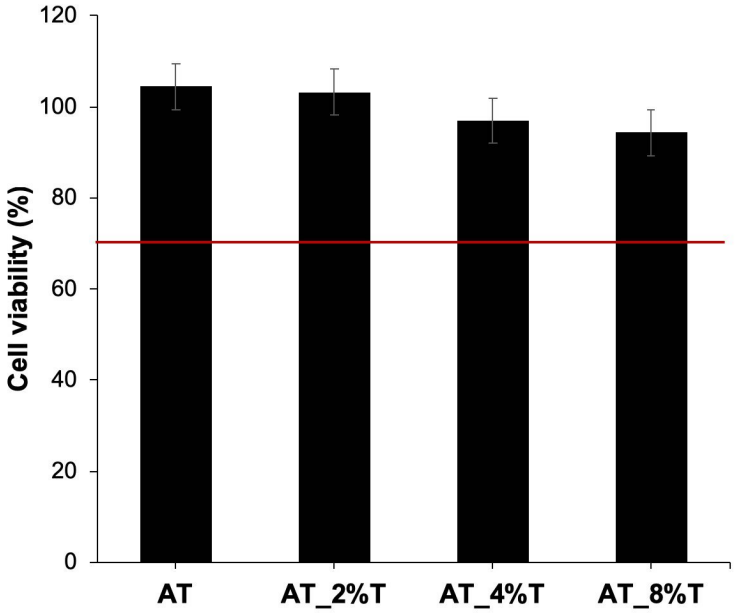

Figure IV-5. Cell viability results of the extract media test for the ATIPA foams (n=3) 48 h after the addition of extraction media to NIH/3T3 cells. Cell viability above the red line (> 70 %) indicates that there's not any cytotoxic effect of extract media according to ISO 10993-5.

Effects of E-beam sterilization

AT and AT_4%T compositions were selected to analyze the E-beam sterilization effect on the ATIPA foams. E-beam irradiation can cause both cross-linking and scission of polymer bonds, depending on the polymer structure.[96] Chemical, thermal, shape recovery, and mechanical properties of the foams were compared before and after E-beam sterilization at 43.6 kGy (**Figure IV-6**). ATR-FTIR was performed to analyze the chemical properties of the foams (**Figure IV-6a**). The IR peaks of E-beam sterilized

foams were mostly not affected by the E-beam radiation except at 841 cm^{-1} where a slight decrease of the peaks was observed in the E-beam sterilized foams (**Figure IV-6b**). The absorption peak at 841 cm^{-1} is attributed to CH_2 rocking vibration.[97],[98] The decrease in this peak indicates that crosslinking could have occurred in the polymer network. An electron beam can abstract hydrogen atoms from saturated carbon atoms forming macroradicals that could react with each other to form C-C crosslinks.[99] Glass transition temperatures were measured using DSC as shown in **Figure IV-6c**. The dry T_g's of E-beam sterilized foams were significantly higher than non-treated foams. The dry T_g's of both AT and AT_4%T were increased about 4 °C after the E-beam treatment which could be a result of cross-linking of polymer structure. Wet T_g's and expansion profiles (**Figure IV-6d**) were not significantly different after the E-beam sterilization. Tensile testing results showed increased ultimate tensile strength, toughness, and strain at break for AT foams and increased toughness and strain at break for AT_4%T after E-beam irradiation which further supports that crosslinking occurred in the polymer system.

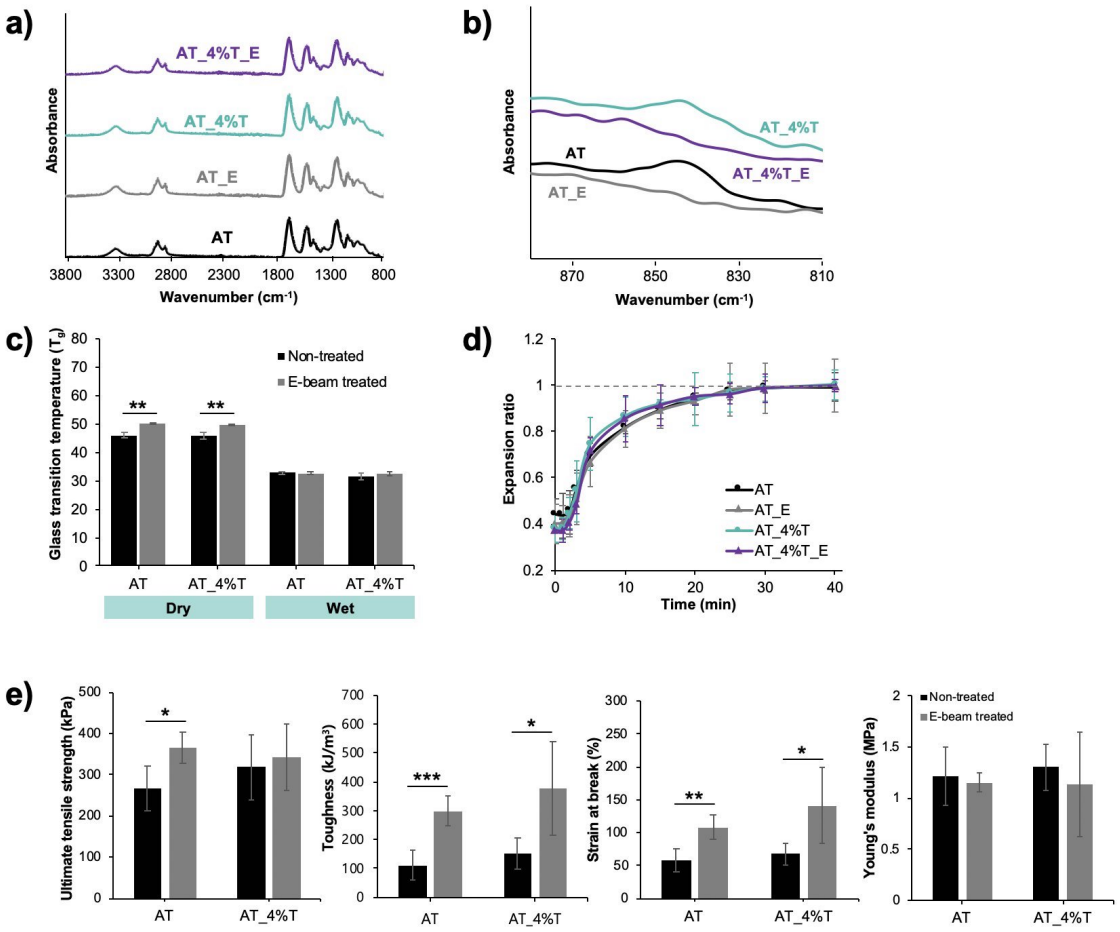

Figure IV-6. Electron-beam sterilization effect on AT and AT_4%T foams. a) ATR-IR spectra for the range of 800-3800 cm^{-1} wavenumber. b) Magnified ATR-IR spectra showing decreased peak after E-beam. c) Dry and wet T_g's measured using DSC (n=3). d) Expansion profile of crimped foams in 37 °C water (n=3). e) Tensile mechanical properties (n=5).

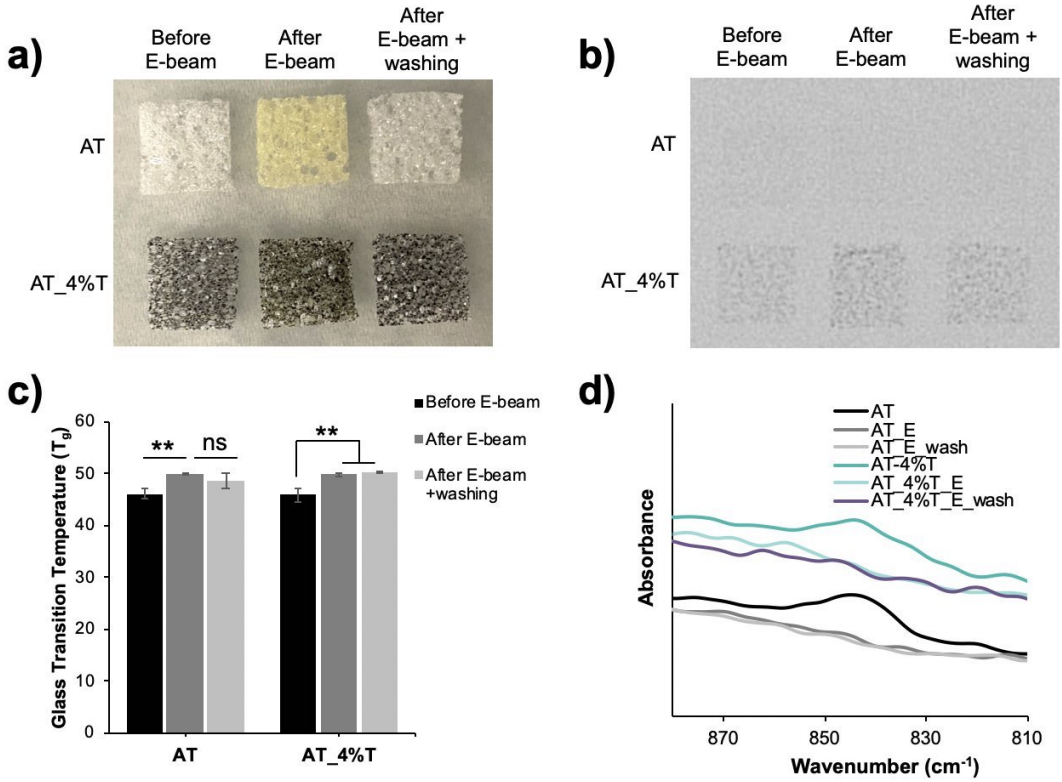

Figure IV-7. Additional effect of E-beam sterilization and washing with water on AT and AT_4%T foams. a) Color change observation. b) X-ray visibility (2 mm thickness) c) Dry T_g measured using DSC. d) ATR-IR peak at 810-880 cm^{-1} range.

In vitro degradation study

The *in vitro* degradability of E-beam sterilized ATIPA foams were analyzed in accelerated oxidative condition (20% H_2O_2, 37 °C) and in accelerated hydrolytic condition (0.1 N NaOH, 37 °C) over 90 days. Gravimetric analysis in **Figure IV-8a** shows that AT foam has 92.7% mass remaining after 90 days in the oxidative condition which is not much different from its gel fraction (92.1%) indicating that oxidative degradation barely occurred in AT foams. As the tantalum content was increased in the foam, the mass loss over time was increased in the oxidative condition. H40 foam is one

of the previously developed SMP foams from our group that contains tertiary amine bonds which get oxidized to amine oxide and further form primary amines, carboxylic acids, and aldehydes.[58] The H40 foam was included in degradation studies to compare degradation profiles with those of ATIPA foams. When compared to H40, AT_T foams showed a steady mass loss while H40 showed a sharp decrease at around 54 days. At 90 days, H40 had the lowest remaining mass of 24.6% followed by AT_8%T (27.6%), AT_4%T (44.5%), and AT_2%T (76.0%). In the hydrolytic degradation condition, ATIPA foams maintained a high percentage of their mass (84.4 – 89.1%, **Figure IV-8b**) at day 90. However, the remaining mass at day 90 were 6.2 - 8.4% lower than their gel fractions which suggests that hydrolytic degradation has occurred in the ATIPA foams. AT foams had the largest mass loss which is expected due to their lowest gel fraction.

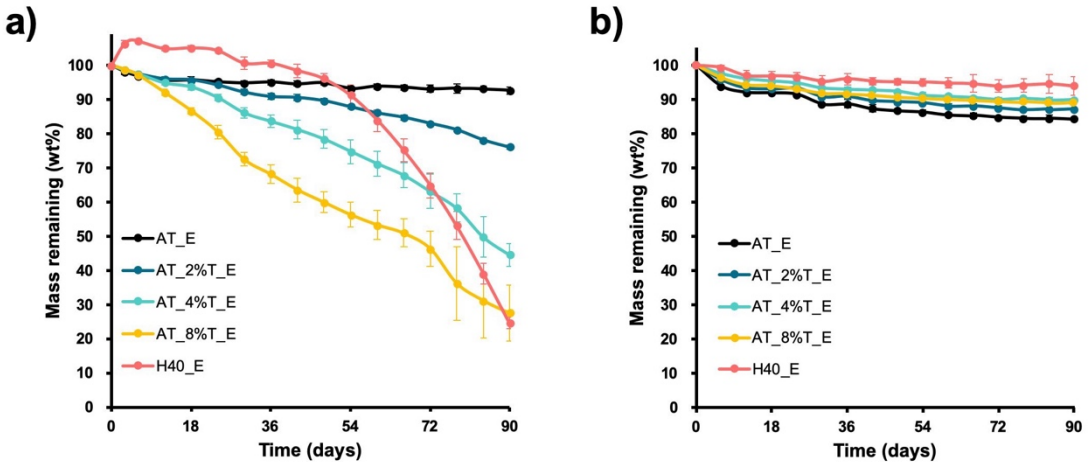

Figure IV-8. *In vitro* degradation studies performed by gravimetric analysis of ATIPA foams (n=3) in a) accelerated oxidative degradation solution (20% H_2O_2) and b) accelerated hydrolytic degradation solution (0.1 N NaOH) at 37 °C over 90 days. H40 foam was used to compare ATIPA foams with the previously developed low-density SMP foam.

Morphological analysis was performed every 18 days on the degraded foams using SEM (**Figure IV-9**). In the oxidative degradation condition, AT and AT_2%T did not show a significant difference during 90 days (**Figure IV-9a**). AT_4%T started to show membrane degradation at day 54 and pore shrinkage and clustering were observed in day 72 and day 90. AT_8%T showed faster membrane degradation and pore shrinkage starting from day 36 which was followed by clustering in day 72 and total material collapse in day 90. In H40, membrane degradation was observed in day 18 followed by fragmentation of foam struts in day 54 and total material collapse in day 90. These morphological results were consistent with the gravimetric results where H40 showed a sharp drop of mass at day 54 which is due to the strut fragmentation leading to a large loss of foam mass. In comparison, AT_4%T and AT_8%T foams did not show strut fragmentation like H40, but they showed foam clustering which led to their constant mass loss over time. In the hydrolytic degradation condition, all of the foam samples did not show a significant difference over 90 days (**Figure IV-9b**).

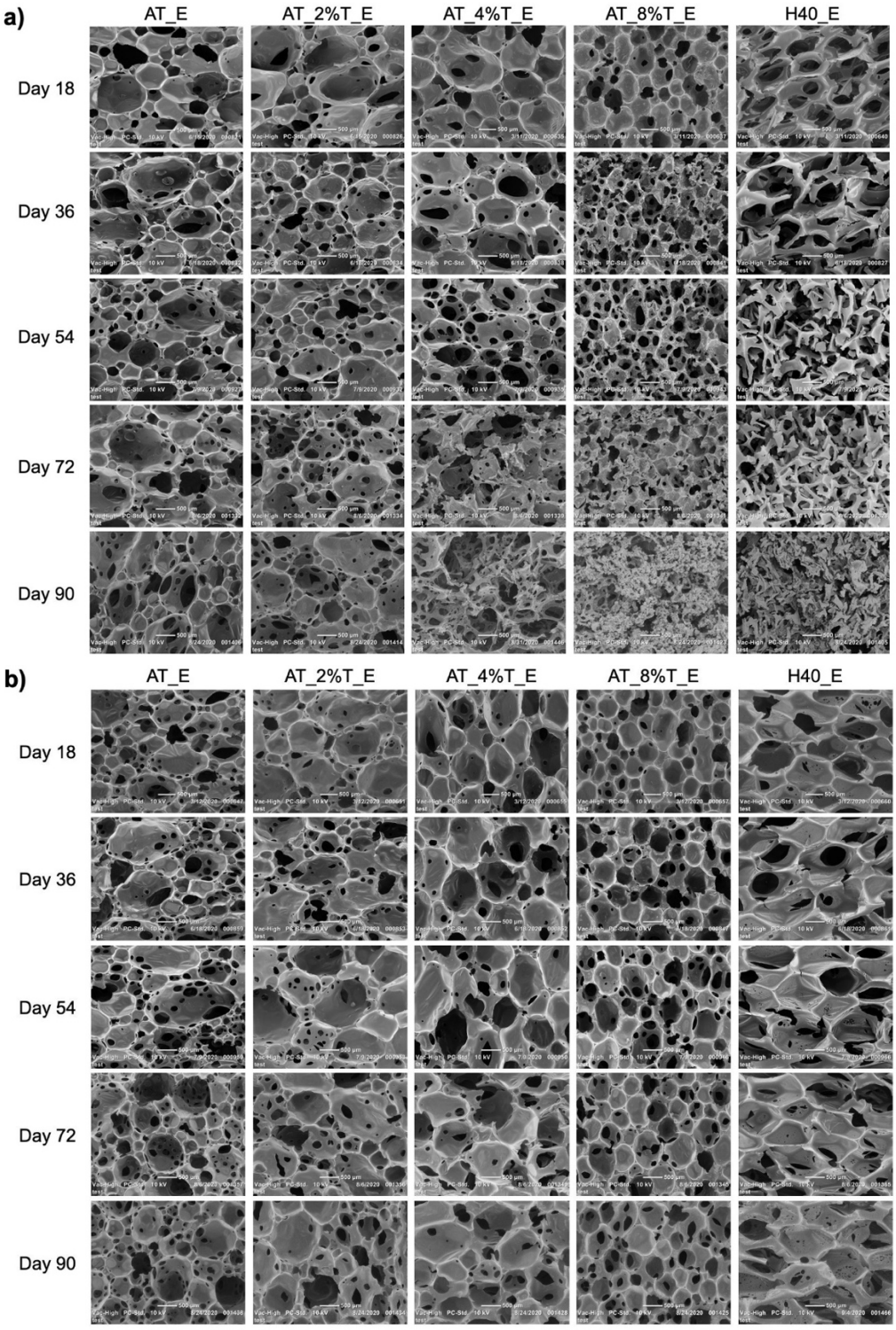

Figure IV-9. Morphological properties of degraded foams analyzed using SEM every 18 days up to 90 days. a) Accelerated oxidative degradation condition. b) Accelerated hydrolytic degradation condition.

Chemical analysis of the degraded foams was performed every 18 days of degradation using ATR-FTIR (**Figure IV-10**). IR spectra of AT, AT_2%T, and AT_4%T did not change significantly throughout 90 days in the oxidative condition (**Figure IV-10a**) even though AT_2%T and AT_4%T had a quite significant mass loss of 23.9 and 55.5% respectively after 90 days of oxidative degradation. This indicates that the mass loss is attributed to tantalum dissolution, leading to the loss of mechanical stability of the foams. ATIPA foams with a higher content of tantalum have a lower portion of polymer in the foam struts and membrane. Thus, as the tantalum content increases, the mechanical stability of the foams decreases due to the dissolution of tantalum in the presence of H_2O_2,[100] and the physical fragmentation of polymer increases in the oxidative degradation condition. The overall decrease in the IR peaks in AT_8%T, which can be observed in **Figure IV-10a**, is likely due to the severe fragmentation and erosion of the polymer. In the hydrolytic degradation condition, all of the ATIPA foams showed an increase in the peak at 1597 cm^{-1} (N-H bend from primary amine) and decrease at 1182 and 1100 cm^{-1} (C-N stretch) which indicates that hydrolysis of amide bonds between ATIPA monomer and HDI has occurred (**Figure IV-10b**). The IR peaks of H40 foam in the oxidative condition (**Figure IV-10a**) demonstrate the scission of C-N bond from the tertiary amine as the peak at 1052 cm^{-1} (C-N stretch) decreases. The scission of C-N bond results in the formation of secondary amines and aldehydes which further get oxidized to form carboxylic acids. The carbonyl shift from 1689 cm^{-1} to 1695 cm^{-1} indicates the formation of aldehydes and carboxylic acids. The peak at 1000 cm^{-1} corresponds to C-O stretch and the increase of the peak supports the

formation of carboxylic acids. The urea bonds (C=O) at 1638 cm^{-1} decreased over time as well as the amide II bonds at 1532 cm^{-1} and the amide III bonds at 1239 cm^{-1}. In hydrolytic degradation condition, there were not any significant changes in the IR peaks during 90 days of H40 degradation. These degradation results of H40 are congruent with the previously reported degradation results of polyurethane SMP foams.[58],[77]

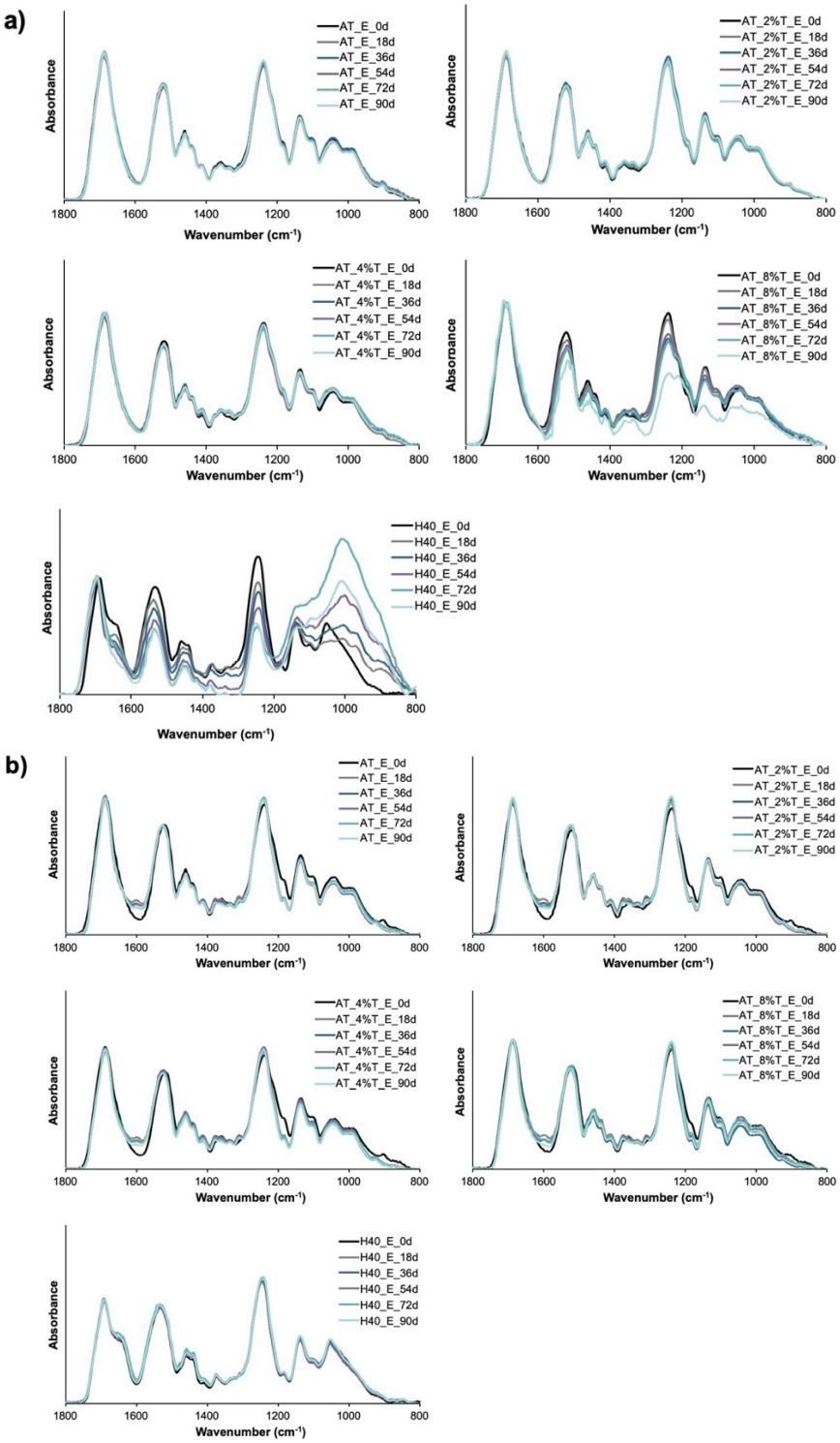

Figure IV-10. ATR-IR spectra of degraded foams over 90 days in a) accelerated oxidative degradation condition and b) accelerated hydrolytic degradation condition.

Extraction study

ICP-OES was used to measure the amount of extracted tantalum from a AT_2%T neurovascular device (2 mm diameter, 1 cm length) in polar and nonpolar extraction solutions (water and hexane respectively) under exaggerated extraction conditions. The extracted tantalum from the device was below detection limit (<0.1 μg/ml) in both polar and nonpolar extraction solutions.

ICP-OES was also used to analyze tantalum extraction in degradation solutions (20% H_2O_2 and 0.1N NaOH, 37°C, 72 hr) from AT_2%T neurovascular devices. An average of 1.5 $\pm$ 2.3 μg/ml tantalum was detected in 20% H_2O_2 and the total Ta amount extracted from the 1cm neurovascular device was calculated to be 6.7 $\pm$ 10.0 μg/ml. Tantalum quantification was below the detection limit (<0.2 μg/ml) for the 0.1N NaOH degradation solution.

Table IV-2. ICP-OES data for AT_2%T foams in various extraction solutions. (Detection limit is higher for 0.1N NaOH due to additional dilution.)

Extraction solution	Ta (μg/ml)	Ta (μg/device)
Water	< 0.1	< 0.4
Hexane	< 0.1	< 0.4
20% H_2O_2	1.5 $\pm$ 2.3	6.7 $\pm$ 10.0
0.1N NaOH	< 0.2	< 0.8

Discussion

The goal of this study was to develop SMP foam compositions with appropriate X-ray visibility on the neurovascular scale. Previously developed ATIPA foams showed

higher X-ray visibility with increasing density but showed limited visibility both in the crimped and expanded forms at the neurovascular scale.[90] Tantalum microparticles (~2um) were added to ATIPA foam premix to combine the chemical approach of incorporating iodine motifs in the foam system and the physical approach of loading radio-dense tantalum microparticles to achieve sufficient X-ray visualization. In a clinical setting, a NED foam should be visible in its crimped shape through fluoroscopy to enable device visualization during delivery into an intracranial aneurysm. Once the delivered foam expands to fill the aneurysm sac, clinicians check whether the aneurysm is properly embolized or not by imaging a contrast agent introduced through the bloodstream (angiography). The expanded device should not be too highly radio-dense since it can block the visibility of the contrast agent flowing into the aneurysm that is not properly embolized, in which case more NED foams are delivered to pack the aneurysm. All of the fabricated AT_T foams (AT_2%T, AT_4%T, and AT_8%T) showed sufficient X-ray visibility in their crimped shape. However, AT_2%T and AT_4%T showed more desirable X-ray visibility in the expanded form, being less radiopaque than AT_8%T. Therefore, the optimal X-ray visibility could be achieved in AT_2%T and AT_4%T foam compositions.

The tensile strength was increased with the increasing tantalum % in the foam, and the strain at break and toughness were decreased at higher tantalum loading % (AT_8%T). This trend is consistent with Hasan et al.'s work where the tungsten loaded SMP foam's material stiffness and strength were increased up to 4 vol% tungsten and higher loading of the additives resulted in decreasing toughness and strain at break.[89]

The tungsten loaded SMP foams could achieve sufficient X-ray visibility at tungsten content greater than 6 vol% of which the mechanical properties were diminished.[89] It is noteworthy that AT_2%T and AT_4%T foams showed sufficient X-ray visibility at the neurovascular scale with slightly improved mechanical properties. Also, ATIPA foams including AT_8%T have much higher toughness compared to previously developed low-density SMP foams due to the aromatic structures from the ATIPA monomer, which demonstrates that ATIPA foams can be mechanically stable under blood flow, lowering the risk of forming emboli due to foam fragmentation.

Biomedical devices can be sterilized in various ways, including ethylene oxide gas sterilization, E-beam radiation, and gamma radiation. E-beam radiation was chosen for a sterilization method in this study since E-beam radiation has more favorable sterilization conditions than the traditional ethylene oxide sterilization method (e.g., high heat, high humidity) for polyurethanes and also has shown to not prematurely actuate or alter any critical properties of SMP foam device in a previous study.[101] After E-beam sterilization, ultimate tensile strength (for AT foam only), toughness, and strain at break of ATIPA foams were increased but Young's modulus was not significantly impacted. Polymer crosslinking usually increases the modulus, ultimate tensile strength, and decreases the strain at break due to the crosslinking of intra- or intermolecular chains restricting the mobility of the polymer chains.[99] However, in highly porous material like ATIPA foams, modulus does not get affected by the crosslinking of polymer chains.[102] The strain at break was increased after the E-beam radiation due to the

elongation of pores to a higher extent resulting from the formation of tougher material after chain crosslinking.

In addition to the polymer chain crosslinking, E-beam sterilization changed the color of ATIPA foams to a more yellowish color (**Figure IV-7a**). The discoloration is commonly observed in various types of polymers after being irradiated by X-ray, gamma, or E-beam. The radiation can cause either permanent color change by rearranging bonds and forming covalent double bonds, or annealable color change by forming free radicals that get trapped in the polymeric matrix.[99] The discoloration observed in ATIPA foams was the latter where the original color could be recovered after washing the material in water. The trapped free radicals can react with water molecules and anneal out the color center. After the recovery of the original color, radiopacity, T_g, and chemical properties of the ATIPA foams were analyzed. There was no significant difference in those properties after the washing step (**Figure IV-7b-d**) which indicates that the increase of T_g and change in the IR after E-beam radiation (**Figure IV-6**) are not relevant to the color center formation but are due to the chain crosslinking.

In the *in vitro* degradation studies, it should be noted that AT foams showed significantly improved biostability in the oxidative degradation condition compared to the previously developed low-density SMP foams (H40 in this study) due to the absence of the tertiary amine-containing monomers which are susceptible to oxidative degradation.[58] Therefore, the mass loss observed for AT_T foams over 90 days is due to the tantalum dissolution. However, the mass loss over 90 days (24, 55, and 72 wt%

for AT_2%T, AT_4%T, and AT_8%T, respectively) was larger than the tantalum wt% in the foams (22, 36, and 52 wt%) and the mass consistently decreased during 90 days. This indicates the mass loss is also associated to the loss of foam particulates as the foam structure gets weaker during the tantalum dissolution. Since fragments from neurovascular foam possess the possibility of generating emboli in the bloodstream, the more oxidatively biostable AT_2%T is more appropriate composition for neurovascular devices than AT_4%T. However, it is very unlikely for the degrading material to enter the circulation since the developing clot isolates the foam material a few hours after the device implantation, and the foam is trapped in thrombus and developing scar tissue.

Extraction studies showed that tantalum was extracted out of AT_2%T device only in 20% H_2O_2, but not in water, hexane or 0.1N NaOH extraction solutions. This is attributed to the higher solubility of tantalum in the H_2O_2 solution compared to other extraction solutions which supports our degradation study results.[100] However, the extracted amounts were still very small, which did not exceed 20 μg per neurovascular device over three days in the accelerated condition. For a large aneurysm with a diameter of 25 mm, 234 cm of foam devices are needed to achieve 90% packing density, which is a high-end estimation for the amount of implanted foams. In this case, 0.031 mg/kg tantalum will be extracted per day for a 50 kg adult which is five orders of magnitude lower than the LD50 (lethal dose) level of tantalum (8000 mg/kg).[103] This extraction study result along with the cell viability result ensures the biocompatibility of AT_2%T device even with a much longer length of the foam device.

One limitation of AT_T foams is the short working time (~2 min) as shown in the expansion profile (**Figure IV-2d**). The clinicians need the working time in delivering the crimped foam through the blood vessel into the aneurysm sac using a microcatheter and the desired working time is around 5-10 min. Several methods can increase the working time for AT_T foams. First, more hydrophobic monomers could be used in the foam synthesis to decrease the water penetration rate into the crimped foam. Second, the foams can be crimped to a smaller diameter which would decrease the water penetration rate as well. In order to crimp foams more tightly, foams with a lower density could be fabricated by increasing the amount of blowing agent or using different surfactants. The foams can also be mechanically crimped into a smaller diameter since the foams could only be crimped down to 0.6 mm diameter in this study due to the crimper used which had the minimum crimping diameter of 0.6 mm. Therefore, a crimper that has a smaller minimum crimping diameter can decrease the crimped diameter of the AT_T foams. For a feasible delivery of the foam device into a tortuous human neurovasculature, the use of 0.017" (0.43 mm) or smaller inner diameter (ID) catheter is required. Thus, the foams would need to be crimped to a smaller diameter than 0.43 mm to be used for a neurovascular embolization device. In addition to increasing the working time and decreasing the crimped diameter, the biocompatibility of the degraded products needs to be analyzed *in vitro* and *in vivo* for future work to ensure the safety of using AT_T foams in neurovascular embolization applications.

Summary

Radiopaque SMP foams were developed using highly radio-dense tantalum microparticles and triiodobenzene containing SMP foam (ATIPA foam). The fabricated ATIPA foam-tantalum composites (AT_T) demonstrated clinically relevant thermal properties, faster expansion profiles, increased X-ray visibility, good cytocompatibility, and faster oxidative degradation compared to the control ATIPA foam without tantalum. The mechanical properties were improved up to 4 vol% tantalum and the most appropriate X-ray visibility could be achieved for the 2 vol% (AT_2%T) and 4 vol% (AT_4%T) tantalum foams. E-beam sterilization did not impair the critical properties of the ATIPA foams. Overall, AT_2%T was the optimal foam composition for neurovascular prototypes due to its high oxidative stability *in vitro* compared to previous low-density SMP foams. The AT_T foams are very promising materials with high toughness and sufficient X-ray visibility for use as neurovascular embolization devices.

CHAPTER V

THREE-DIMENSIONAL BIOPRINTING OF ANEURYSM-BEARING TISSUE STRUCTURE FOR ENDOVASCULAR DEPLOYMENT OF EMBOLIZATION COILS*

Introduction

The attractive features of endovascular treatment led to the active research and development of various endovascular devices to further enhance treatment efficacy, such as hydrogel coated coils,[104]–[106] growth factor coated coils,[107],[108] and shape memory polymer foam coated coils.[37] However, *in vitro* evaluation of clotting performance and predicting outcomes for new devices remain challenging. Modero et al. fabricated a patient-specific aneurysm model by 3D printing aneurysm geometry obtained from 3D computed tomography (CT) angiogram using water-dissolvable material which was then submerged in silicone and the printed geometry was dissolved after the silicone was cured. [109] Ohta et al. used poly-vinyl alcohol hydrogel instead of silicone to simulate the stiffness of the *in vivo* tissue which allowed for pulsations during flow.[110] However, these studies were confined to mimicking the anatomical aneurysm shape or

---

*Reprinted with permission from "Three-dimensional bioprinting of aneurysm-bearing tissue structure for endovascular deployment of embolization coils" by L. Jang, J. Alvarado, M. Pepona, E. Wasson, L. Nash, J. Ortega, A. Randles, D. Maitland, M. Moya, and W. Hynes, 2020. *Biofabrication*, 13, Copyright [2020] by IOP Publishing.

the mechanical stiffness of vascular tissues, and not the physiological cellular structure of blood vessels or extracellular matrices, which is a fundamental aspect of a functional *in vitro* aneurysm model for testing biocompatibility and healing efficiency of endovascular devices.

To study the cellular responses and healing effects of the endovascular devices, *in vivo* studies are generally performed in various animal models by artificially generating aneurysms using balloon inflation or elastase infusion techniques.[111],[112] However, reproducing the same anatomy or the same hemodynamic forces of human cerebral aneurysms in animal models is not currently achievable.[112] In addition, the artificially created surgical wound induces cellular migration (e.g., fibroblasts) into the lumen which is not observed in human cerebral aneurysms.[112] Healing responses also vary significantly between species which makes it challenging to apply the animal testing results to human physiology.

In this chapter, we present the first-ever *in vitro* living three-dimensional (3D) printed aneurysm possessing a fully-encapsulating extracellular matrix to interrogate treatment with an endovascular device. The model supports the growth of endothelial lined channels in a biocompatible matrix with physiologically relevant mechanical stiffness to brain tissue. The 3D printed platform is transparent and therefore allows for flow visualization at varying flow rates within the in vitro aneurysm through particle image velocimetry (PIV). We establish in this work the utility of this platform to provide critical data for 3D computational flow models and further demonstrate the

successful deployment of detachable coils inside the cell-laden aneurysm sac using a microcatheter to observe the in vitro clotting response of plasma.

Materials and Methods

Materials

Thrombin from bovine plasma (T4648, Sigma), Pluronic F127 (P2443, Sigma), gelatin from porcine skin, ~300 g Bloom, type A (G1890, Sigma), fibrinogen from bovine plasma, type I-S, 65-85% protein (F8630, Sigma), transglutaminase, TI formulation (TG) (Modernist Pantry), sodium hydroxide (NaOH) (S2770, Sigma), phosphate buffered saline without calcium and magnesium, pH 7.4, 1X (PBS) (10010-023, Gibco), Hank's balanced salt solution with calcium and magnesium, 1X (HBSS) (14025-092, Gibco), Calcium chloride (CaCl2) (C1016, Sigma), SE-1700 silicone, clear base, and SE-1700 catalyst (Dow Corning), Bovine plasma with sodium citrate (IGBOPLANAC500ML, Innovative Research), 1 μm 580/605 red fluorescent FluoSpheres (F13083, Thermofisher), 10% w/v neutral buffered formalin (VWR) info, Alexa Fluor 488 phalloidin (A12379) , Alexa Fluor 594 conjugated fibrinogen (F13193, Thermofisher)

HCMEC/D3 cell culture & maintenance

Cultures of immortalized human cerebral microvascular endothelial cells (hCMEC/D3, Cedarlane) were initiated in T-75 flasks pre-coated with 150 μg/mL rat tail collagen-Type I (Corning). Cells were maintained in EndoGRO MV culture media

(Millipore-Sigma) supplemented with 1% Penicillin-Streptomycin (Gibco) and 1 ng/mL human bFGF (Sigma) in a humidity-controlled CO_2 incubator held at 37 °C and 5% CO_2. The media was changed every other day until cultures were confluent and then sub-cultured according to the vendor's protocol.

3D printing of silicone sidewalls for bioreactor

Bioreactor sidewalls for the aneurysm platform were designed in SolidWorks, converted to G-code using open source Slic3r software, and then modified to integrate pump calls for the Ultimus V dispenser (Nordson EFD) using a custom Matlab script. Bioreactor walls were fabricated using SE-1700 silicone, prepared at a 10:1 elastomer to catalyst ratio and mixed with an ARV-310 centrifugal mixer (Thinky) at 2000 rpms for 2.5 min followed by a 15 min cooling step. This was repeated twice before loading the silicone material into a 10 mL EFD syringe (Nordson) and 3-5-minute centrifugation of the syringe at 3234 rcf to eliminate bubbles. The walls were then printed onto precleaned 3"x5" glass slides (VWR) using a custom extrusion-based bioprinter composed of CNC motion stages and controllers (Aerotech) connected to an Ultimus V precision dispenser. Post-printing, SE-1700 walls were cured at 65 °C for at least 2 hours, followed by autoclave sterilization.

Fugitive vascular ink preparation

Fugitive ink was prepared as previously described.[113] Pluronic F127 (34.1 wt%) and 100 U/mL (final concentration) thrombin in deionized water were added into a cold

syringe and centrifuged at 2000 rpm for 30 s for homogeneous mixing. The ink was cooled at -20 °C for 5 min and centrifuged again at 2000 rpm for 30 s. A piston was plunged into the syringe and the prepared ink was stored at 4 °C until use.

Matrix preparation

Gelatin stock solution was prepared by dissolving 15 g of gelatin powder in 75 mL of PBS. The mixture was placed on a magnetic stir plate set to 150 rpm at 70 °C overnight until fully dissolved. The pH value of the solution was adjusted to 7.5-7.54 using 1 N NaOH and brought to a final volume of 100 mL using additional PBS. The solution was then filter sterilized through a 0.22 μm PES filter, followed by aliquoting and storage at 4 °C until use. $CaCl_2$ stock solution (250 mM) was prepared by dissolving the salt in PBS on a magnetic stir plate set to 100 rpm at 90 °C until dissolved. The solution was then filter sterilized to remove any precipitate and stored at 4 °C until needed.

Fibrinogen (50 mg/mL, Sigma) was dissolved at 4 °C in PBS overnight, followed by warming to 37 °C before use. Transglutaminase (TG) solution (60 mg/mL) was prepared by dissolving TG powder (Moo Glue TI, Modern Pantry) in PBS less than 1 hour before use. The fibrinogen and TG solutions were then sterile filtered before mixing steps were performed. All components were warmed to 37 °C before mixing steps. Fibrinogen, PBS, TG, and $CaCl_2$ solutions were mixed at 37 °C and held for 5 min before the addition of gelatin (15 wt%). After gelatin was added the mixture was held at 37 °C for 20 min. Finally, 200 U/mL thrombin in PBS was added to the solution

at a final concentration of 1 U/mL and mixed. Final concentration of all components was 7.5 mg/mL gelatin, 10 mg/mL fibrinogen, 2 mg/mL TG, and 2.5 mM $CaCl_2$, and 1 U/mL thrombin. The solution (1mL) was quickly cast into the bioreactor, which was followed by the removal of 800 µL of the solution to remove any bubbles and leave a thin base layer. This layer was allowed to crosslink and partially dry at room temperature for 35 min before the printing step.

Fabrication of vascular tissue structure

A 1.19 mm nozzle (Nordson EFD) was used to print the fugitive ink on the base layer, forming the basis for the resulting vessel channels and aneurysm dome. The same matrix formulation used for the base layer gel was used to make the encapsulating gel solution. After encapsulating the printed vascular ink with the matrix solution, the silicone walls were then sealed with an additional glass slide. The bioreactor was then incubated at 37 °C for an hour, followed by incubation at 4 °C for 20 min to liquify the printed fugitive ink. Fugitive ink was removed by pulling out the liquified solution with a syringe, followed by rinsing with 5 mL of cold EndoGRO MV culture media.

Perfusion fluidics setup

The perfusion fluidics entry and exit reservoirs each consisted of GL45 glass bottles (Corning) with a two-port, 1/4-28 threaded, cap (Diba OmniFit). Each reservoir was connected to an air tubing (Tygon) in one port and a silicone media line in the other. Air tubing connected to the entry reservoir included two in-line PES, 0.2 µm membrane

syringe filters (Whatman) to ensure that the reservoir was not contaminated by the compressed air used to pressurize the reservoir for flow. The air tubing connected to the exit reservoir had one PES syringe filter in-line in order to both equilibrate the contained media and to release the pressure within the reservoir as media is passed through the platform.

After fluidic tubing (IDEX) was connected to the reservoirs, 85 mL of Endogrow MV media (equilibrated with 5% CO_2 for at least 2 hours) was then deposited in the entry reservoir, followed by 10 mL of media into the exit reservoir. Additionally, 5 mL of media was used to charge the fluidic tubing with media before final connections were made. MFS3 flow rate sensors (Elveflow) were sterilized with a 10% bleach solution for 10 min followed by an 8 times rinse with sterile diH_2O. The media line from the entry reservoir was then connected to one end of the flow rate sensor, with the other end of the flow sensor connected to the tubing extending from the bioreactor. The silicone tubing from the opposite side of the reactor was then connected via a union fitting to the exit reservoir's media line, completing the perfusion path. The air line attached to the entry reservoir was then connected to an OB1 microfluidic flow controller (Elveflow) to enable pressure control over the media within the reservoir. After the perfusion fluidics were constructed, the entire bioreactor was transferred to an incubator at 37 °C, 5% CO_2 and the flow rate was maintained at 10 μL/min overnight.

Endothelialization of aneurysm-bearing vessels

The *in vitro* aneurysm bioreactors were perfused with media at 10 μL/min for 24 hours before hCMECs were seeded within the channel lumen. The hCMECs were harvested and resuspended to a concentration of 1 x 10^6 cell/mL and allowed to attach to the channel for 15 min at 37 °C. The bioreactor was then inverted and allowed to sit for an additional 15 min at 37 °C. This cycle was repeated 3 times total and followed by a waiting period of 4 hours before the bioreactor was reconnected to flow at a rate of 10 μL/min for long-term culture. Every four days, 60 mL of media was exchanged between the exit reservoir and the entry reservoir for continued culture.

Particle image velocimetry (PIV) analysis

Particle image velocimetry (PIV) was performed on day 7 for all experiments involving endothelial cells. PIV was conducted using an Olympus IX83 inverted microscope equipped with LaVision FlowMaster 2-C components, including an Imager M-lite 2M CMOS camera, a 1 W, 532 nm gateable DPSS laser, and a PTU-X HS timing unit. A solution of fluorescent beads was prepared containing 3.49% 1 μm 580/605 FluoSpheres (Thermofisher) suspended in HBSS with ions. The bead solution was perfused through the *in vitro* aneurysm using a KDS-210 syringe pump (KD Scientific) set to volumetric flowrates ranging from 300 μL/min to 20 mL/min. PIV imaging was performed at predetermined positions within the artificial aneurysm and the Z-plane of imaging was selected by determining the focal point at the widest diameter of the vessel. PIV images were captured and processed using DaVis 10 software (LaVision) and

exported as .dat files for comparison and incorporation into the fluid dynamics computational model.

Fluorescence staining and imaging

After PIV imaging, printed vessel geometries were fixed in formalin and stained for actin. Briefly, fixed samples were rinsed twice with PBS, permeabilized with 0.5% (v/v) Tween-20 and stained with 1:40 Alexa Fluor 488 phalloidin for at least 1 hour at room temperature. Stained vessel geometries were imaged and reconstructed using tile-stitched Z-stacks gathered using a Zeiss LSM700 confocal microscope and Zen 2012 SP1 software (Carl Zeiss).

Computational flow modeling

The 3D surface model was reconstructed from segmented images of the aneurysm-bearing tissue structure, obtained by confocal microscopy, using the thresholding technique in the commercial image processing software Materialise Mimics. The 3D reconstructed surface model was exported as a mesh file in stereolithography (STL) file format. The open source modeling software Blender was used for mesh editing and converting the mesh file from STL to object file format (OFF), which can be imported into the computational fluid dynamics (CFD) solver. Volume measurements can be automatically obtained by the 3D printing toolbox, available as an add-on in Blender.

To computationally model the flow, we employed HARVEY, the in-house developed massively parallel CFD solver.[114] HARVEY is based on the lattice Boltzmann method (LBM), a mesoscopic modeling approach. In the LBM framework, distribution functions $f_i(\vec{x}, t)$ representing the density of particles at position $\vec{x}$ and time t with velocity $\vec{c_i}$ along the i^{th} lattice direction are tracked. The evolution of the distribution functions is governed by the lattice Boltzmann equation:

$$f_i(\vec{x} + \vec{c_i}\Delta t, t + \Delta t) = f_i(\vec{x}, t) + \Omega_i(\vec{x}, t).$$

Here, the Bhatnagar-Gross-Krook collision operator is considered, $\Omega_i(f) = -\frac{\Delta t(f_i - f_i^{eq})}{\tau}$.[115] The equilibrium distribution function f_i^{eq} is given by the Maxwell-Boltzmann distribution function. The relaxation time τ, determining the rate at which f_i relax towards f_i^{eq}, is related to the fluid kinematic viscosity by $\nu = c_s^2\left(\tau - \frac{\Delta t}{2}\right)$. $c_s = \frac{\Delta x}{(\sqrt{3}\Delta t)}$ denotes the lattice speed of sound, with Δx and Δt being respectively the lattice spacing and time step. The macroscopic quantities of the fluid, namely the density ρ and velocity $\vec{u}$, are given by the 0^{th} and 1^{st} moments of the distribution function:

$$\rho(\vec{x}, t) = \sum_i f_i(\vec{x}, t),$$

$$\vec{u}(\vec{x}, t) = \frac{\sum_i \vec{c_i} f_i(\vec{x}, t)}{\rho(\vec{x}, t)}$$

The simulations are performed using the D3Q19 lattice arrangement.[116] The fluid kinematic viscosity and density are taken equal to those of the bead solution in HBSS (with ions), that is $\nu = 0.9565\ mm^2/s$ and $\rho = 995.609 \frac{kg}{m^3}$. To ensure the stability and accuracy of the numerical solutions, we consider a relaxation time of $\tau = 1$ and 0.6 and fluid resolutions of 10 and 5 μm at the 0.3 and 20 mL/min flowrates, respectively. Finally, the no-slip boundary condition on the structure walls is applied by the half-way bounce-back scheme,[117] while the finite difference boundary scheme[118] is employed for enforcing the desired velocity and pressure profiles at the structure's inlet and outlets.

Deployment of detachable coils into the aneurysm platform

The aneurysm system used for coil deployment testing was cultured for 9 days before testing. A microcatheter (Vasco+, Balt Extrusion) was used to deliver two detachable coils (Barricade Complex Finish, 2 mm x 3 cm and 3 mm x 6 cm, Blockade Medical) into the printed aneurysm sac under static conditions. The microcatheter was carefully inserted into the metal pin and navigated to the aneurysm sac using brightfield microscopy. After placing the tip of the microcatheter at the neck of the aneurysm sac, the coil was dispensed from the microcatheter using the push wire until the entire coil was deployed in the aneurysm. The coil was detached from the push wire using an electrolytic detachment controller (Shape Memory Medical). The entirety of the insertion and detachment processes were monitored in real-time using brightfield microscopy.

Coil packing density calculation

The packing density of coils was calculated using the equation below.

$$Packing\ density = \frac{Coil\ volume}{Aneurysm\ sac\ volume} \times 100\%$$

The coil volume was calculated by assuming the bare platinum coil is a simple cylinder. The diameters of all the Barricade coils used in this study were 0.011". The length of coils used for the deployment testing was 9 cm and the coil length for the plasma clotting test was 8 cm. The aneurysm volume was measured from the reconstructed model in the computer simulation which provided accurate volumes of non-spherical aneurysms.

Plasma clotting within the coil-treated aneurysm sac

For clotting test, the aneurysm platform was cultured with hCMECs for 9 days and a detachable coil (3 mm × 8 cm) was delivered into the aneurysm sac using a microcatheter as mentioned above. Bovine plasma anticoagulated with sodium citrate was used for the clotting experiment. To initiate clotting, a stock solution of 800 mM $CaCl_2$ was added to the plasma to a final concentration of 10 mM. 147 µL of 1.5 mg/mL fluorescent fibrinogen stock was added to 10 mL of plasma which was then perfused through the channels using a syringe. The channels filled with plasma were held for 30 min at room temperature under static conditions. After 30 min, the channels were thoroughly rinsed via injection with 10 mL of HBSS to remove any uncoagulated plasma from inside the vessel channels. Clot formation within the aneurysm platform was then imaged using confocal microscopy.

Results

Fabrication of aneurysm-bearing tissue structure

The geometry of the printed aneurysm at the branching vessels is representative of an aneurysm at the basilar artery bifurcation. The elemental geometries used were based on previous publications where an idealized 2D computational model was developed to mimic an aneurysm at the basilar artery bifurcation.[119],[120] A 3.6 mm diameter aneurysm dome was created with an aneurysm neck width of 1.9 mm. The parent vessel was 2.4 mm wide while the branching vessels were 1.8 mm wide from the top point of view. The afferent and efferent vessels were connected to stainless steel tubes which were connected via fluidic tubing to media reservoirs with a pressurized entry reservoir and a vented exit reservoir, respectively. This bioreactor system allowed a constant flow of cell media through the vessels in the bioreactor (**Figure V-1A**). Fluorescent beads were perfused through the channels to confirm the complete evacuation of the fugitive ink from the complex aneurysm-bearing vessel structure. Precise and clear vessel structure embedded in the transparent gelatin-fibrin hydrogel were observed without showing any leakage from the vessels (**Figure V-1B**).

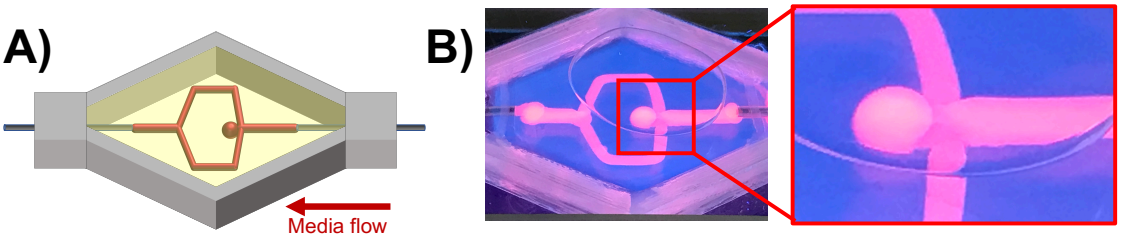

Figure V-1. The *in vitro* living cerebral aneurysm. A) Illustration of the 3D printed aneurysm bioreactor. B) The *in vitro* aneurysm vessel structure perfused with red fluorescent beads, demonstrating the formation of patent vessels post-evacuation of sacrificial ink.

Particle image velocimetry (PIV) measurement

Analyzing the hemodynamics around an aneurysm is very critical in understanding the mechanisms of aneurysm pathogenesis, progression, and rupture,[121],[122] evaluating the treatment efficacy,[123] and predicting the occlusion time after the treatment.[124] Particle image velocimetry (PIV) is a strong analyzing tool to quantitatively measure the flow dynamics within cerebral aneurysms and to validate computational simulation or clinical results.[125] **Figure V-2A** and **V-2B** demonstrates the flow dynamics within the channels of the *in vitro* living aneurysm platform. A flow rate of 300 μL/min was supplied to the channels which led to the average flow velocity (U_{avg}) of 1.18 mm/s for the parent vessel, 1.86 and 1.71 mm/s for the left and right daughter vessels respectively, 0.19 mm/s at the neck of the aneurysm, and no detectable flow inside the aneurysm sac (**Figure V-2A** and **Table V-1**). As the flow rate increased, the fluid motion within the aneurysm dome also increased and began exhibiting intra-aneurysmal circular flow at 20 mL/min flow rate showing U_{avg} of 0.88 mm/s (**Figure V-2B** and **Table V-2**). The high flow velocities of fluorescent beads in the parent and daughter vessels at 20 mL/min flow rate, however, could not be measured using PIV due to the low frame rate of the camera. The observed flow patterns were consistent with previous computational simulation results where the flow velocity in the aneurysm sac was more stagnant at the lower flow rate and at least one order of magnitude smaller than in the bifurcation channels.[126]–[128] In addition, many computational studies, as well as clinical studies, reported similar circular flow happening inside the bifurcation aneurysm sac at higher flow rates.[127]–[130] This demonstrates that the *in vitro* aneurysm

platform we developed can be used to simulate and analyze flow dynamics in cerebral aneurysms.

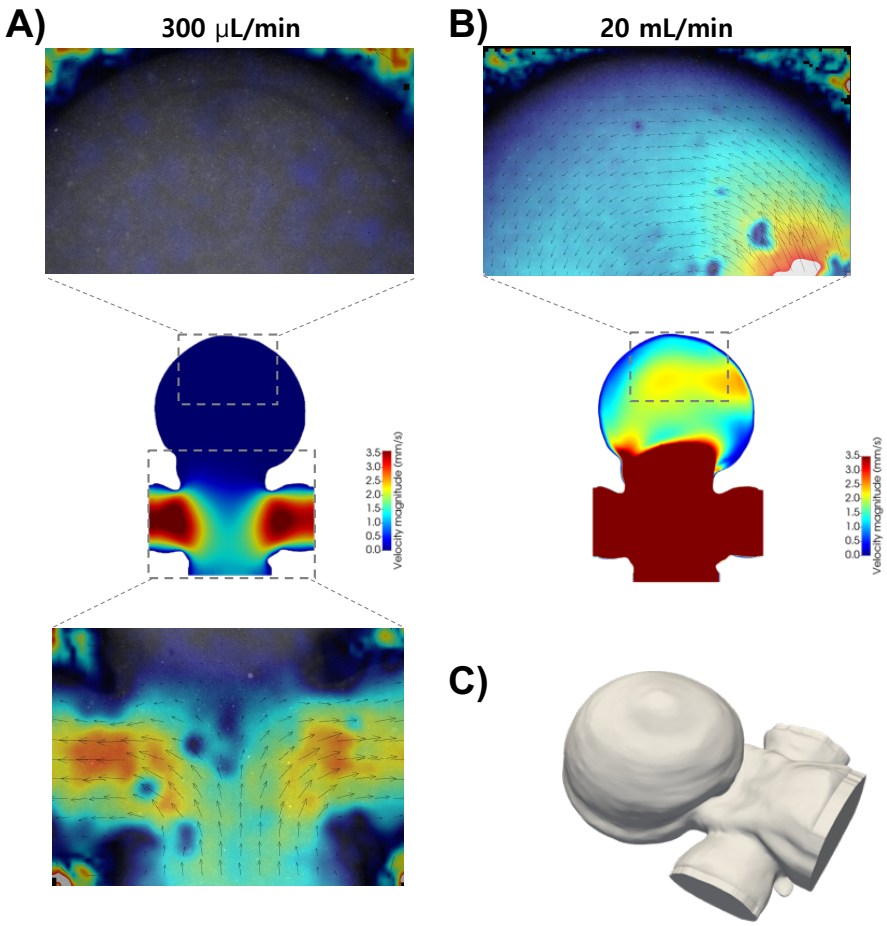

Figure V-2. Particle image velocimetry (PIV) analysis and 3D computational flow model simulations. A) Above: PIV measurement at the back of the aneurysm dome showing no detectable flow at a 300 µL/min flow rate. Middle: A 3D flow simulation of the same geometry and flow rate at z = -0.66 mm. Below: PIV measurements within the parent and daughter vessels captured with a 2x objective at the same flow rate. B) Above: PIV measurement gathered at the back of the aneurysm dome showing circular flow patterns and captured with a 4x objective at a 20 mL/min flow rate. Below: Simulation of the same geometry and flow rate demonstrating that fluid motion only occurs within the dome at high flow rates. C) High-fidelity geometric reconstruction of the printed living aneurysm constructed from image stacks gathered via confocal microscopy.

3D computational flow model simulation

The 3D printed aneurysm vessel was reconstructed as a 3D computational model using the image stacks from confocal microscopy (**Figure V-2C**). The flow simulations were demonstrated at flow rates of 300 μL/min and 20 mL/min to compare the flow patterns and velocities of the simulated models to those in the in vitro bioreactor at the given flow rates. The reconstructed model and the in vitro system displayed similar flow patterns, showing almost no flow inside the aneurysm sac at 300 μL/min and high flow at the starting points of two daughter vessels (**Figure V-2A**). The high-speed flow at the daughter vessels was due to the daughter vessels being printed with smaller vessel lumens at the branching point as shown in **Figure V-2C**. The U_{aver}'s for the parent vessel, daughter vessels, and the aneurysm neck region in the 3D computational model (at z = -0.66 mm) showed less than 50% relative error compared to those in PIV result (**Table V-1**). At 20 mL/min flow simulation, more active fluid motion was observed in the aneurysm sac (U_{aver} of 2.17 mm/s) which was consistent with the PIV result that showed active intra-aneurysmal circular flow (**Figure V-2B** and **Table V-2**). However, the relative error of U_{avg} between PIV (U_{avg} of 0.88 mm/s) and the computational model (U_{avg} of 1.70 mm/s) in the aneurysm sac was quite high (93.2%) which could be attributed to the vessel smoothing process during the reconstruction of the computational model slightly decreasing the vessel diameters and resulting in higher flow velocities in the vessels and in the aneurysm dome. Although the reconstruction process needs to be improved to decrease the flow velocity discrepancies between the simulation models and

the *in vitro* models, the general consistency between those models supports the flow dynamic information obtained in the *in vitro* platform.

Table V-1. Average flow velocities (U_{aver}) and maximum flow velocities (U_{max}) from different regions of the in vitro aneurysm platform at 300μL/min flow rate. For the PIV measurements, the average values of the average and maximum velocity magnitudes over 10 time instances along with the standard deviation (in parentheses) are reported.

	Parent		Left daughter		Right daughter		Aneurysm neck	
	U_{avg}	U_{max}	U_{avg}	U_{max}	U_{avg}	U_{max}	U_{avg}	U_{max}
PIV (mm/s)	1.18 (0.08)	2.32 (0.20)	1.86 (0.12)	3.74 (0.19)	1.71 (0.11)	3.41 (0.23)	0.19 (0.01)	0.61 (0.05)
HARVEY z = -0.65 mm (mm/s)	1.09	1.48	2.83	4.10	2.57	3.94	0.21	0.83
HARVEY z = -0.66 mm (mm/s)	1.00	1.38	2.68	3.88	2.43	3.74	0.21	0.80
HARVEY z = -0.67 mm (mm/s)	0.92	1.28	2.53	3.66	2.30	3.52	0.20	0.76
Relative error z = -0.65 mm (%)	7.6	36.2	52.2	9.6	50.3	15.5	10.5	36.1
Relative error z = -0.66 mm (%)	15.3	40.5	44.1	3.7	42.1	9.7	10.5	31.2
Relative error z = -0.67 mm (%)	22.0	44.8	36.0	2.1	34.5	3.2	5.3	24.6

Average relative error at z = -0.65 mm: 27.3 %

Average relative error at z = -0.66 mm: 24.6 %

Average relative error at z = -0.67 mm: 21.6 %

Table V-2. Average flow velocities (U_{avg}) and maximum flow velocities (U_{max}) from aneurysm sac of the in vitro aneurysm platform at 20 mL/min flow rate. For the PIV measurements, the average values of the average and maximum velocity magnitudes over 10 time instances along with the standard deviation (in parentheses) are reported.

	Aneurysm sac	
	U_{avg}	U_{max}
PIV (mm/s)	0.88 (0.03)	4.21 (0.28)
HARVEY (mm/s)	1.70	2.50
Relative error (%)	93.2	40.6

Endothelialization of aneurysm-bearing vessels

The innermost layer of cerebral arteries is composed of a single layer of endothelial cells which plays an important role in maintaining the vessel patency.[131] The endothelial cells are responsible for recanalization after the arterial occlusion,[21] or endothelium formation at the occluded aneurysm neck.[132] The hCMEC line has been investigated extensively because they retain most of the morphological characteristics of human blood–brain barrier (BBB) endothelial cells *in vitro*.[133],[134] In this study, hCMECs were seeded on the inner wall of the vessel structures to mimic the innermost cerebral blood vessel wall.[135] After seeding hCMECs, they were cultured for seven days to form a confluent single layer. They formed a uniform single layer along the walls of the channels and inside the aneurysm dome with actin filaments and closely associated phenotype (**Figure V-3**). It should be noted that endothelial cells which are present at the seam which is formed between the encapsulation and base-layer gels tend to prefer to grow along the seam, leading to higher intensity actin staining in these regions. This demonstrates the biocompatibility of the gelatin-fibrin hydrogel with

hCMECs as well as its feasibility to serve as a 3D vascularized tissue scaffold for *in vitro* aneurysm structures.

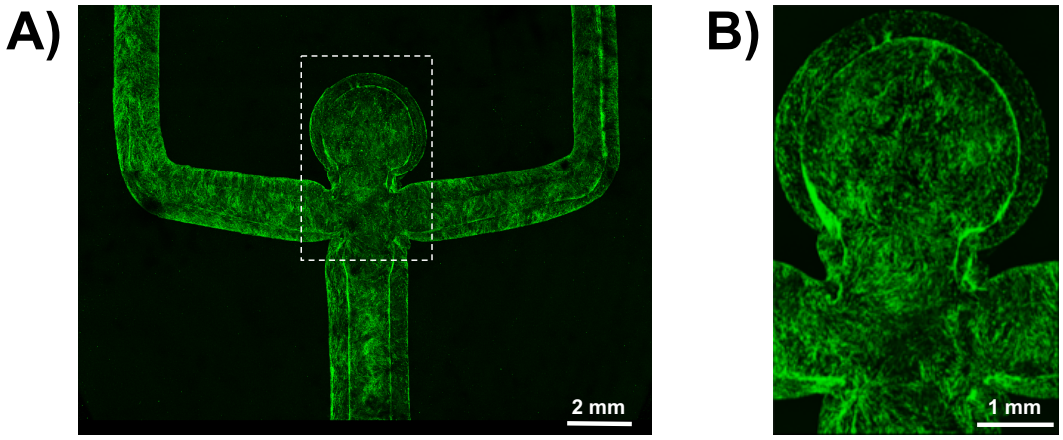

Figure V-3. Endothelialization of aneurysm-bearing printed vessels. A) Confocal image of actin stained endothelial cells after 7 days of perfusion culture. B) Close-up image of actin stained endothelium within the aneurysm dome, demonstrating fully confluent monolayer growth within the platform.

Deployment of detachable coils into the aneurysm sac

The approximate volume of the printed aneurysm dome was calculated to choose the right dimensions of coils to be inserted. Two detachable coils (3 mm × 6 cm and 2 mm × 3 cm) were delivered inside the aneurysm using a microcatheter as shown in **Figure V-4A**, resulting in a volumetric filling percentage of 36.5%. The coils were densely packed inside the aneurysm without protruding out to the parent vessel or piercing into the gelatin-fibrin hydrogel matrix (**Figure V-4B**). As the coils were being delivered, the tip and the side of the coils collided with the aneurysm walls, slightly, but reversibly, deforming the walls and scraping some endothelial cells off the aneurysm

wall. This endothelial denudation was previously reported in dense coil packing of aneurysms with Guglielmi detachable coils.[136] The removal of endothelial layer is considered necessary to promote thrombus formation, prevent recanalization, and improve the healing of endovascularly treated aneurysms.[132],[137] To evaluate whether the aneurysm dome was damaged or deformed during coil deployment, bare gel aneurysm channels were filled with fluorescent polystyrene beads (1 μm diameter) before and after the deployment and retraction of a 2 mm x 3 cm detachable coil (**Figure V-4C and D**). Confocal imaging of the aneurysm dome after the coil retraction showed the walls were fully intact and did not show any difference compared to the walls before the deployment, despite the deformation of gel seen during coiling. This demonstrates that while the vessels are highly compliant relative to silicone-based models, the sturdiness of the gelatin-fibrin hydrogel channels is robust enough to be readily used as a training platform for surgeons or as an *in vitro* testing system for embolization devices.

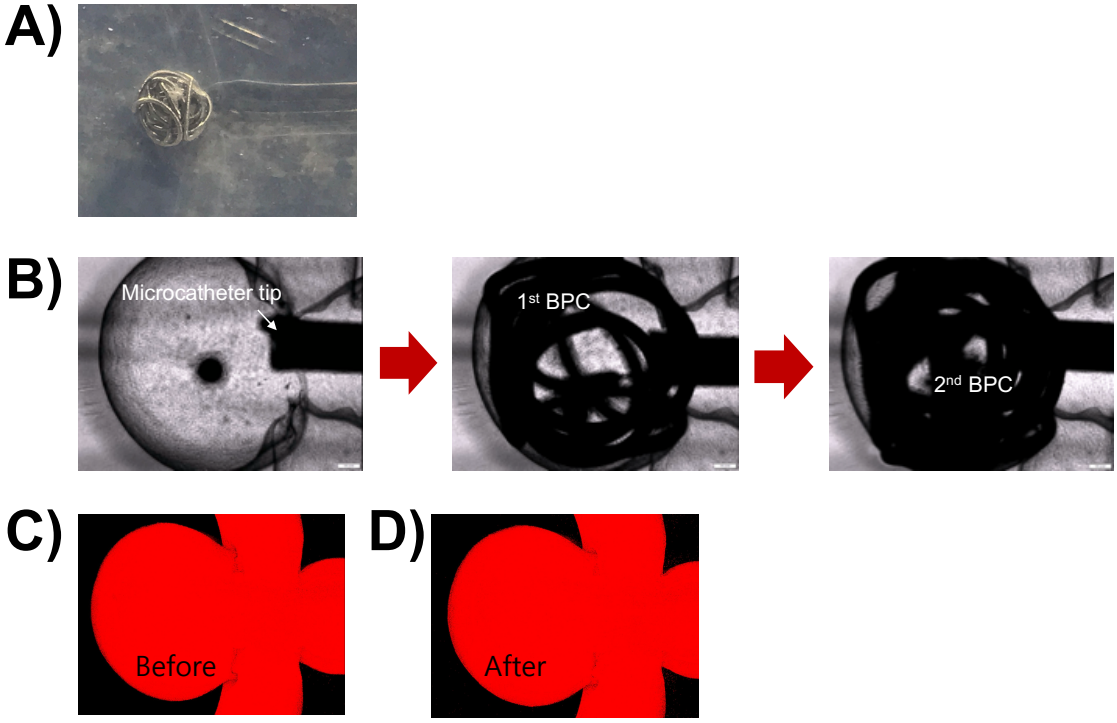

Figure V-4. Deployment of endovascular bare platinum coil (BPC) intervention treatment within the *in vitro* aneurysm. A) Image of dual coil deployment with the aneurysm dome. B) Micrographs of brightfield monitoring during BPC insertions from the endovascular microcatheter (1st BPC: 3 mm x 6 cm, 2nd BPC: 2 mm x 3 cm) C) Maximum projection confocal image stacks of an artificial aneurysm filled with 1 µm red fluorescent beads before and D) after BPC (2 mm x 3 cm) deployment and retraction, demonstrating no damage to the aneurysm sac during BPC insertion.

Plasma clot formation inside the aneurysm sac

The aneurysm platform used for the clotting test was endothelialized and packed with a detachable coil (3 mm x 8 cm) which filled 32.5% of the aneurysm sac volume. Coagulation-activated bovine plasma including fluorescent fibrinogen was injected through the endothelialized *in vitro* aneurysm with coils deployed in the aneurysm sac. Clot formation in the channels was observed using confocal microscopy under static

conditions. After a 30 min static dwell time, a significant clot was formed around the deployed coils in the aneurysm sac, but not at the branching point or outside the aneurysm sac (**Figure V-5**). A clot formation only around the occlusion device indicates that the *in vitro* aneurysm which is made of gelatin-fibrin gel does not trigger the clotting cascade of plasma through the contact pathway. This also shows that the deployed coils were densely packed in the aneurysm sac and had sufficient surface area to initiate clotting around the coils when performed under static conditions within the device. Overall, this proves the feasibility of the *in vitro* aneurysm platform to compare the coagulation efficiency of diverse embolization devices, to observe clotting behaviors under diverse flow rate, and to understand how clotting leads to a healing response.

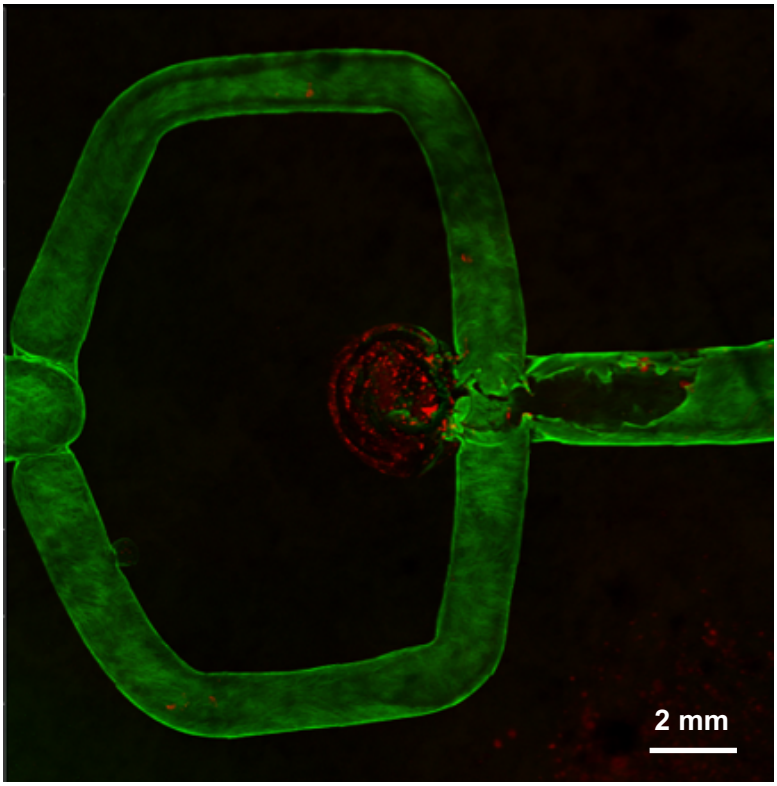

Figure V-5. Plasma clot formation in response to BPC deployment within *in vitro* living aneurysm dome. Maximum projection confocal image stack of the complete *in vitro* aneurysm after BPC deployment and injection with bovine plasma. Clot formation is visualized via accumulation of trace fluorescently labeled red human fibrinogen included with the plasma mixture. Endothelial cells are fluorescently stained green for actin. Imaging reveals clot formation and occlusion of the aneurysm sac, with no major clot formation present elsewhere in the vessel structures.

Discussion

This study presents for the first time the development of a printed *in vitro* living aneurysm platform with potential use in surgical intervention simulations and for analysis of clotting responses post-treatment. The system is made of compliant and biocompatible ECM material, gelatin-fibrin hydrogel, which has similar stiffness to the brain tissue compared to the previous aneurysm models.[42],[43],[110],[138] The brain tissue

without vasculature has reported elastic modulus of 0.1-1 kPa,[139],[140] while the existence of vasculature is likely to increase the mechanical modulus of the brain.[141],[142] Since the aim of the study was to analyze the hemodynamics and cellular responses inside the brain vessel that is embedded in the brain tissue, the elastic modulus of the gelatin-fibrin gel (1.1 kPa)[143] was considered suitable for this investigation.

Our platform allows for 3D printing complex vascular structure with variable sizes and geometries of vessel lumens and aneurysm domes. Many previous aneurysm *in vitro* models use stiff materials such as liquid resin,[43] silicon,[42],[144],[145] and polydimethylsiloxane (PDMS)[146] due to the ease of fabricating complex anatomical shapes. Although these systems are able to reproduce accurate shapes of aneurysms and are amenable for the testing of flow dynamics, they do not simulate the mechanical modulus of brain tissue which can derive inaccurate results for hemodynamic studies and are non-physiological environments for cell culture or endovascular device training. To address this limitation, some research groups have fabricated softer *in vitro* aneurysm models to address the problems using poly-vinyl alcohol hydrogel[110] or electrospun poly(D,L-lactide-co-glycolide) (PLGA) scaffolds,[147] however these approaches still are not comparable to the elastic modulus of brain tissue. The PLGA vessel scaffold from Cardinal group was cultured with human umbilical vein endothelial cells (HUVECs) and human umbilical artery smooth muscle cells (HUASMCs) and flow diverters were deployed to evaluate the cellular responses to this method of aneurysm treatment. However, the electrospun PLGA was not transparent which limited the visibility of cultured cells and the deployed devices inside the scaffold. Additionally, the method of

electrospinning PLGA upon a stainless-steel mandrel limits the vascular structure to that of a simple straight channel. Our *in vitro* platform is able to pattern a complex vasculature in soft, biocompatible, and transparent fibrin-gelatin hydrogel which can provide a brain tissue-like environment for cells and allows for straightforward visualization of cells or devices in the vessels. This *in vitro* model can be used for training surgeons or medical students to deploy neurovascular devices into a complex vascular structure and can be readily utilized in investigations related to analyzing clotting responses of embolization devices, healing responses after treatment, and the biophysical mechanisms of aneurysm formation or rupture using the resulting hemodynamic data.

Intracranial aneurysms are usually formed at places where abnormal hemodynamic forces are exerted upon the vascular wall.[148] Wall shear stress (WSS), which is a tangential force applied by blood flow against the endothelial cell lining is the key determinant of vascular remodeling.[149] Thus, matching the WSS's of the printed vessels to the physiological values is critical in developing the *in vitro* aneurysm platform. The assumptions we used to calculate the WSS's of the *in vitro* vessel structures are as follows: the flow splits into both daughter vessels equally after passing through the intersection, the printed vessels are in cylindrical shapes, and there is no contribution of compliance to vessel diameter under flow. At 20 mL/min flow rate, the calculated WSS was ~2.22 dyne/cm^2 for the parent vessel and ~2.63 dyne/cm^2 for the daughter vessel. These values were low compared to some literature values for arteries *in vivo* (10-70 dyne/cm^2) but were in-line with that of veins (1-6 dyne/cm^2).[150] Since

the platform is modeling an aneurysm on the basilar artery, the WSS of our printed vessels is an order of magnitude lower. However, this is primarily due to the limitations of the PIV imaging rate, and the syringe pump perfusion rate. These limitations can be addressed by using a faster PIV imaging rate and faster perfusion rate to achieve clinically relevant WSS values. In addition, the similar trend was observed in the flow velocities obtained from the computational model at 20 mL/min flow rate. The average velocity in the parent vessel was 13.4 cm/s which is smaller than the velocity at basilar arteries *in vivo* (~32.8 cm/s)[151] but within the range of that of cerebral veins (4-17 cm/s).[152] The computational 3D vascular flow model used here to recapitulate the experimental aneurysm flow velocities can also be used to simulate blood flow that forms physiologically relevant WSS and flow velocity on the printed vessels. The flow simulation will aid in predicting the hemodynamics, calculating flow velocities in the vessels or in the aneurysm sac, and predicting the clotting responses after endovascular treatment.

The main difficulty in comparing PIV data against computational results is that the location, as in z-coordinate, of the PIV images is unknown. Choosing different slices along the z-coordinate of the 3D simulation may result in significant differences in the velocity magnitude. The flow velocities from the simulation model at slightly different z slices (z = -0.65mm, - 0.66 mm, -0.67 mm) were analyzed at 300 μL/min flow rate (**Table V-1**). Although the three slices were only 10 μm apart, the velocity magnitudes were significantly different in each slice. The flow at the parent vessel showed smaller relative error at a slice closer to the center of the device (z = -0.65 mm), whereas the

errors for the rest of the device (left and right daughter vessels, aneurysm neck) decreased at a slice closer to the bottom wall (z = -0.67 mm). This indicates that the *in vitro* vessels are not perfectly flat but are in a slight inclination which leads to discrepancies between the experimental and computational data. Identifying the angle of a slice with respect to the xy-plane remains as a challenge in comparing PIV and computational models. In addition, disturbances in the flow that were observed in some of the PIV images could have led to the higher errors.

Low packing density of aneurysms using embolization coils is an important contributing factor of aneurysm recurrence after endovascular therapy, which increases the recurrence rate especially when the percent packing volume is less than 25%.[153],[154] Clinical treatments using bare platinum coils showed mean packing density of 23% with a range of 8-40% in randomized clinical trials.[25],[155],[156] The coil packing densities in our *in vitro* system were 32.5 and 36.5% which were well within the range of clinical trials and above the packing density of 25%. The aneurysm volume was measured from the reconstructed model in the computer simulation which provided accurate volumes of non-spherical aneurysms. This indicates that our *in vitro* model can be used to calculate accurate packing density of aneurysms using embolization devices and serve as a realistic model for testing the efficiencies of endovascular devices in aneurysm clotting and healing.

The potential significance of the *in vitro* living aneurysm platform is the ability to observe the cellular responses or the healing process after embolization treatment. For future studies, cells can be cultured for longer periods of time after the embolization

device deployment which may lead to the subsequent formation of endothelium at the neck of the aneurysm, which represents the ideal recovery outcome in aneurysm intervention treatments. It is currently highly challenging to observe or predict when and how the endothelium develops across the neck of the embolized aneurysms *in vivo* or in clinical studies.[157] However, the *in vitro* platform developed here can reveal the healing process near the occluded aneurysm in real-time, which can enable investigations directly upon the mechanism of vascular healing post-treatment. In addition, observing cellular behaviors under pulsatile flow, how the geometry of aneurysm neck affects the hemodynamics, and how the size of the aneurysm dome affects the treatment efficiency will be some possible future works that are of great interest.

Summary

Three-dimensionally (3D) printed aneurysm-bearing vascularized tissue structures were developed using gelatin-fibrin hydrogel of which the inner vessel walls were seeded with human cerebral microvascular endothelial cells (hCMECs). The hCMECs readily exhibited cellular attachment, spreading, and confluency all around the vessel walls, including the aneurysm walls. Additionally, the *in vitro* platform was directly amenable to flow measurements via particle image velocimetry, enabling the direct assessment of the vascular flow dynamics for comparison to a 3D computational fluid dynamics model. Detachable coils were delivered into the printed aneurysm sac through the vessel using a microcatheter and static blood plasma clotting was monitored

inside the aneurysm sac and around the coils. This biomimetic *in vitro* aneurysm model is a promising method for examining the biocompatibility and hemostatic efficiency of embolization devices and for providing hemodynamic information which would aid in predicting aneurysm rupture or healing response after treatment.

CHAPTER VI

CONCLUSIONS

Multiple functionalities of SMP foams have been improved in this dissertation which include biodegradability and fluid-uptake capacity for hemostatic application, and radiopacity for neurovascular embolization application. The biodegradability of SMP foams was enhanced by incorporating short chain ester-containing monomers in the foam system. The fabricated foams showed uniformly porous structure, improved mechanical strengths compared to the controls, excellent thermal properties along with rapid and full volume expansion (<8 min). Most importantly, faster degradation rate compared to the controls were achieved both in hydrolytic and oxidative solutions. Fluid absorption of SMP foams was increased by coating SMP foam with physically crosslinked gelatin-nanosilicate hydrogel, forming foam/hydrogel composite. The composite demonstrated 11 times higher swelling ratio, faster expansion rate, higher expansion force, and faster oxidative degradation rate compared to the control SMP foam. Hemostatic studies showed that the composite could clot blood at around three minute which was two times faster than the control SMP foam. Radiopacity of SMP foams was improved to ensure the safe delivery of the foam to the targeted aneurysm site. Highly radio-dense tantalum microparticles were added to the triiodobenzene containing SMP foam (ATIPA foam) premix to fabricate ATIPA foam-Tantalum composite (AT_T). The AT_T foams showed appropriate glass transition temperatures, faster expansion profile, increased X-ray visibility and faster oxidative degradation

compared to the control ATIPA foams. The mechanical properties were improved up to 4 vol% tantalum and the X-ray visibility was most appropriate at 2 vol% (AT_2%T) and 4 vol% (AT_4%T) tantalum foams with AT_2%T being the most ideal foam composition due to more stable oxidative degradation. Therefore, this dissertation shows promising and efficient ways to improve the biodegradability, fluid uptake capacity, and radiopacity of SMP foams for versatile biomedical applications.

In vitro living aneurysm system was 3D printed for the testing of novel endovascular interventions with the capability of enhancing the translation of experimental treatments from lab to clinical practice. Detachable coils were delivered through printed vessels using a microcatheter without penetrating the aneurysm dome, with the deployed coils successfully packed tightly within the aneurysm sac while achieving high percent packing volume (>30%). After 30 minutes of filling the vessels with bovine plasma, a significant clot was formed only at the embolized aneurysm, with no clotting observed at any other locations in the vessels. This key demonstration of the ability to perform a medical intervention with living *in vitro* constructs highlights the utility of this platform as a testbed to simulate treatment using embolization devices, analyze hemodynamics around the aneurysm sac, and observe the clotting properties of the deployed embolization devices. Furthermore, utilizing the *in vitro* platform as an experimental validation of predictive models will be a first step towards developing computation-based personalized medicine.

REFERENCES

1. Eastridge BJ, Hardin M, Cantrell J, Oetjen-Gerdes L, Zubko T, Mallak C, Wade CE, Simmons J, Mace J, Mabry R. Died of wounds on the battlefield: causation and implications for improving combat casualty care. J Trauma Acute Care Surg. 2011;71:S4–8.
2. Wedmore I, McManus JG, Pusateri AE, Holcomb JB. A special report on the chitosan-based hemostatic dressing: experience in current combat operations. J Trauma Acute Care Surg. 2006;60:655–8.
3. Holcomb JB, McMullin NR, Pearse L, Caruso J, Wade CE, Oetjen-Gerdes L, Champion HR, Lawnick M, Farr W, Rodriguez S. Causes of death in US Special Operations Forces in the global war on terrorism: 2001–2004. Ann Surg. 2007;245:986.
4. Eastridge BJ, Mabry RL, Seguin P, Cantrell J, Tops T, Uribe P, Mallett O, Zubko T, Oetjen-Gerdes L, Rasmussen TE, Butler FK, Kotwal RS, Holcomb JB, Wade C, Champion H, Lawnick M, Moores L, Blackbourne LH. Death on the battlefield (2001–2011): Implications for the future of combat casualty care. J Trauma Acute Care Surg [Internet]. 2012;73. Available from: https://journals.lww.com/jtrauma/Fulltext/2012/12005/Death_on_the_battlefield__2001_2011___.10.aspx
5. Sheppard FR, Macko A, Fryer DM, Ozuna KM, Brown AK, Crossland RF, Tadaki DK. Development of a nonhuman primate (rhesus macaque) model of uncontrolled traumatic liver hemorrhage. Shock. 2015;44:114–22.
6. Monroe MBB, Easley AD, Grant K, Fletcher GK, Boyer C, Maitland DJ. Multifunctional Shape-Memory Polymer Foams with Bio-inspired Antimicrobials. ChemPhysChem. 2018;19:1999–2008.
7. Holcomb JB, Stansbury LG, Champion HR, Wade C, Bellamy RF. Understanding combat casualty care statistics. J Trauma Acute Care Surg. 2006;60:397–401.
8. Kragh JFJ, Baer DG, Walters TJ. Extended (16-Hour) Tourniquet Application After Combat Wounds: A Case Report and Review of the Current Literature. J Orthop Trauma [Internet]. 2007;21. Available from: https://journals.lww.com/jorthotrauma/Fulltext/2007/04000/Extended__16_Hour__Tourniquet_Application_After.9.aspx
9. Mueller GR, Pineda TJ, Xie HX, Teach JS, Barofsky AD, Schmid JR, Gregory KW. A novel sponge-based wound stasis dressing to treat lethal noncompressible hemorrhage. J Trauma Acute Care Surg. 2012;73:S134–9.
10. Kragh JF, Aden JK, Steinbaugh J, Bullard M, Dubick MA. Gauze vs XSTAT in wound packing for hemorrhage control. Am J Emerg Med. 2015;33:974–6.
11. Peng T. Biomaterials for hemorrhage control. Trends Biomater Artif Organs. 2010;24:27–68.
12. Tomizawa Y. Clinical benefits and risk analysis of topical hemostats: a review. J Artif Organs. 2005;8:137–42.

13. Bal-Ozturk A, Karal-Yilmaz O, Akguner ZP, Aksu S, Tas A, Olmez H. Sponge-like chitosan-based nanostructured antibacterial material as a topical hemostat. J Appl Polym Sci. 2019;47522.
14. Fathi P, Sikorski M, Christodoulides K, Langan K, Choi YS, Titcomb M, Ghodasara A, Wonodi O, Thaker H, Vural M. Zeolite-loaded alginate-chitosan hydrogel beads as a topical hemostat. J Biomed Mater Res B Appl Biomater. 2018;106:1662–71.
15. Sukul M, Ventura RD, Bae SH, Choi HJ, Lee SY, Lee BT. Plant-derived oxidized nanofibrillar cellulose-chitosan composite as an absorbable hemostat. Mater Lett. 2017;197:150–5.
16. van Gijn J, Kerr RS, Rinkel GJ. Subarachnoid haemorrhage. The Lancet. 2007;369:306–18.
17. van Gijn J, Rinkel GJE. Subarachnoid haemorrhage: diagnosis, causes and management. Brain. 2001;124:249–78.
18. Solomon RA, Fink ME, Pile-Spellman J. Surgical management of unruptured intracranial aneurysms. J Neurosurg. 1994;80:440–6.
19. Claiborne Johnston S, Wilson CB, Halbach VV, Higashida RT, Dowd CF, McDermott MW, Applebury CB, Farley TL, Gress DR. Endovascular and surgical treatment of unruptured cerebral aneurysms: Comparison of risks. Ann Neurol. 2000;48:11–9.
20. Ishihara S, Mawad ME, Ogata K, Suzuki C, Tsuzuki N, Katoh H, Ohnuki A, Miyazawa T, Nawashiro H, Kaji T. Histopathologic findings in human cerebral aneurysms embolized with platinum coils: report of two cases and review of the literature. Am J Neuroradiol. 2002;23:970–4.
21. Castro E, Fortea F, Villoria F, Lacruz C, Ferreras B, Carrillo R. Long-term histopathologic findings in two cerebral aneurysms embolized with Guglielmi detachable coils. Am J Neuroradiol. 1999;20:549–52.
22. van der Schaaf I, Algra A, Wermer M, Molyneux A, Clarke MJ, van Gijn J, Rinkel GJ. Endovascular coiling versus neurosurgical clipping for patients with aneurysmal subarachnoid haemorrhage. Cochrane Database Syst Rev. 2005;
23. Carr SC, Pearce WH, Vogelzang RL, McCarthy WJ, Nemcek Jr AA, Yao JS. Current management of visceral artery aneurysms. Surgery. Elsevier; 1996;120:627–34.
24. Cognard C, Weill A, Spelle L, Piotin M, Castaings L, Rey A, Moret J. Long-term angiographic follow-up of 169 intracranial berry aneurysms occluded with detachable coils. Radiology. Radiological Society of North America; 1999;212:348–56.
25. Sluzewski M, van Rooij WJ, Slob MJ, Bescós JO, Slump CH, Wijnalda D. Relation between aneurysm volume, packing, and compaction in 145 cerebral aneurysms treated with coils. Radiology. 2004;231:653–8.
26. Landsman T, Touchet T, Hasan S, Smith C, Russell B, Rivera J, Maitland D, Cosgriff-Hernandez E. A shape memory foam composite with enhanced fluid uptake and bactericidal properties as a hemostatic agent. Acta Biomater. 2017;47:91–9.
27. Singhal P, Rodriguez JN, Small W, Eagleston S, Van de Water J, Maitland DJ, Wilson TS. Ultra low density and highly crosslinked biocompatible shape memory polyurethane foams. J Polym Sci Part B Polym Phys. 2012;50:724–37.

28. Singhal P, Boyle T, Infanger S, Letts S, Small W, Maitland D, Wilson T. Controlling the rate of actuation of shape memory polymer foams in water. Macromol Chem Phys. 2012;
29. Landsman TL, Bush RL, Glowczwski A, Horn J, Jessen SL, Ungchusri E, Diguette K, Smith HR, Hasan SM, Nash D, Clubb FJ, Maitland DJ. Design and verification of a shape memory polymer peripheral occlusion device. J Mech Behav Biomed Mater. 2016;63:195–206.
30. Ortega J, Hartman J, Rodriguez J, Maitland D. Virtual treatment of basilar aneurysms using shape memory polymer foam. Ann Biomed Eng. 2013;41:725–43.
31. Rodriguez JN, Miller MW, Boyle A, Horn J, Yang C-K, Wilson TS, Ortega JM, Small W, Nash L, Skoog H, Maitland DJ. Reticulation of low density shape memory polymer foam with an in vivo demonstration of vascular occlusion. J Mech Behav Biomed Mater. 2014;40:102–14.
32. Rodriguez JN, Clubb FJ, Wilson TS, Miller MW, Fossum TW, Hartman J, Tuzun E, Singhal P, Maitland DJ. In vivo response to an implanted shape memory polyurethane foam in a porcine aneurysm model. J Biomed Mater Res A. 2014;102:1231–42.
33. Jansen A-JS, van Schaik PM, Martens JM, Reijnen MMPJ. Embolization of the false lumen using IMPEDE-FX embolization plugs as part of treatment of an infrarenal post-dissection aneurysm: a case report. CVIR Endovasc. 2020;3:91.
34. Yu Y-J, Hearon K, Wilson TS, Maitland DJ. The effect of moisture absorption on the physical properties of polyurethane shape memory polymer foams. Smart Mater Struct. 2011;20:085010.
35. Cutting K. Managing wound exudate using a super-absorbent polymer dressing: a 53-patient clinical evaluation. J Wound Care. 2009;18:200–5.
36. Lloyd L, Kennedy J, Methacanon P, Paterson M, Knill C. Carbohydrate polymers as wound management aids. Carbohydr Polym. Elsevier; 1998;37:315–22.
37. Herting SM, Ding Y, Boyle AJ, Dai D, Nash LD, Asnafi S, Jakaitis DR, Johnson CR, Graul LM, Yeh C, Kallmes DF, Kadirvel R, Maitland DJ. In vivo comparison of shape memory polymer foam-coated and bare metal coils for aneurysm occlusion in the rabbit elastase model. J Biomed Mater Res B Appl Biomater. John Wiley & Sons, Ltd; 2019;107:2466–75.
38. Boyle AJ, Wierzbicki MA, Herting S, Weems AC, Nathan A, Hwang W, Maitland DJ. In vitro performance of a shape memory polymer foam-coated coil embolization device. Med Eng Phys. Elsevier; 2017;49:56–62.
39. Horn J, Hwang W, Jessen SL, Keller BK, Miller MW, Tuzun E, Hartman J, Clubb Jr. FJ, Maitland DJ. Comparison of shape memory polymer foam versus bare metal coil treatments in an in vivo porcine sidewall aneurysm model. J Biomed Mater Res B Appl Biomater. John Wiley & Sons, Ltd; 2017;105:1892–905.
40. Ford MD, Nikolov HN, Milner JS, Lownie SP, DeMont EM, Kalata W, Loth F, Holdsworth DW, Steinman DA. PIV-measured versus CFD-predicted flow dynamics in anatomically realistic cerebral aneurysm models. J Biomech Eng. 2008;130:021015.
41. Berry E, Marsden A, Dalgarno K, Kessel D, Scott D. Flexible tubular replicas of abdominal aortic aneurysms. Proc Inst Mech Eng [H]. 2002;216:211–4.

42. Sugiu K, MARTIN J-B, Jean B, Gailloud P, Mandai S, Rufenacht DA. Artificial cerebral aneurysm model for medical testing, training, and research. Neurol Med Chir (Tokyo). 2003;43:69–73.
43. Gailloud P, Pray J, Muster M, Piotin M, Fasel J, Rüfenacht D. Anin vitro anatomic model of the human cerebral arteries with saccular arterial aneurysms. Surg Radiol Anat. 1997;19:119–21.
44. O'Rourke MJ, McCullough JP. A comparison of the measured and predicted flowfield in a patient-specific model of an abdominal aortic aneurysm. Proc Inst Mech Eng [H]. 2008;222:737–50.
45. Mu L, Li X, Chi Q, Yang S, Zhang P, Ji C, He Y, Gao G. Experimental and numerical study of the effect of pulsatile flow on wall displacement oscillation in a flexible lateral aneurysm model. Acta Mech Sin. Springer; 2019;35:1120–9.
46. Li J, Wu X, Wu Y, Tang Z, Sun X, Pan M, Chen Y, Li J, Xiao R, Wang Z. Porous chitosan microspheres for application as quick in vitro and in vivo hemostat. Mater Sci Eng C. 2017;77:411–9.
47. Jiang X, Wang Y, Fan D, Zhu C, Liu L, Duan Z. A novel human-like collagen hemostatic sponge with uniform morphology, good biodegradability and biocompatibility. J Biomater Appl. 2017;31:1099–107.
48. Singhal P, Small W, Cosgriff-Hernandez E, Maitland DJ, Wilson TS. Low density biodegradable shape memory polyurethane foams for embolic biomedical applications. Acta Biomater. 2014;10:67–76.
49. Weems AC, Wacker KT, Maitland DJ. Improved oxidative biostability of porous shape memory polymers by substituting triethanolamine for glycerol. J Appl Polym Sci. 2019;47857.
50. Li J, Sha Y. A convenient synthesis of amino acid methyl esters. Molecules. 2008;13:1111–9.
51. Easley AD, Monroe MBB, Hasan SM, Weems AC, Frederick J, Maitland DJ. Shape memory polyurethane-urea foams with improved toughness. J Appl Polym Sci. 2019;136:47268.
52. Dounis DV, Wilkes GL. Influence of diethanolamine on hard segment ordering in flexible polyurethane foams. J Appl Polym Sci. 1997;65:525–37.
53. Alarhayem AQ, Myers JG, Dent D, Liao L, Muir M, Mueller D, Nicholson S, Cestero R, Johnson MC, Stewart R, O'Keefe G, Eastridge BJ. Time is the enemy: Mortality in trauma patients with hemorrhage from torso injury occurs long before the "golden hour." Southwest Surg Congr. 2016;212:1101–5.
54. Kotwal RS, Howard JT, Orman JA, Tarpey BW, Bailey JA, Champion HR, Mabry RL, Holcomb JB, Gross KR. The effect of a golden hour policy on the morbidity and mortality of combat casualties. JAMA Surg. 2016;151:15–24.
55. Tierney CM, Haugh MG, Liedl J, Mulcahy F, Hayes B, O'Brien FJ. The effects of collagen concentration and crosslink density on the biological, structural and mechanical properties of collagen-GAG scaffolds for bone tissue engineering. J Mech Behav Biomed Mater. 2009;2:202–9.

56. Jeon O, Song SJ, Lee K-J, Park MH, Lee S-H, Hahn SK, Kim S, Kim B-S. Mechanical properties and degradation behaviors of hyaluronic acid hydrogels cross-linked at various cross-linking densities. Carbohydr Polym. 2007;70:251–7.
57. Nash LD, Docherty NC, Monroe MBB, Ezell KP, Carrow JK, Hasan SM, Gaharwar AK, Maitland DJ. Cold plasma reticulation of shape memory embolic tissue scaffolds. Macromol Rapid Commun. 2016;37:1945–51.
58. Weems AC, Wacker KT, Carrow JK, Boyle AJ, Maitland DJ. Shape memory polyurethanes with oxidation-induced degradation: In vivo and in vitro correlations for endovascular material applications. Acta Biomater. 2017;59:33–44.
59. Wu Y, Li W, Zhang M, Wang X. Oxidative degradation of synthetic ester and its influence on tribological behavior. Tribol Int. 2013;64:16–23.
60. Feng Y, Li C. Study on oxidative degradation behaviors of polyesterurethane network. Polym Degrad Stab. 2006;91:1711–6.
61. Burkersroda F von, Schedl L, Göpferich A. Why degradable polymers undergo surface erosion or bulk erosion. Biomaterials. 2002;23:4221–31.
62. Gorna K, Gogolewski S. Preparation, degradation, and calcification of biodegradable polyurethane foams for bone graft substitutes. J Biomed Mater Res A. 2003;67A:813–27.
63. Guo A, Javni I, Petrovic Z. Rigid polyurethane foams based on soybean oil. J Appl Polym Sci. 2000;77:467–73.
64. Collins NJ, Bridson RH, Leeke GA, Grover LM. Particle seeding enhances interconnectivity in polymeric scaffolds foamed using supercritical CO2. Acta Biomater. 2010;6:1055–60.
65. Tan JY, Chua CK, Leong KF. Indirect fabrication of gelatin scaffolds using rapid prototyping technology. Virtual Phys Prototyp. 2010;5:45–53.
66. Blackwood KA, McKean R, Canton I, Freeman CO, Franklin KL, Cole D, Brook I, Farthing P, Rimmer S, Haycock JW, Ryan AJ, MacNeil S. Development of biodegradable electrospun scaffolds for dermal replacement. Biomaterials. 2008;29:3091–104.
67. Simmons A, Padsalgikar AD, Ferris LM, Poole-Warren LA. Biostability and biological performance of a PDMS-based polyurethane for controlled drug release. Biomaterials. 2008;29:2987–95.
68. Parker T, Dave V, Falotico R. Polymers for drug eluting stents. Curr Pharm Des. 2010;16:3978–88.
69. Health Council of the Netherlands: Committeee on Updating of Occupational Exposure Limits, Oxalic acid; Health-based reassessment of administrative occupational exposure limits, : Health Council of the Netherlands, The Hague, . 2000/15OSH/106. 2004.
70. Tsujihata M. Mechanism of calcium oxalate renal stone formation and renal tubular cell injury. Int J Urol. 2008;15:115–20.
71. Bennett-Guerrero E, Sorohan JG, Gurevich ML, Kazanjian PE, Levy RR, Barbera AV, White WD, Slaughter TF, Sladen RN, Smith PK. Cost-Benefit and Efficacy of Aprotinin Compared with ε-Aminocaproic Acid in Patients Having Repeated Cardiac

Operations A Randomized, Blinded Clinical Trial. Anesthesiol J Am Soc Anesthesiol. 1997;87:1373–80.
72. Kang H-W, Tabata Y, Ikada Y. Fabrication of porous gelatin scaffolds for tissue engineering. Biomaterials. 1999;20:1339–44.
73. Gaharwar AK, Avery RK, Assmann A, Paul A, McKinley GH, Khademhosseini A, Olsen BD. Shear-Thinning Nanocomposite Hydrogels for the Treatment of Hemorrhage. ACS Nano. 2014;8:9833–42.
74. Lokhande G, Carrow JK, Thakur T, Xavier JR, Parani M, Bayless KJ, Gaharwar AK. Nanoengineered injectable hydrogels for wound healing application. Acta Biomater. 2018;70:35–47.
75. Singhal P, Rodriguez JN, Small W, Eagleston S, Van de Water J, Maitland DJ, Wilson TS. Ultra low density and highly crosslinked biocompatible shape memory polyurethane foams. J Polym Sci Part B Polym Phys. 2012;50:724–37.
76. Xavier JR, Thakur T, Desai P, Jaiswal MK, Sears N, Cosgriff-Hernandez E, Kaunas R, Gaharwar AK. Bioactive nanoengineered hydrogels for bone tissue engineering: a growth-factor-free approach. ACS Nano. 2015;9:3109–18.
77. Jang LK, Fletcher GK, Monroe MBB, Maitland DJ. Biodegradable shape memory polymer foams with appropriate thermal properties for hemostatic applications. J Biomed Mater Res A. John Wiley & Sons, Ltd; 2020;108:1281–94.
78. Alcala-Orozco CR, Mutreja I, Cui X, Kumar D, Hooper GJ, Lim KS, Woodfield TB. Design and characterisation of multi-functional strontium-gelatin nanocomposite bioinks with improved print fidelity and osteogenic capacity. Bioprinting. Elsevier; 2020;18:e00073.
79. Yao Q, Fuglsby KE, Zheng X, Sun H. Nanoclay-functionalized 3D nanofibrous scaffolds promote bone regeneration. J Mater Chem B. Royal Society of Chemistry; 2020;8:3842–51.
80. Chimene D, Miller L, Cross LM, Jaiswal MK, Singh I, Gaharwar AK. Nanoengineered osteoinductive bioink for 3D bioprinting bone tissue. ACS Appl Mater Interfaces. ACS Publications; 2020;12:15976–88.
81. Cross LM, Carrow JK, Ding X, Singh KA, Gaharwar AK. Sustained and prolonged delivery of protein therapeutics from two-dimensional nanosilicates. ACS Appl Mater Interfaces. ACS Publications; 2019;11:6741–50.
82. Du H, Zhang J. Solvent induced shape recovery of shape memory polymer based on chemically cross-linked poly (vinyl alcohol). Soft Matter. 2010;6:3370–6.
83. Késmárky G, Kenyeres P, Rábai M, Tóth K. Plasma viscosity: a forgotten variable. Clin Hemorheol Microcirc. 2008;39:243–6.
84. Traitel T, Cohen Y, Kost J. Characterization of glucose-sensitive insulin release systems in simulated in vivo conditions. Biomaterials. 2000;21:1679–87.
85. Kabiri K, Omidian H, Hashemi SA, Zohuriaan-Mehr MJ. Synthesis of fast-swelling superabsorbent hydrogels: effect of crosslinker type and concentration on porosity and absorption rate. Eur Polym J. 2003;39:1341–8.
86. Kim DB, Choi H, Joo SM, Kim HK, Shin JH, Hwang MH, Choi J, Kim D-G, Lee KH, Lim CH, Yoo SK, Lee H-M, Sun K. A Comparative Reliability and Performance Study of Different Stent Designs in Terms of Mechanical Properties:

Foreshortening, Recoil, Radial Force, and Flexibility. Artif Organs. John Wiley & Sons, Ltd; 2013;37:368–79.
87. MacDonald DJ, Finlay HM, Canham PB. Directional wall strength in saccular brain aneurysms from polarized light microscopy. Ann Biomed Eng. Springer; 2000;28:533–42.
88. Kashyap D, Kishore Kumar P, Kanagaraj S. 4D printed porous radiopaque shape memory polyurethane for endovascular embolization. Addit Manuf. 2018;24:687–95.
89. Hasan SM, Harmon G, Zhou F, Raymond JE, Gustafson TP, Wilson TS, Maitland DJ. Tungsten-loaded SMP foam nanocomposites with inherent radiopacity and tunable thermo-mechanical properties. Polym Adv Technol. 2016;27:195–203.
90. Nash L, Browning Monroe M, Ding Y-H, Ezell K, Boyle A, Kadirvel R, Kallmes D, Maitland D. Increased X-ray Visualization of Shape Memory Polymer Foams by Chemical Incorporation of Iodine Motifs. Polymers. 2017;9:381.
91. Balla VK, Bose S, Davies NM, Bandyopadhyay A. Tantalum—A bioactive metal for implants. Jom. 2010;62:61–4.
92. Cristea D, Ghiuta I, Munteanu D. Tantalum based materials for implants and prostheses applications. Bull Transilv Univ Brasov Eng Sci Ser I. 2015;8:151.
93. Balla VK, Banerjee S, Bose S, Bandyopadhyay A. Direct laser processing of a tantalum coating on titanium for bone replacement structures. Acta Biomater. Elsevier; 2010;6:2329–34.
94. Ionita CN, Loughran B, Jain A, Vasan SS, Bednarek DR, Levy E, Siddiqui AH, Snyder KV, Hopkins L, Rudin S. New head equivalent phantom for task and image performance evaluation representative for neurovascular procedures occurring in the Circle of Willis. International Society for Optics and Photonics; 2012.
95. Yakacki CM, Shandas R, Lanning C, Rech B, Eckstein A, Gall K. Unconstrained recovery characterization of shape-memory polymer networks for cardiovascular applications. Biomaterials. Elsevier; 2007;28:2255–63.
96. Lee EH, Rao GR, Mansur LK. LET effect on cross-linking and scission mechanisms of PMMA during irradiation. Radiat Phys Chem. 1999;55:293–305.
97. Haris M, Kathiresan S, Mohan S. FT-IR and FT-Raman spectra and normal coordinate analysis of poly methyl methacrylate. Pharma Chem. Citeseer; 2010;2:316–23.
98. Nallasamy P, Anbarasan P, Mohan S. Vibrational spectra and assignments of cis- and trans-1, 4-polybutadiene. Turk J Chem. The Scientific and Technological Research Council of Turkey; 2002;26:105–12.
99. Ramachandran P, Naskar K, Nando GB. Effect of electron beam irradiation on the structure–property relationship of ethylene octene copolymer and polydimethyl siloxane rubber blends. Rubber Chem Technol. The Rubber Division, American Chemical Society; 2016;89:477–98.
100. Kuiry S, Seal S, Fei W, Ramsdell J, Desai V, Li Y, Babu S, Wood B. Effect of pH and H 2 O 2 on Ta Chemical Mechanical Planarization: Electrochemistry and X-Ray Photoelectron Spectroscopy Studies. J Electrochem Soc. IOP Publishing; 2002;150:C36.

101. Muschalek R, Nash L, Jones R, Hasan SM, Keller BK, Monroe MBB, Maitland DJ. Effects of sterilization on shape memory polyurethane embolic foam devices. J Med Devices. 2017;11:031011.
102. Oláh L, Filipczak K, Czvikovszky T, Czigány T, Borbás L. Changes of porous poly (ε-caprolactone) bone grafts resulted from e-beam sterilization process. Radiat Phys Chem. Elsevier; 2007;76:1430–4.
103. Coulston F, Korte F. Heavy metal toxicity, safety and hormology. Environ Qual Saf Suppl. 1975;1:1–120.
104. Berenstein A, Song J, Niimi Y, Namba K, Heran N, Brisman J, Nahoum M, Madrid M, Langer D, Kupersmith M. Treatment of cerebral aneurysms with hydrogel-coated platinum coils (HydroCoil): early single-center experience. Am J Neuroradiol. 2006;27:1834–40.
105. Dawson RC, Krisht AF, Barrow DL, Joseph GJ, Shengelaia GG, Bonner G. Treatment of experimental aneurysms using collagen-coated microcoils. Neurosurgery. 1995;36:133–40.
106. Taschner CA, Chapot R, Costalat V, Machi P, Courthéoux P, Barreau X, Berge J, Pierot L, Kadziolka K, Jean B. Second-generation hydrogel coils for the endovascular treatment of intracranial aneurysms: a randomized controlled trial. Stroke. Am Heart Assoc; 2018;49:667–74.
107. Abrahams JM, Forman MS, Grady MS, Diamond SL. Delivery of human vascular endothelial growth factor with platinum coils enhances wall thickening and coil impregnation in a rat aneurysm model. Am J Neuroradiol. 2001;22:1410–7.
108. De Gast AN, Altes TA, Marx WF, Do HM, Helm GA, Kallmes DF. Transforming growth factor β-coated platinum coils for endovascular treatment of aneurysms: an animal study. Neurosurgery. 2001;49:690–6.
109. Medero R, Ruedinger K, Rutkowski D, Johnson K, Roldán-Alzate A. In Vitro Assessment of Flow Variability in an Intracranial Aneurysm Model Using 4D Flow MRI and Tomographic PIV. Ann Biomed Eng. Springer; 2020;1–10.
110. Ohta M, Handa A, Iwata H, Rüfenacht DA, Tsutsumi S. Poly-vinyl alcohol hydrogel vascular models for in vitro aneurysm simulations: the key to low friction surfaces. Technol Health Care. 2004;12:225–33.
111. Bouzeghrane F, Naggara O, Kallmes DF, Berenstein A, Raymond J. In vivo experimental intracranial aneurysm models: a systematic review. Am J Neuroradiol. 2010;31:418–23.
112. Cloft HJ, Altes TA, Marx WF, Raible RJ, Hudson SB, Helm GA, Mandell JW, Jensen ME, Dion JE, Kallmes DF. Endovascular creation of an in vivo bifurcation aneurysm model in rabbits. Radiology. 1999;213:223–38.
113. Kolesky DB, Homan KA, Skylar-Scott MA, Lewis JA. Three-dimensional bioprinting of thick vascularized tissues. Proc Natl Acad Sci. 2016;113:3179.
114. Randles AP, Kale V, Hammond J, Gropp W, Kaxiras E. Performance analysis of the lattice Boltzmann model beyond Navier-Stokes. IEEE; 2013.
115. Bhatnagar PL, Gross EP, Krook M. A model for collision processes in gases. I. Small amplitude processes in charged and neutral one-component systems. Phys Rev. 1954;94:511.

116. Qian Y-H, d'Humières D, Lallemand P. Lattice BGK models for Navier-Stokes equation. EPL Europhys Lett. 1992;17:479.
117. He X, Zou Q, Luo L-S, Dembo M. Analytic solutions of simple flows and analysis of nonslip boundary conditions for the lattice Boltzmann BGK model. J Stat Phys. 1997;87:115–36.
118. Feiger B, Vardhan M, Gounley J, Mortensen M, Nair P, Chaudhury R, Frakes D, Randles A. Suitability of lattice Boltzmann inlet and outlet boundary conditions for simulating flow in image-derived vasculature. Int J Numer Methods Biomed Eng. 2019;35:e3198.
119. Horn JD, Maitland DJ, Hartman J, Ortega JM. A computational thrombus formation model: application to an idealized two-dimensional aneurysm treated with bare metal coils. Biomech Model Mechanobiol. 2018;17:1821–38.
120. Horn JD, Maitland DJ, Hartman J, Ortega JM. Computational study of clot formation in aneurysms treated with shape memory polymer foam. Med Eng Phys [Internet]. 2019; Available from: http://www.sciencedirect.com/science/article/pii/S1350453319302115
121. Lu G, Huang L, Zhang X, Wang S, Hong Y, Hu Z, Geng D. Influence of hemodynamic factors on rupture of intracranial aneurysms: patient-specific 3D mirror aneurysms model computational fluid dynamics simulation. Am J Neuroradiol. 2011;32:1255–61.
122. Cebral JR, Mut F, Weir J, Putman C. Quantitative characterization of the hemodynamic environment in ruptured and unruptured brain aneurysms. Am J Neuroradiol. 2011;32:145–51.
123. Pereira VM, Bonnefous O, Ouared R, Brina O, Stawiaski J, Aerts H, Ruijters D, Narata AP, Bijlenga P, Schaller K. A DSA-based method using contrast-motion estimation for the assessment of the intra-aneurysmal flow changes induced by flow-diverter stents. Am J Neuroradiol. 2013;34:808–15.
124. Mut F, Raschi M, Scrivano E, Bleise C, Chudyk J, Ceratto R, Lylyk P, Cebral JR. Association between hemodynamic conditions and occlusion times after flow diversion in cerebral aneurysms. J Neurointerventional Surg. 2015;7:286–90.
125. Bouillot P, Brina O, Ouared R, Lovblad KO, Pereira VM, Farhat M. Multi-time-lag PIV analysis of steady and pulsatile flows in a sidewall aneurysm. Exp Fluids. 2014;55:1746.
126. Groden C, Laudan J, Gatchell S, Zeumer H. Three-Dimensional Pulsatile Flow Simulation before and after Endovascular Coil Embolization of a Terminal Cerebral Aneurysm. J Cereb Blood Flow Metab. 2001;21:1464–71.
127. Perktold K, Peter R, Resch M. Pulsatile non-Newtonian blood flow simulation through a bifurcation with an aneurysm. Biorheology. 1989;26:1011–30.
128. Szikora I, Paal G, Ugron A, Nasztanovics F, Marosfoi M, Berentei Z, Kulcsar Z, Lee W, Bojtar I, Nyary I. Impact of aneurysmal geometry on intraaneurysmal flow: a computerized flow simulation study. Neuroradiology. 2008;50:411–21.
129. Perktold K, Kenner T, Hilbert D, Spork B, Florian H. Numerical blood flow analysis: Arterial bifurcation with a saccular aneurysm. Basic Res Cardiol. 1988;83:24–31.

130. Steinman DA, Milner JS, Norley CJ, Lownie SP, Holdsworth DW. Image-Based Computational Simulation of Flow Dynamics in a Giant Intracranial Aneurysm. Am J Neuroradiol. 2003;24:559.
131. Reidy M, Schwartz S. Endothelial regeneration. III. Time course of intimal changes after small defined injury to rat aortic endothelium. Lab Investig J Tech Methods Pathol. 1981;44:301–8.
132. Raymond J, Sauvageau E, Salazkin I, Ribourtout E, Gevry G, Desfaits A-C. Role of the endothelial lining in persistence of residual lesions and growth of recurrences after endovascular treatment of experimental aneurysms. Stroke. 2002;33:850–5.
133. Dauchy S, Miller F, Couraud P-O, Weaver RJ, Weksler B, Romero I-A, Scherrmann J-M, De Waziers I, Declèves X. Expression and transcriptional regulation of ABC transporters and cytochromes P450 in hCMEC/D3 human cerebral microvascular endothelial cells. Biochem Pharmacol. 2009;77:897–909.
134. Afonso PV, Ozden S, Prevost M-C, Schmitt C, Seilhean D, Weksler B, Couraud P-O, Gessain A, Romero IA, Ceccaldi P-E. Human blood-brain barrier disruption by retroviral-infected lymphocytes: role of myosin light chain kinase in endothelial tight-junction disorganization. J Immunol. 2007;179:2576–83.
135. Adriani G, Ma D, Pavesi A, Kamm RD, Goh EL. A 3D neurovascular microfluidic model consisting of neurons, astrocytes and cerebral endothelial cells as a blood–brain barrier. Lab Chip. 2017;17:448–59.
136. Abrahams JM, Diamond SL, Hurst RW, Zager EL, Grady MS. Topic review: surface modifications enhancing biological activity of guglielmi detachable coils in treating intracranial aneurysms. Surg Neurol. 2000;54:34–41.
137. Darsaut T, Bouzeghrane F, Salazkin I, Lerouge S, Soulez G, Gevry G, Raymond J. The effects of stenting and endothelial denudation on aneurysm and branch occlusion in experimental aneurysm models. J Vasc Surg. 2007;45:1228–35.
138. Kerber CW, Hecht ST, Knox K. Arteriovenous malformation model for training and research. Am J Neuroradiol. 1997;18:1229–32.
139. Metz H, McElhaney J, Ommaya AK. A comparison of the elasticity of live, dead, and fixed brain tissue. J Biomech. 1970;3:453–8.
140. Elkin BS, Azeloglu EU, Costa KD, Morrison Iii B. Mechanical heterogeneity of the rat hippocampus measured by atomic force microscope indentation. J Neurotrauma. 2007;24:812–22.
141. Zhang L, Bae J, Hardy WN, Monson KL, Manley GT, Goldsmith W, Yang KH, King AI. Computational study of the contribution of the vasculature on the dynamic response of the brain. SAE Technical Paper; 2002.
142. Omori K, Zhang L, Yang KH, King AI. Effect of cerebral vasculatures on the mechanical response of brain tissue: a preliminary study. ASME Appl Mech Div-Publ-AMD. 2000;246:167–74.
143. Hynes WF, Pepona M, Robertson C, Alvarado J, Dubbin K, Triplett M, Adorno JJ, Randles A, Moya ML. Examining metastatic behavior within 3D bioprinted vasculature for the validation of a 3D computational flow model. Sci Adv. 2020;(In Press).

144. Baráth K, Cassot F, Rüfenacht DA, Fasel JH. Anatomically shaped internal carotid artery aneurysm in vitro model for flow analysis to evaluate stent effect. Am J Neuroradiol. 2004;25:1750–9.
145. Gobin Y, Counord J, Flaud P, Duffaux J. In vitro study of haemodynamics in a giant saccular aneurysm model: influence of flow dynamics in the parent vessel and effects of coil embolisation. Neuroradiology. 1994;36:530–6.
146. Boyle AJ, Landsman TL, Wierzbicki MA, Nash LD, Hwang W, Miller MW, Tuzun E, Hasan SM, Maitland DJ. In vitro and in vivo evaluation of a shape memory polymer foam-over-wire embolization device delivered in saccular aneurysm models. J Biomed Mater Res B Appl Biomater. 2016;104:1407–15.
147. Shen TW, Puccini B, Temnyk K, Herting S, Cardinal KO. Tissue-engineered aneurysm models for in vitro assessment of neurovascular devices. Neuroradiology. 2019;61:723–32.
148. Ellegala DB, Day AL. Ruptured cerebral aneurysms. N Engl J Med. 2005;352:121–4.
149. Tzima E, Del Pozo MA, Kiosses WB, Mohamed SA, Li S, Chien S, Schwartz MA. Activation of Rac1 by shear stress in endothelial cells mediates both cytoskeletal reorganization and effects on gene expression. EMBO J. 2002;21:6791–800.
150. Paszkowiak JJ, Dardik A. Arterial wall shear stress: observations from the bench to the bedside. Vasc Endovascular Surg. 2003;37:47–57.
151. Cantu C, Yasaka M, Tsuchiya T, Yamaguchi T. Evaluation of the basilar artery flow velocity by transcranial Doppler ultrasonography. Cerebrovasc Dis. Karger Publishers; 1992;2:372–7.
152. Valdueza JM, Schmierer K, Mehraein S, Einhaüpl KM. Assessment of normal flow velocity in basal cerebral veins: a transcranial Doppler ultrasound study. Stroke. Am Heart Assoc; 1996;27:1221–5.
153. Uchiyama N, Kida S, Nomura M, Hasegawa M, Yamashima T, Yamashita J, Matsui O. Significance of volume embolization ratio as a predictor of recanalization on endovascular treatment of cerebral aneurysms with Guglielmi detachable coils. Interv Neuroradiol. 2000;6:59–63.
154. Tamatani S, Ito Y, Abe H, Koike T, Takeuchi S, Tanaka R. Evaluation of the stability of aneurysms after embolization using detachable coils: correlation between stability of aneurysms and embolized volume of aneurysms. Am J Neuroradiol. 2002;23:762–7.
155. White PM, Lewis SC, Gholkar A, Sellar RJ, Nahser H, Cognard C, Forrester L, Wardlaw JM. Hydrogel-coated coils versus bare platinum coils for the endovascular treatment of intracranial aneurysms (HELPS): a randomised controlled trial. The Lancet. 2011;377:1655–62.
156. McDougall CG, Johnston SC, Gholkar A, Barnwell S, Suarez JV, Romero JM, Chaloupka J, Bonafe A, Wakhloo AK, Tampieri D. Bioactive versus bare platinum coils in the treatment of intracranial aneurysms: the MAPS (Matrix and Platinum Science) trial. Am J Neuroradiol. 2014;35:935–42.

157. Marotta TR, Riina HA, McDougall I, Ricci DR, Killer-Oberpfalzer M. Physiological remodeling of bifurcation aneurysms: preclinical results of the eCLIPs device. J Neurosurg. 2017;128:475–81.